Project 3.05: Prevention of Stress-Induced Failures of Prestressed Concrete Crossties of Railroad Track Structure
Final Report
November 2025

Principal Investigator: Moochul Shin

Civil and Environmental Engineering
Western New England University

Authors
Moochul Shin, ChangHoon Lee, Abdoulaye Diallo, and Cy Riding

Sponsored By
Transportation Infrastructure Durability Center

A report from
Western New England University
Department of Civil and Environmental Eng.
1215 Wilbraham Rd.
Springfield, MA 01119
Phone:413-781-3111
Website: https://wne.edu/

About the Transportation Infrastructure Durability Center

The Transportation Infrastructure Durability Center (TIDC) is the 2018 US DOT Region 1 (New England) University Transportation Center (UTC) located at the University of Maine Advanced Structures and Composites Center. TIDC's research focuses on efforts to improve the durability and extend the life of transportation infrastructure in New England and beyond through an integrated collaboration of universities, state DOTs, and industry. The TIDC is comprised of six New England universities, the University of Maine (lead), the University of Connecticut, the University of Massachusetts Lowell, the University of Rhode Island, the University of Vermont, and Western New England University.

U.S. Department of Transportation (US DOT) Disclaimer

Acknowledgements

Funding for this research is provided by the Transportation Infrastructure Durability Center at the University of Maine under grant 69A3551847101 from the U.S. Department of Transportation's University Transportation Centers Program. The authors also gratefully acknowledge the financial support and cost share contribution provided by Western New England University. Additionally, the authors acknowledge the Texas Advanced Computing Center (TACC) at The University of Texas at Austin for providing computational resources that have contributed to the research results reported within this report. This work used the Extreme Science and Engineering Discovery Environment (XSEDE), Stampede 2 through Project #MSS180002 allocation. The authors acknowledge the expertise provided by Dr. Kwack, who developed the "FlyingFish" in-house finite element software package based on a parallel computing algorithm when he was working as a research programmer at the National Center for Supercomputing Applications (NCSA).

Technical Report Documentation Page

1. Report No.	2. Government Accession No.	3. Recipient Catalog No.
4 Title and Subtitle **Prevention of Stress-Induced Failures of Prestressed Concrete Crossties of Railroad Track**		5 Report Date 6 Performing Organization Code
7. Author(s) Moochul Shin https://orcid.org/000-0001-9153-6000 Chang Hoon Lee https://orcid.org/0000-0001-7209-5203 Abdoulaye Diallo Cy Riding		8 Performing Organization Report No.
9 Performing Organization Name and Address Western New England University 1215 Wilbraham Rd., Springfield, MA 01119		10 Work Unit No. (TRAIS) 11 Contract or Grant No.
12 Sponsoring Agency Name and Address		13 Type of Report and Period Covered 14 Sponsoring Agency Code

15 Supplementary Notes

16 Abstract

Prestressed concrete crossties are vital for railroad stability and safety, but frequently suffer premature failures—such as splitting cracks and corrosion—due to increasing heavy freight and high-speed rail demands. To address these vulnerabilities, this project employs a dual approach of 3D numerical simulation and experimental material development. The research identifies specific failure mechanisms while simultaneously optimizing a new fiber-reinforced "Engineered Cementitious Material" (ECM) designed to bridge cracks and enhance strength. By delivering a material formula with superior resistance to impact and environmental degradation, this study aims to significantly improve the structural integrity of crossties, ensuring safer, more durable railroad infrastructure with an extended service life.

17 Key Words	18 Distribution Statement
Prestressed Concrete Crosstie, Prestressing wire, Indentation, High Performance Concrete, Parallel computing, Fiber, Engineered Cementitious Material	No restrictions. This document is available to the public through

19 Security Classification (of this report)	20 Security Classification (of this page)	21 No. of pages	22 Price
Unclassified	Unclassified	97	$811,758

Form DOT F 1700.7 (8-72)

Contents

List of Figures 5
List of Tables 7
List of Key Terms 7
Abstract 8
Chapter 1 : Introduction and Background 1
1.1 Project Motivation 1
1.1.1 Prestressed Concrete 2
1.1.2 Development of Engineered Cementitious Materials for Railroad Crossties 3
1.2 Research, Objectives, and Tasks 5
1.3 Report Overview 5
Chapter 2 : Literature Review 6
2.1 Yu, et al. 2011 [13] 6
2.2 Oh, et al. 2006 [14] 6
2.3 Malvar 1992 [15] 7
2.4 Gupta and Khapre 2008 [16] 8
2.5 Stuart, Peterman, and Beck 2019 [17] 9
2.6 Background on ECM for Railroad Crossties 10
Chapter 3 : Modeling Setup 13
3.1 Mesh 19
3.1.1 Separating the Pieces: Zoning 19
3.1.3 Element Shape 24
3.2 Material Properties 25
3.2.1 Properties of Steel 25
3.2.2 Properties of Concrete 25
3.3 Constraints 27
3.3.1 Boundary Conditions 27
3.3.2 Prestress and External Load 28
Chapter 4 : Parallel Computing 31
4.1 Transforming the Model 31
4.2 Numerical Analysis Using a Parallel Computing Algorithm 32
4.2.1 Mesh File Conversion 32
4.2.2 Partitioning 32
4.2.3 Analysis 33

4.3 Postprocessing and Visualization: ParaView 35
Chapter 5 : Numerical Analysis 37
5.1 Pull-out Aanalysis 37
5.2 Prestress Analysis: De-tensioning 40
5.2.1 2”x2”x34.5” Prism (Intermediate model) 40
5.2.2 Prestressed Concrete Crosstie - PSCC (Full Scale Model) 50
Chapter 6 : Development Performance-Base Engineered Cementitious Materials for Railroad Crossties 63
6.1 Determination of the Reference Mixture Design based on State Qualified Construction Materials List 63
Chapter 7 : Experimental Program for Developing ECM for Railroad Crossties 67
7.1 Mixture Compositions 67
7.2 Preparation of Specimens 71
7.3 Compressive Strength Measurement 72
7.4 Impact Load Test 72
Chapter 8 : Experimental Results and Discussions for Development of ECM for Railroad Crossties 75
8.1 Compressive Strength with Various Mixture Parameters 75
8.1.1 Effect of Water-to-Binder (W/B) Ratio on Strength 75
8.1.2 Effect of Inclusion of Basalt Fibers 76
8.1.3 Effect of Fly Ash on Compressive Strength 78
8.1.4 Effect of Ground Granulated Blast Furnace Slag (GGBFS) on Compressive Strength 79
8.1.5 Effect of Paste Content 80
8.1.6 Heat Treatment Effect on Compressive Strength at 1 day 81
8.2 Impact Resistance of Developing Concrete 81
8.3 Surface Reflectance of Developing Concrete 84
Chapter 9 Determination of Concrete Mixtures for Railroad Crossties 87
9.1 Water-to-Binder Ratio 87
9.2 Binder and Paste Contents 87
9.3 Supplementary Cementitious Materials 88
9.4 Aggregates 88
9.5 Fiber Inclusion 89
Chapter 10 : Conclusions 90
Chapter 11 References 92

List of Figures

Figure 1.1 Overview of the study on prestressed concrete crossties 0
Figure 1.2 Prestressed concrete mechanism. 2
Figure 2.1 Bond Stress Transfer by wedging (Malvar, 1992) [15] 7
Figure 3.1 Wire Model Dimension [41]. 12
Figure 3.2Tendon Indentation Examples [42]. 13
Figure 3.3 Circular Pattern 3D Numerical Model 15
Figure 3.4 Chevron (a) and Chevron, Single Reversed (b) 3D CAD Models 16
Figure 3.5 Chevron WG 3D CAD Model 16
Figure 3.6 CSquare (a) and OSquare (b) 3D CAD Model Comparison 17
Figure 3.7 Csquare Rotated 30° 3D CAD Model 17
Figure 3.8 3D CAD wire models: (a) Smooth WA, (b) shallow-Chevron WG, and (c) deeper chevron WP. 18
Figure 3.9 Partition Zone Labels (Small scale model) 20
Figure 3.10 (a) Zones on Prestressed Concrete (PSC) WG Model and (b) Zones on Prestressed Concrete (PSC) WA&WP Models 20
Figure 3.11 Local Seeds of Chevron Reinforcement at the Interface Zone 21
Figure 3.12 Concrete Stress-Strain Responses to Uniaxial Tension and Uniaxial Compression [44]. 26
Figure 3.13 Boundary condition of Reinforced Block (a) Small (b) Intermediate (c) Full size 27
Figure 3.14 Prestressed Member in Reinforced Concrete (a) Small (b) Intermediate (c) Full size 28
Figure 3.15 Displacement Control Loading (Pullout) 29
Figure 4.1 Parallel Computing Steps 30
Figure 4.2 Speed up test (# Cores vs Time) 33
Figure 4.3 Circular Reinforcement Pattern after A PSC Prism with WA (a smoother tendon) 35
Figure 4.4 Elements less than or equal to 500 psi: PSC-WG 35
Figure 5.1 Pull-Out Test Schematic. 36
Figure 5.2 Force Displacement Results, All Models. 38
Figure 5.3 Model Partition. 40
Figure 5.4 PSC Prism – WG mesh refinement. 40
Figure 5.5 Sensitivity analysis: Mesh Size on PSC Prism-WA 41
Figure 5.6 Line Analysis around free end. 41
Figure 5.7 Max and Min Principal stress: PSC Prism-WA 42
Figure 5.8 Indentation Profile 42
Figure 5.9 Max and Min Principal stress, PSC Prism-WG 43
Figure 5.10 Max and Min Principal stress, Chevron_WP_Prism_M3. 44
Figure 5.11 Comparisons of three prisms. 45
Figure 5.12 Damaged portion of the PSC Prism-WA model due to tensile and compressive stresses. 46
Figure 5.13 Damaged Radius of the PSC Prism-WA (Maximum Principal Stress and Minimum Principal Stress). 46

Figure 5.14 Damaged portion of the PSC Prism-WG model due to tensile and compressive stresses. 47
Figure 5.15 Damaged Radius of the PSC Prism-WG (Maximum Principal Stress and Minimum Principal Stress). 47
Figure 5.16 Damaged portion of the Smooth_WP_Prism model due to tensile and compressive stresses. 48
Figure 5.17 Damaged Radius of the PSC Prism-WG (Maximum Principal Stress and Minimum Principal Stress). 48
Figure 5.18 Damaged volume study. 49
Figure 5.19 (a) Full crosstie model, (b) Divided Full model (with PSCC highlighted), (c) Quarter PSCC model 50
Figure 5.20 (a) Material property assigned, (b) boundary conditions applied and prestress applied to the tendons 50
Figure 5.21 Meshing. 51
Figure 5.22 Effect due to rotating the tendons. 52
Figure 5.23 1st and 2nd Tendon Arrangement. 53
Figure 5.24 Displacement Comparisons. 53
Figure 5.25 Overlapped PSCC models. 54
Figure 5.26 Interlocking effect Explained, Overlapped tendons. 54
Figure 5.27 Normalized Displacement Comparisons of PSCC models. 55
Figure 5.28 Line Stress Analysis. 55
Figure 5.29 Line Stress Analysis on Indentations # 1-8 from PSCC models. 57
Figure 5.30 Stress curves (MaxPs &MinPs) from the indentation #4 57
Figure 5.31 Volume of damaged material with respect to stress interval 58
Figure 5.32 PSCC-WA: Tensile strength of 500 psi 59
Figure 5.33 PSCC-WA: Tensile strength of 1000 psi 59
Figure 5.34 PSCC-WG: Tensile strength of 500 psi 60
Figure 5.35 PSCC-WG: Tensile strength of 1000 psi 60
Figure 5.36 PSCC-WP: Tensile strength of 500 psi 61
Figure 5.37 PSCC-WP: Tensile strength of 1000 psi 61
Figure 6.1 Relationship amongst Design Strength, Total Cementitious Material Content, and Slump in QCML Database 62
Figure 6.2 Relations of Design Strength, Air Content, and Nominal Maximum Aggregate Size 63
Figure 6.3 Estimated W/B ratio and Paste volume fraction (relative to 1 cubic yard of the concrete) with respect to strength 63
Figure 6.4 Relation between W/B and Paste volume fraction 64
Figure 7.1 Passing Percent of Fine, Coarse, and Mixed Aggregates 66
Figure 7.2 Apparatus of Impact Loading Test 71
Figure 7.3 LabSphere Portable Reflectometer Kit 72
Figure 7.4 Preparation of Specimens for Measuring Reflectance of Concrete Surface 73
Figure 8.1 Strength with varying W/B ratio 74
Figure 8.2 Strength development of concrete with different dosage of Basalt fibers: (a) Inclusion of 44-mm fibers and (b) Inclusion of 22-mm fibers 75
Figure 8.3 Comparison of Strength with different dosage of Basalt fibers: (a) Inclusion of 44-mm fibers and (b) Inclusion of 22-mm fibers 76

Figure 8.4 Strength development of Air-Entrained Concrete with Different Dosage of 22-mm Basalt fibers 76
Figure 8.5 Strength development with Different Replacement Ratios of Fly Ash 77
Figure 8.6 Strength development with Different Replacement Ratios of GGBFS 78
Figure 8.7 Comparison of Compressive Strength with Different Paste Content (a) by Mass and (b) by Volume Ratio (V_p) 79
Figure 8.8 Heat Treatment Effect at 1 day 80
Figure 8.9 Comparison of Impact Test for the Concretes with (a) 44-mm and (b) 22-mm Basalt Fibers 81
Figure 8.10 Comparison of Impact Test for the Concretes with M17, M18, and M19 82
Figure 8.11 Samples of the Concrete Failure after Impact Loading up to 4 Times 82
Figure 8.12 Specimens after exposure to different environmental conditions: (a) Front Face and (b) Side Face 83
Figure 8.13 Reflectance Values for Specimens exposed to different environmental conditions: (a) Front Face and (b) Side Face 84
Figure 8.14 Relationship between Strength and Surface Reflectance 84
Figure 9.1 Comparison of Strength Development for the Mixtures with Lower W/B Ratios 86
Figure 9.2 Relationship between Strength and S_A 87

List of Tables

Table 2.1 Performance of FEA code on PARAM 10000 [16] 8
Table 3.1 Wire model dimensions and geometrical properties. 13
Table 3.2 Wire geometrical properties. 14
Table 3.3 Wire model dimension and Geometrical properties. 15
Table 3.4 Wire geometrical properties. 15
Table 3.5 Set Radius and Thickness 22
Table 3.6 Approximate Element Sizes by Zone (Pullout) 22
Table 3.7 Approximate Element Sizes by Zone (Prestress) 22
Table 3.8 Number of Nodes and Elements in Each Small Model 23
Table 3.9 Number of Nodes and Elements in Each Larger Model 23
Table 3.10 Elastic Properties of Steel 24
Table 3.11 Plasticity Parameters for Concrete Damaged Plasticity Model. 25
Table 4.1 Queue, Node, and core Information [46]. 32
Table 4.2 Number of Cores Versus Time. 33
Table 5.1 Models Sorted by Stiffness. 37
Table 5.2 Element and Nodes. 39
Table 6.1 Limits on Cementitious Materials by ACI 318 [50] (for exposure class F3) and ACI 350R-20 [51] 64
Table 6.2 Range of Mixture Parameters 65
Table 7.1 Mixture proportion of Group 1 (per a cubic yard of concrete) 67
Table 7.2 Mixture proportion of Group 2 (per a cubic yard of concrete) 68
Table 7.3 Mixture proportion of Group 3 (per a cubic yard of concrete) 69
Table 7.4 Mixture proportion of Group 4 (per a cubic yard of concrete) 70

List of Key Terms

PSCCs: Prestressed Concrete Crossties
ECM: Engineered Cementitious Materials

Abstract

Prestressed concrete crossties (PSCCs) serve as an essential component of modern railroad track structures, intended to withstand heavy freight loads and ensure passenger safety for a service life of up to 50 years. However, as the industry moves toward heavier axle loads and higher-speed train systems, these components are increasingly suffering from premature failures, including splitting cracks, rail seat deterioration, and center binding. A significant structural challenge is that, unlike highway girders, many PSCCs lack transverse reinforcement (stirrups), making them highly vulnerable to impact and environmental degradation once the bond between the concrete and prestressing wires is compromised. To address these critical issues, this project employs a comprehensive research approach that integrates advanced numerical simulation with experimental material design. This study is utilizing 3D finite element modeling to pinpoint the potential mechanisms of splitting cracks that occur during the de-tensioning of prestressing wires using a parallel computing algorithm. Simultaneously, the project focuses on developing a novel fiber-reinforced "Engineered Cementitious Material" (ECM) designed to bridge microcracks and enhance tensile capacity. A key step involves optimizing the fiber content to balance structural strength against potential downsides, such as increased surface roughness—which can lead to abrasion—and the corrosion risks associated with traditional steel fibers. The findings from this project delivers a new, high-performance concrete formulation with superior impact resistance, corrosion durability, and concrete-wire bonding properties. By mitigating the primary causes of premature failure, this research directly contributes to extending the life cycle of railroad infrastructure, reducing maintenance burdens, and ensuring the safety of the national rail network.


1865 THE UNIVERSITY OF MAINE
UMASS LOWELL
WESTERN NEW ENGLAND UNIVERSITY
WNE
UCONN
THE UNIVERSITY OF RHODE ISLAND
The UNIVERSITY of VERMONT

Chapter 1 : Introduction and Background

1.1 Project Motivation

This study focuses on improving the life cycle of the railroad track structure by examining failure mechanisms of prestressed concrete crossties (PSCCs). As the loading demands increase as results of increasing freight axle loads and the interest in developing a higher speed train system, PSCCs have become an important structural component of the railroad track structure. However, in light of those ever-increasing demands, ensuring the safety and longevity of the track structure has been of great concern, since multiple railroad accidents occurred due to premature failures of the track structure including PSCCs prior to their expected service life, i.e. 50 years [1], [2]. Some of the failure modes of PSCCs are as follows, not limited to: splitting/bursting failures, center binding, rail seat deterioration (RSD), and loss of cover concrete. Although the Federal Railroad Administration (FRA) has been sponsoring multiple research activities in order to improve the structural integrity of the PSCCs-based track structure [3], [4], [5], our understanding on the failure mechanisms of PCSSs has been limited due to the complex behaviors of the heterogeneous concrete material, interfacial mechanics between prestressing wires and concrete, and various design parameters (not-standardized) in the industry. Figure 1 shows exemplary pictures of a derailment accident [1], damaged ties [2], and various prestressing wires in use [6], and the overview of the proposed study. The research activities include conducting numerical analyses by developing a 3D finite element model of prestressed concrete prisms and crossties, and performing experimental tests to develop new engineered cementitious materials (ECM) for highly improved bonding mechanisms.

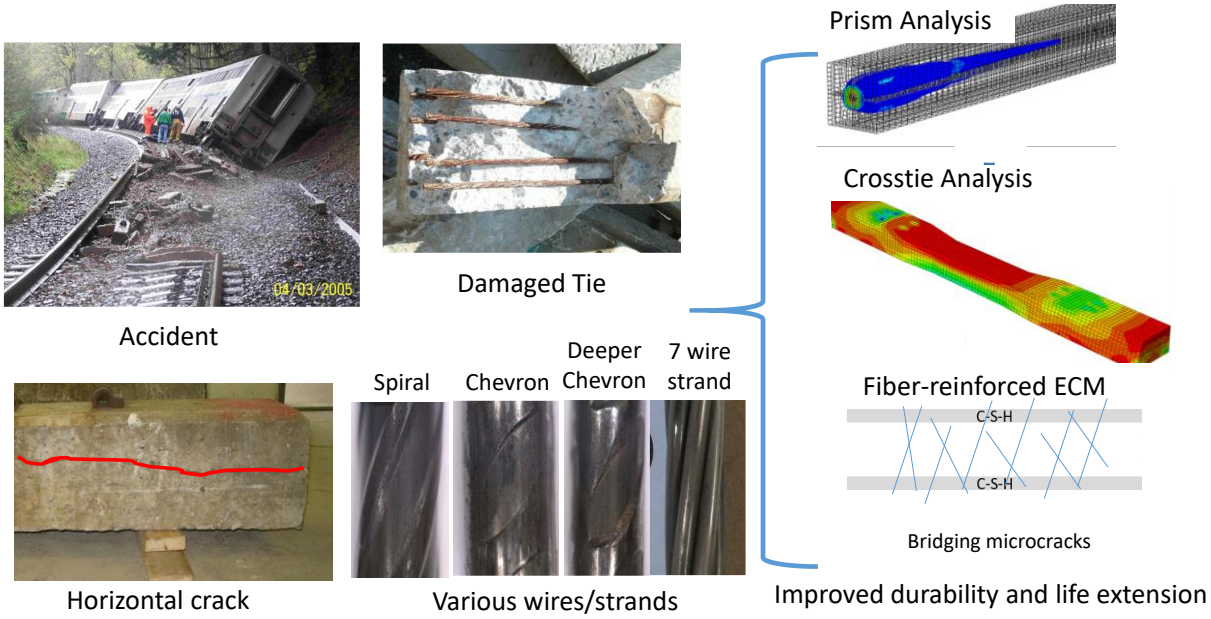

Figure 1.1 Overview of the study on prestressed concrete crossties

Since the 1960s and 70s, concrete crossties have been increasingly adopted in North American, largely due to their potential for lower life-cycle costs compared to traditional wooden ties. Despite this shift, there have been premature failures of PSCCs, and researchers have been working to fully understand their failure mechanisms. To investigate these complex behaviors, this project employs the finite element method (FEM). This numerical approach allows for the prediction of structural performance in scenarios where geometric complexity, especially different types of indentations of prestressing tendons and wires, material properties, and/or combined loading make traditional analysis difficult. This study is utilizing 3D finite element modeling to pinpoint the potential mechanisms of splitting cracks that occur during the de-tensioning of prestressing wires using a parallel computing algorithm. Simultaneously, the project focuses on developing a novel fiber-reinforced "Engineered Cementitious Material" (ECM) designed to bridge microcracks and enhance tensile capacity. A key step involves optimizing the fiber content to balance structural strength against potential downsides, such as increased surface roughness—which can lead to abrasion—and the corrosion risks associated with traditional steel fibers.

1.1.1 Prestressed Concrete

Concrete is a remarkably common yet structurally complex material. It's a heterogeneous mixture composed of fine and coarse aggregate, cement, water, air, and often chemical admixtures. The chemical reaction that occurs when these basic components are mixed creates the durable foundation for modern construction. Reinforced concrete is technically a composite material, combining two or more distinct components to create a final product superior to the original parts.

Concrete possesses high compressive strength (resisting being squeezed) but is exceptionally weak in tension (resisting being pulled apart). To overcome this weakness, concrete is paired with steel tendons (or strands). When the composite material is subjected to tensile forces, the load transfers to the steel, effectively preventing failure.

The technique of prestressing significantly improves this tensile capacity. With standard reinforced concrete, some degree of tensile cracking is almost inevitable, but prestressing can completely eliminate it. Prestressing is achieved by placing the steel tendon under high tension before the concrete hardens (Figure 1.1a). Once the concrete cures, the pretension force is released, causing the tendon to attempt to contract back to its original length (Figure 1.1b). This contraction creates beneficial internal compressive forces within the concrete (Figure 1.1c). These built-in forces counteract the tensile stresses that occur when external loading is applied (such as a train running on the rail, Figure 1.1d), resulting in a far more durable and crack-resistant structural component.

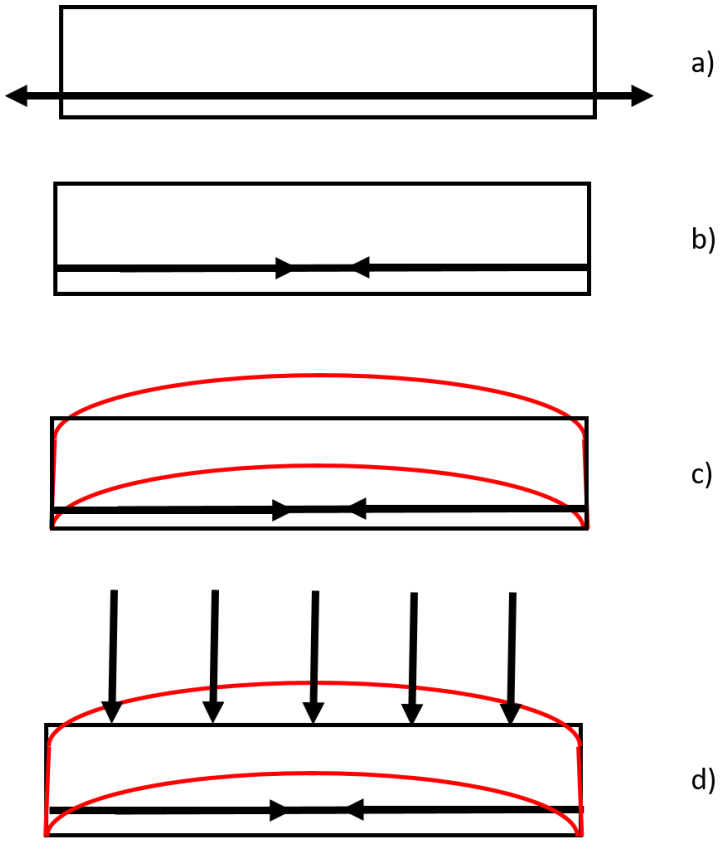

Figure 1.2 Prestressed concrete mechanism.

1.1.2 Development of Engineered Cementitious Materials for Railroad Crossties

The railroad crosstie (often called “sleeper”) is a critical structural component that transfers rail loads to the ballast and underlying track substructure. In the United States, wooden crossties have been the predominant choice since the inception of the rail industry in the early to mid-1800s [7]. In response to concerns about potential timber shortages, the Association of American Railroads (AAR) initiated efforts in 1957 to develop prestressed concrete crossties, leading to several subsequent field evaluations [8]. Wooden crossties, however, exhibit relatively low resistance to mechanical loading and environmental exposure, including moisture and biological degradation [9]. Although chemical treatments have been implemented to improve decay resistance and extend service life, some treatment agents raise environmental and health concerns during manufacturing and handling [9]. In addition, wooden crossties typically have shorter service lives than their concrete counterparts, resulting in increased maintenance demands and higher long-term replacement costs.

The unit price of a concrete crosstie, including fasteners and labor, is approximately twice that of a wooden tie [10]. However, because the required spacing for concrete ties is 24 in., compared to 19.5 in. for wooden ties, the overall cost of constructing a mile of railway with concrete crossties is about 70% higher than that with wooden ties. Consequently, it is reasonable to ask whether the service life of concrete crossties is sufficiently long to justify the higher upfront cost. Interestingly, Ferro et al. [11] reported that the average service life of appropriately treated

timber crossties is approximately 30 years, whereas prestressed concrete crossties can be designed for a service life of up to 60 years. Therefore, this rough cost-benefit comparison supports the use of concrete crossties.

Nonetheless, AREMA [12] does not specify a particular minimum service life. Instead, it requires that the concrete used for the tie achieve a minimum 28-day compressive strength of 7,000 psi and references relevant ASTM standards for evaluating durability performance, specifically freeze-thaw resistance and alkali-silica reaction, to ensure adequate service life. Therefore, the primary objective of this research is to develop concrete mixtures that satisfy the criteria suggested by AREMA. Achieving sufficiently high strength is essential for improved structural integrity and durability, which can be realized through a denser microstructure of the hydrated products. At the same time, the associated cost and environmental impact of such mixtures must be considered. Accordingly, this study investigates the influence of individual cementitious ingredients and provides recommendations for mixture development.

1.2 Research, Objectives, and Tasks

The objectives of this study are to:

- identify the main mechanisms of horizontal cracks upon de-tensioning prestressing wires with respect to various geometrical/mechanical parameters.
- develop more durable bonding mechanisms of PSCCs .
- develop fiber-reinforced engineered-cementitious materials (ECM), which can be adopted for PSCCs.
- develop framework for a numerical analysis of prestressed concrete blocks using a parallel computing algorithm.

The tasks of this study are to:

- develop FE models of prestressed concrete prisms with various indented wires
- develop FE models of prestressed concrete crossties
- conduct crosstie analyses
- find optimal concrete mixtures for fiber-reinforced ECM
- conduct mechanical tests on the fiber-reinforced ECM

1.3 Report Overview

This report is organized into ten chapters. Chapter 1 serves as an introduction, outlining the fundamental background of prestressed concrete, along with the research motivation, objectives, and specific tasks. Chapter 2 provides a comprehensive literature review. The computational methodology is detailed in Chapters 3 and 4; Chapter 3 focuses on the development and preprocessing of numerical models, while Chapter 4 describes the utilization of supercomputing resources to run numerical analysis of de-tensioning of prestressed concrete models using parallel computing algorithms and data visualization techniques. Chapter 5 presents numerical analyses results. Chapters 6 through 9 focus on the experimental development of Engineered Cementitious Materials (ECM); Chapter 6 presents the basic mixture design and explore key parameters for ECM. Chapter 7 describes the experimental tests, while Chapter 8 reports the testing results, Chapter 9 provides optional design guidelines for of fiber-reinforced Engineered Cementitious Materials (ECM). Finally, Chapter 10 summarizes the study's conclusions and offers recommendations.

Chapter 2 : Literature Review

During the major North American rail infrastructure investments of the 1960s, concrete crossties were identified as a preferred alternative to timber, primarily due to their potential for lower life-cycle costs. However, many critical structural characteristics of these components were not fully understood at the time. Subsequent research has sought to address these knowledge gaps. Yu et al. (2011) [13] provide a detailed analysis of the complexities associated with prestressed concrete crossties, while Oh et al. (2006) [14] and Malvar (1992) [15] offer significant insights into the fundamental mechanics governing the interaction between prestressing tendons and the concrete matrix.

2.1 Yu, et al. 2011 [13]

Despite the advantages of concrete ties over timber, only about 5% of the ties in track are concrete in North America. A big reason for this is the concern over unresolved performance issues which cause higher-than-predicted maintenance costs and shorter service lives. To correct these issues, research into the behavior of these reinforced concrete ties under a dynamic load is necessary. This calls for smaller scale models that account for the heterogeneity of the crossties which include explicit modeling of the strand and concrete components and an understanding of the bond-slip relationships. Yu, et al. (2011) seek to create a finite element model (using the ABAQUS FEA software) which includes pretensioning and rail seat loads, however ignores the fastening system and simulates the ballast and subgrade as to study their response.

Yu, et al. use some basic parameters which we have adopted to our model; the Young's modulus for the steel was taken to be 30,000 ksi with a Poisson's ratio of 0.3 and is linear elastic throughout. The concrete is modeled using the Concrete Damaged Plasticity model, for which some factors must be modified to meet our research needs. In particular, the damage factors which are used in calculating post-peak stress-strain response are based off of the fracture energy and will be revisited when creating our own model.

2.2 Oh, et al. 2006 [14]

An important precondition of the paper is understanding the term transfer length, which Oh et al. (2006) describe as the distance from one face of the tendon to the point at which prestress is equal to zero.

Prestressed concrete is becoming more common in the field, but standards have not quite adapted to its more frequent use. Current design standards – note that this paper was published in 2006 – only consider strand diameter and prestress intensity when determining transfer length, neglecting concrete strength and cover thickness. Therefore, it is necessary to establish a more comprehensive method for calculation transfer length.

The idea of the paper is to provide realistic, theoretical predictions for transfer length of pretensioned prestressed concrete. Some key assumptions in this paper are considering prestressing steel as a solid cylinder and surrounding concrete as a hollow cylinder, the compatibility equation, and appropriate equilibrium equation. Cracking is considered by an appropriate tensile stress-crack width relationship. The theoretically predicted values are corroborated with experimental results with good correlation.

Another important understanding is that of the bond mechanism. The bond is the property that causes hardened concrete to grip embedded steel in such a manner as to resist forces tending to

slide longitudinally through the concrete. Bond strength is dependent on two factors: coefficient of friction (determined to be 0.4 as a typical value for concrete/steel) and the radial stress – or interface pressure, as the paper calls it. This interface pressure comes from the tendon shrinking lengthwise and expanding in the radial direction causing pressure at the concrete/steel interface. Using the thick cylinder theory, stresses, strains, and displacements can all be calculated with appropriate compatibility and equilibrium equations.

The equilibrium equations are developed for the solid steel cylinder and hollow concrete cylinder independently and combined. Ultimately, it comes down to the radial stress through the cylinder minus the hoop stress in the circumferential direction must be equal to zero.
The compatibility equation, although in the same idea, is much simpler. It states that the displacement of the steel and the thickness of the steel before prestressing must be equal to the displacement of the concrete plus the thickness of the steel after prestressing.

One of the most important features in pretensioned concrete members is the correct transfer of prestress into the concrete because prestress is released to zero on both ends. Cracking occurs around the interface due to the radial expansion at the release of the prestress. The effects of partial and full cracking are taken into account using the tensile strength-crack width relationship and construction of the governing equation. The equilibrium equations are then solved for each segment member in the longitudinal direction and strain development curves can be generated. These strain development profiles allow the transfer length to be determined. This theory is then verified experimentally.

2.3 Malvar 1992 [15]

Malvar (1992) is concerned with the local bond stress-slip of reinforcing bars inside of concrete. This paper describes a relationship between radial confining stress in the interface zone and bond stress and slip as the main variables in being able to describe the behavior in the interface zone. The objectives outlined in the paper are establishing the necessity for considering radial stress and deformation in studying bond phenomena, show that certain bond characteristics are dependent on (or at least sensitive to) the specimen configuration during testing, and to determine configuration-independent local bond stress-slip relationships for two types of tendon with different deformations. This is performed using 12 specimens of #6 tendon (3/4" nominal diameter) of two different types.

The practical benefit of this paper to our research is that considering actual bond-slip properties allows for a much more realistic prediction of crack formation. Differences in bond assumptions will change the predicted crack pattern which, in turn, affects the distribution of internal forces, the ultimate stress, and the mode of failure.
The mechanism of bond is threefold: mechanical interlock (concrete seeping and hardening between bar ribs after pour), friction, and chemical adhesion. For very small stress values (up to about 200 psi), chemical adhesion will be the main resisting mechanism, however in our research the prestress alone is much higher than this threshold (about 200 ksi). At this point, the main resistance to failure comes from the wedging action of the ribs, as shown in Figure 2.1. The wedging originates crushing in front of the ribs, radial cracking, and eventually longitudinal cracking. If the confining pressure is adequate, bond stress reaches a maximum of about 1/3 f'_c before the concrete fails and friction becomes the resisting mechanism.

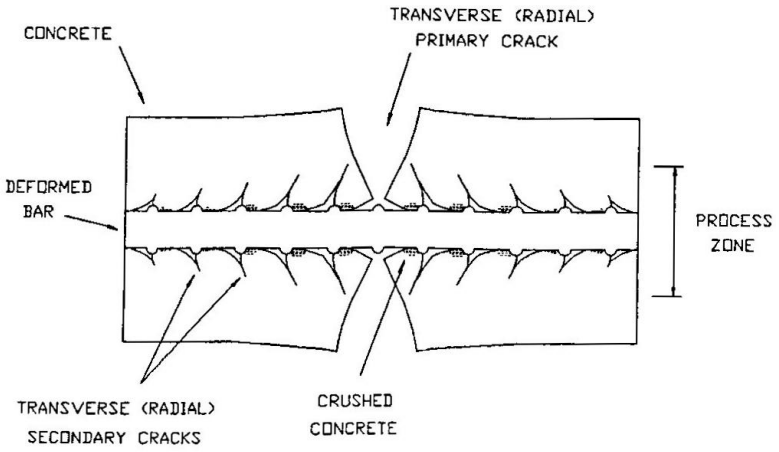

Figure 2.1 Bond Stress Transfer by wedging (Malvar, 1992) [15]

As a result of experimentation, Malvar (1992) makes six observations regarding bond slip variables:

1. If confinement is not provided, bond stresses disappear as the longitudinal cracks develop though the cover.
2. The cover itself provides confinement through tensile hoop stresses prior to cracking.
3. Ultimate resistance at large slips appears to be Coulomb friction type.
4. Bond stress is higher when bars are pushed instead of pulls (Poisson's effect)
5. Variations in test specimens provide varying degrees of confinement and therefore bond stress-slip discrepancies.
6. Effects of concrete cover, bar spacing, position, end distance, and transverse reinforcement could be predicted via the confinement each provides.

Malvar concludes the paper with another six observations, but one of these jumps out far more than the others: bars with ribs at 90° to the longitudinal axis exhibited better bond characteristics than inclined ribs. They also produced more severe radial cracking and generated a wider process zone. This observation is greatly important to us as the models developed for our own research have ribbing generated at multiple inclines. An important consideration to this factor however, is the manufacturing process for the reinforcing wires. The indentation is created by stamping, and as such, perfect 90° sidewall angles are very difficult to create.

2.4 Gupta and Khapre 2008 [16]

Gupta and Khapre (2008) investigate stress development in anchorage zone in prestressed post-tensioned concrete beam using FEA and the PARAM 10000 supercomputer. The PARAM 10000 was released in 1998 and as such, significant computing progress has been made since its release. Much of the focus of this paper is running advanced calculations on parallel processors and so is still very relevant to the current research. Gupta and Khapre seek to analyze the spalling zone and bursting tensile force around the anchoring zone using these techniques.
In the prestressed post-tensioned concrete beam, anchorage zone is the zone in which complex stress develop. Transverse tensile stresses develop along the axis of loading. When these tensile stresses go beyond a certain threshold, the reinforced beam can burst. Transverse tensile stresses

can also develop in the regions around the free corners of the beam, which are generally designated as the spalling zone.

The literature review shows that parallel solvers can significantly reduce the computation time in complex nonlinear dynamic FEA as well as in simple linear elastic FEA. Gupta and Khapre seek to study the effect of Poisson's ratio and eccentricity of prestressing forces on development of stresses in anchorage zone and spalling zone in prestressed post-tensioned concrete beam by first verifying their algorithm with comparisons with existing literature. These variables (the ratio of loaded area and cross-sectional area of the beam, eccentricity, and Poisson's ratio) are then varied to study their effect on stress distribution. A generalized code is developed using FEM on the platform of supercomputer PARAM 10000 with matrix inversion parallel solver to carry out the structural analysis.

In 2008 (and using a 1998 machine) it took Gupta and Khapre 11.05 hours to analyze a member with "4800 three noded triangular elements with 2501 nodes each having two degree of freedom, hence resulting in global stiffness matrix of size 5002×5002" (Gupta & Khapre, 2008) on a single processor. Using the full extent of the machine with their parallelization of five processors, the solution was found in around 2.4 hours. The difference the number of processors makes is highlighted in the Table 2.1 - Performance of FEA code on PARAM 10000 [16].

Table 2.1 Performance of FEA code on PARAM 10000 [16]

No. Of Processors	Computational Time		Speedup	
	Total (Hours)	Communication (Minutes)	Actual	Ideal
1	11.046484	0.0000	1	1
2	5.5350045	1.0528	1.99575	2
3	3.6807758	3.0751	3.00113	3
4	3.607758	2.6418	3.9223	4
5	2.8163307	3.9173	4.59453	5

The major takeaway from this paper is how much more efficient multicore processors at performing the complex solid mechanics and matrix transformations than a standard single core processor using a direct solver. This will be used and improved upon over a decade later through the use of one of the super computer clusters, i.e. the Stampede2 high performance computer.

2.5 Stuart, Peterman, and Beck 2019 [17]

This Federal Railroad Administration report uses non-contact optical wire indentation profiling developed by Kansas State University to measure the geometric parameters of prestressed wire reinforcements as to determine their impact on transfer length and crack propensity in prestressed concrete prisms. Their analysis shows a correlation between parameters explored in this report such as indent shape, side angle, indent depth, sidewall area, and volume as well as parameters like cover depth and release strength. This report concludes that increasing cover depth is the most impactful criteria for reducing crack length and that the volume of the indentation is most important for determining the transfer length. These results were shown to be statistically significant and provide us a useful comparison for exploring our own parameters.

The main conclusion drawn from this paper is the factors of influence:

- Volume of indentation over the depth
- Shape effect
- Side wall angle

Each of these factors are explored, particularly in the elastic model, in this research.

With the background provided by Yu, et al. the framework for the damaged plasticity model can be developed. This is the key model property for accurately portraying the crack analysis in this research. Oh, et al. and Malvar provide context for how the interaction between the tendon and the concrete affects the response of the concrete. The concept of transfer length is thoroughly explained by Oh, et al. and the bonding properties and failure mechanisms around the interference zone, which is the focus locale for this research is explored by Malvar. These two papers are instrumental for the background understanding of what is happening within the model and where and why we will be looking for failures and responses are specific points. The report by Gupta and Khapre, although not directly related to the research, highlights the need for multiple processors when analyzing high volume data. It is the first level of insight into the notion that local computers and single core processors cannot handle the vast quantity of data being processed by such large calculations. Finally, the Federal Railroad Administration report [17] introduces the impact the geometric variables of the tendon has on the response of the concrete in terms of transfer length and crack propensity. Most, if not all, of these variables will be explored in this research and it is a great comparison to have.

2.6 Background on ECM for Railroad Crossties

The improvement of the mechanical property and the durability is the key for elongating the life-cycle of the concrete structures. Currently, as the need to improve the structural and material performances of cement-based materials has grown, many researchers have proposed methods to produce so-called Ultra-High Performance Concrete (UHPC). The definition of UHPC maybe ambiguous because the adjective “ultra” is qualitative, thereby requiring the datum to which any mechanical or other properties can be referenced. Accordingly, ACI 239R-18 [18] defines UHPC as “a concrete that has a minimum specified compressive strength of 22,000 psi (150 MPa) with specified durability, tensile ductility, and toughness requirements,” and similar definition can be found in elsewhere [19]. However, the “specified” requirement is translated by the parameters in design/analysis process, thus it can be deviant from the measured material properties. Nevertheless, there is an agreement that the compressive strength of UHPC must be approximately 3 to 6 times higher than that of the conventional concrete, which generally ranges from 3,000 psi to 6,000 psi (20 to 40 MPa). Also, the higher strength concretes generally implies having denser microstructure, as reported by [20], [21] thereby inevitably leading to improve the durability performance as mitigating the penetration of any chemicals and water in the service period. Furthermore, the higher toughness and tensile ductility may require more than benefits of denser microstructure, thus addition of a variety of fibers can be incorporated to improve the associated performance [22], [23], [24].

Despite the substantial improvements in structural integrity offered by UHPC, its environmental impact and cost are considerably higher than those of conventional concrete. Because UHPC

contains no coarse aggregates, it requires a substantially higher paste content, which further elevates both cost and environmental burden. Farahzadi et al. [25] reported that UHPC mixtures typically contain approximately 1,300 to 1,700 lb of cementitious materials per cubic yard of concrete (roughly 60% by volume), with material costs ranging from $1,900 to $3,700 per cubic yard [26]. Considering that the price of a prestressed concrete tie with fasteners is approximately $220, the use of UHPC for railroad crossties appears limited, despite its demonstrated benefits in structural integrity and durability performance. Further, although the definition of UHPC is advantageous in its broad applicability, the concept of "performance" within this classification remains largely qualitative. Consequently, generalizing UHPC requirements across diverse applications is impractical. For example, the performance demands of a bridge deck differ significantly from those of a railroad tie, even if both materials are categorized as UHPC. To address this limitation, the notion of performance-oriented UHPC has been proposed [9], emphasizing the tailoring of material properties to meet application-specific performance criteria rather than adhering to a fixed set of mixture parameters. In line with the broader movement toward performance-based concrete mixture design, AASHTO PP-84 [27] provides guidance for performance-engineered concrete mixtures for pavement applications, and the National Ready Mixed Concrete Association promotes a "Prescriptive-to-Performance" initiative to support specifying concrete based on intended functional requirements. Furthermore, ACI Committee 329 [28] outlines performance-based requirements for concrete, detailing the responsibilities of owners, contractors, and producers, relevant test methods, and associated acceptance criteria. In addition to performance considerations, the properties of concrete can vary significantly depending on the characteristics of locally available constituent materials, unless proprietary mixture systems are used. Therefore, designing mixtures to achieve targeted performance requires both the development of a comprehensive materials database and adjustments tailored to regional material sources.

In this context, the present research aims to develop cement-based materials using constituents readily available in Western Massachusetts, with a focus on meeting the designated performance requirements for railroad crossties. The performance criteria targeted in this study include: (1) the AREMA compressive strength requirement, (2) resistance to impact loading, and (3) abrasion resistance. Durability performance is anticipated to be achieved through strength enhancement [29], as a denser microstructure of hydrated products not only improves structural integrity but also reduces the ingress of aggressive chemicals.

The AREMA requirement for railroad crossties (i.e., achieving a compressive strength exceeding 7,000 psi at 28 days) falls within the category of high-strength concrete rather than UHPC. Attaining such strength typically necessitates a reduced water-to-binder ratio in combination with a relatively higher paste content to maintain the designated workability. Piasta and Zarzycki [30] reported that, for mixtures with a W/B ratio between 0.25 and 0.35, compressive strength increases as paste content decreases; however, this relationship is nonlinear, indicating the need for comprehensive experimental evaluation. In addition, to reduce the environmental impact associated with increased binder usage, incorporating supplementary cementitious materials becomes essential.

Railway crossties are frequently subjected to impact loading generated by conditions such as flat wheels and dipped rails. Kaewunruen [31] reported that these dynamic impact loads can range

from 200 kN to 600 kN; however, their consideration in current design specifications for crossties remains limited. Extensive research has been conducted to mitigate impact-induced damage at both the structural and material levels. In the context of the research on the manipulation of the material, fiber-reinforced concrete has been widely investigated as a means to enhance impact resistance at the material scale. Mao et al. [32] reported that increasing the steel fiber volume in the concrete improves the impact load resistance, particularly blast resistance. Also, Ranade et al. [33] mentioned more than 3% of the steel fiber dosage is beneficial to improve the impact loading resistance, yet the better compatibility between tension-softening of the concrete and the reinforcement steel would improve the performance related to impact (or blast) loading.

In addition to structural performance, abrasion resistance is a key factor in the service life of concrete crossties. Shurpali et al. [34], [35] noted that while conventional approaches focused on pad design and fastening systems to reduce wear, modifying the concrete itself, through non-air-entraining mixtures, steel fiber inclusion, and metallic fine aggregates, can significantly enhance abrasion resistance. Although many studies have focused on hydraulic structures, similar strategies have been applied to improve abrasion resistance in concrete [36], [37], [38], [39], [40]. Common approaches include: (1) reducing air content, (2) incorporating supplementary cementitious materials such as silica fume, fly ash, or geopolymer, (3) adding fibers, (4) optimizing aggregate grading, and (5) applying surface treatments such as polyurea or polyurethane coatings, iron sheets, or rubber. Fundamentally, these methods enhance abrasion resistance by increasing the material's strength through careful selection of mix constituents and aggregate gradation.

Chapter 3 : Modeling Setup

Due to their complex geometry, the reinforcement (tendons) were first modeled on a 3D CAD Software, SolidWorks, before they were imported and assembled with the concrete section of the models for mesh generation. This study used ABAQUS to generate the mesh of concrete prisms or crossties with prestressing tendons. Two groups of reinforcement were created. The first group (comporting circular, square and chevron shaped indentations on the various tendons and a smooth tendon) was mainly used on 4in long (small) models, destined for pullout analysis. While the second group comprising of three tendons, two chevron indented (chevron WG and WP) plus a smooth tendons, was used on 34.5in long (intermediate) and on 51in long (full size) models and was destined for prestress analysis (detensioning). The geometrical parameters defining indentation of prestressing wires are shown in Figure 3.1, where *a* is the depth of indentation in prestressing wires which the concrete bonds to, P is the nominal pitch, and L is the nominal length. The pitch and the length are given as they allow the dimensions to be applied to a variety of shapes.

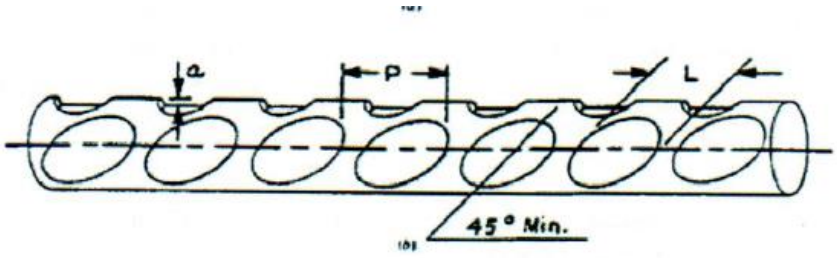

Figure 3.1 Wire Model Dimension [41].

Kansas State University has been studying the various effects of prestressing wires and prestressed concrete crossties by testing their performance. One of their remarkable contributions to the profession was the development of 3D scanning technology to quantify the indentation characteristics of existing prestressing wires. Figure 3.2 shows the different prestressing wires adopted in their study [42].

The specific dimensions for each of the wire models are summarized in Tables 3.1 – 3.4. Among the four basic shapes from the first group (small concrete prism models) in Tables 3.1 and 3.2, there were certain varied dimensions, meaning 13 models were created in total, which were used for the elastic model analysis (Pullout test). The tendons for larger size concrete prism models from the second group were modeled using measurements provided by laser scanning the real tendons in Tables 3 and 4 [42].

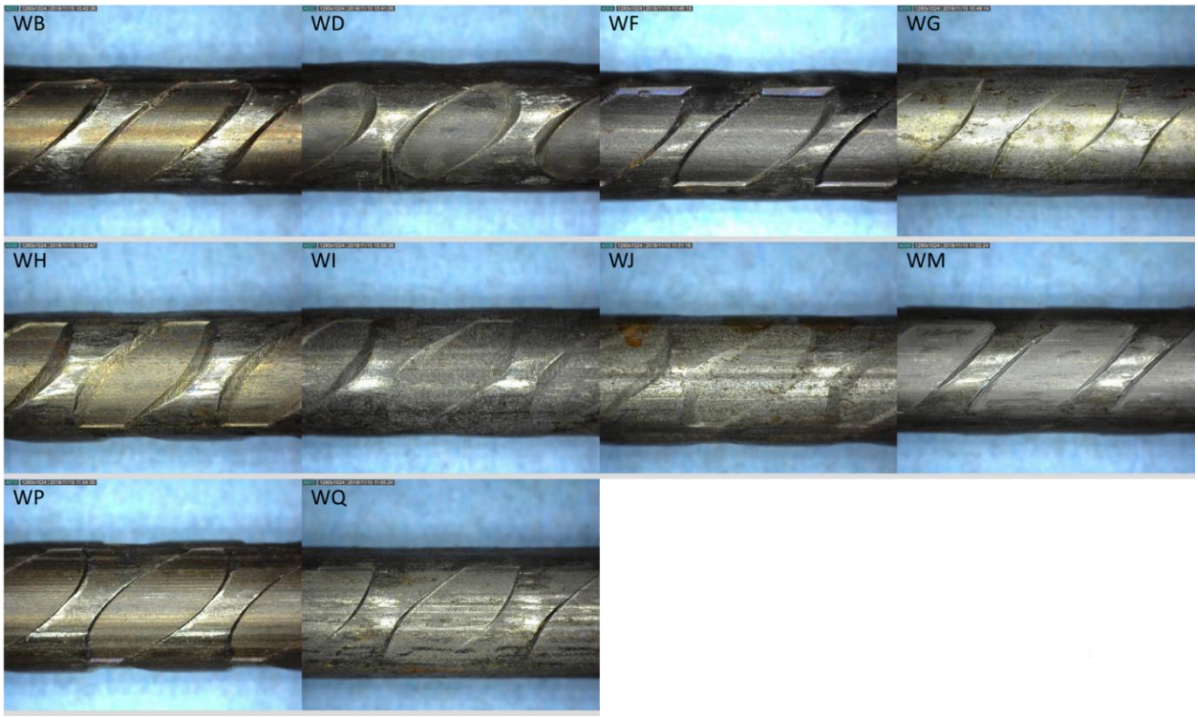

Figure 3.2Tendon Indentation Examples [42].

Table 3.1 Wire model dimensions and geometrical properties.

Shape	Total Length	Diameter	Nominal Length (L)	Pitch (P)	Depth (a)	Side Angle
	in	in	In	in	in	degree
Circle	4	0.2094	0.138	0.215	0.0045	90°
Chevron	4	0.2094	0.138	0.215	0.0045	90°
Chevron (Single Reverse)	4	0.2094	0.138	0.215	0.0045	90°
OSquare	4	0.2094	0.138	0.215	0.0045	90°
OSquare_T60	4	0.2094	0.138	0.215	0.0045	60,90,60,90
OSquare_T90	4	0.2094	0.138	0.215	0.0045	90,60,90,60
CSquare	4	0.2094	0.138	0.215	0.0045	90°
Chevron_WG	4	0.2094	0.138	0.215	0.0026	10.56°
CSquare_Rotated30	4	0.2094	0.138	0.215	0.0045	90°
Smooth	4	0.2094	--	--	--	--

Table 3.2 Wire geometrical properties.

Shape	**Wall Area**	**Cut Area, base**	**Surface Area**	**Volume**	**V/d**
	in^2	in^2	in^2	in^3	in^2
Circle	0.00193	0.01431	0.01624	6.37E-05	0.01415
Chevron	0.00354	0.02641	0.02995	1.17E-04	2.02596
Chevron (Single Reverse)	0.00354	0.02641	0.02995	1.17E-04	0.02596
OSquare	0.00218	0.01431	0.01649	6.59E-05	0.01464
OSquare_T60	0.00236	0.01431	0.01667	6.59E-05	0.01464
OSquare_T90	0.0024	0.01477	0.01717	6.59E-05	0.01464
CSquare	0.00296	0.02641	0.02937	1.22E-04	0.02701
Chevron_WG	0.00814	0.01985	0.02799	6.24E-05	0.02402
CSquare_Rotated30	0.00296	0.02641	0.02937	1.22E-04	0.027
Smooth	--	--	--	--	--

Table 3.3Wire model dimension and Geometrical properties.

Shape	Total Length	Diameter	Nominal Length (L)	Pitch (P)	Depth (a)	Side Angle
	in	in	in	in	in	degree
Smooth	34.5 & 51	0.2094	--	--	--	--
Chevron_WG	34.5 & 51	0.2094	0.138	0.215	0.0026	10.56°
Chevron_WP	34.5 & 51	0.2094	0.138	0.215	0.0046	29°

Table 3.4 Wire geometrical properties.

Shape	Wall Area	Cut Area, base	Surface Area	Volume	V/d
	in^2	in^2	in^2	in^3	in^2
Smooth	--	--	--	--	--
Chevron_WG	0.00633	0.01631	0.02264	4.64E-05	0.01785
Chevron_WP	0.00535	0.01941	0.02473	1.06E-04	0.02304

After completing the models, they are saved as .IGES files. IGS files are based on the Initial Graphics Exchange Specification standard, common in many computer-aided drawing applications.

Classified respectively under their group each of the models are shown in Figure 3.3 through Figure 3.8.

Small Scale Prestressing Tendon Models

The basic shapes under investigation are circle, chevron, square and smooth, where each additional model is a variant of one of these shapes. The circular model can be seen in Figure 3.3.

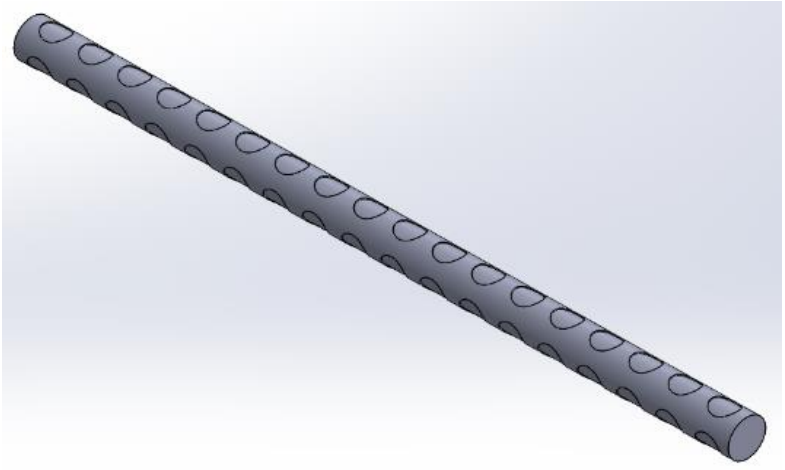

Figure 3.3 Circular Pattern 3D Numerical Model

The chevron and chevron (single reversed) are the shapes shown in Figure 3.4a and Figure 3.4b, respectively. In the single reversed model, one of the three bands of cut pattern is rotated 90° to better mimic the typical product. There is no other dimension variation between the two. However, both of these models still have the practical limitation of a 90° sidewall, a manufacturing implausibility. To better simulate realistic conditions another chevron model, the WG model shown in Figure 3.5, was created. It was modeled just as the models of the second group based on the measurements provided by laser scanning the real tendon for its dimensions[42] . As shown in Table 2, the depth of the cut is a very shallow 0.0026 inches and a very gentle side angle of 10.56°.

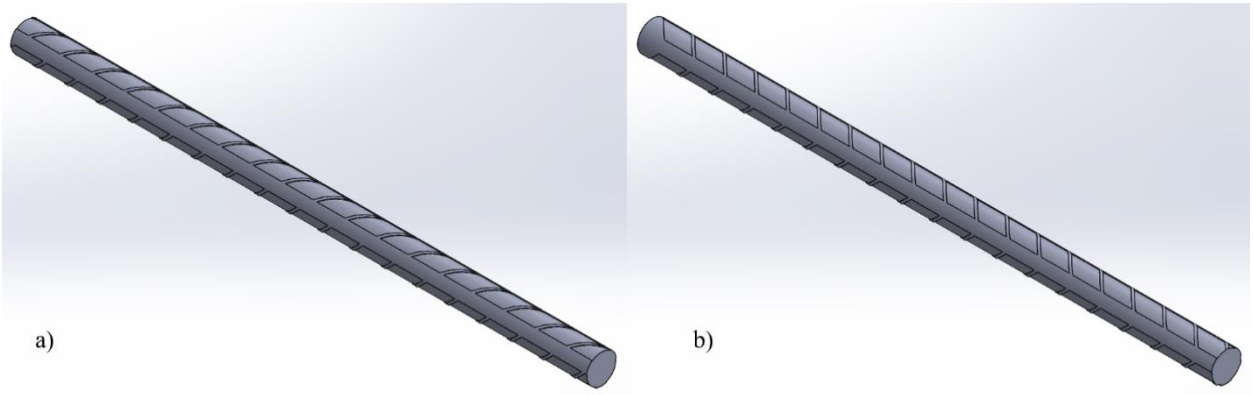

Figure 3.4 Chevron (a) and Chevron, Single Reversed (b) 3D CAD Models

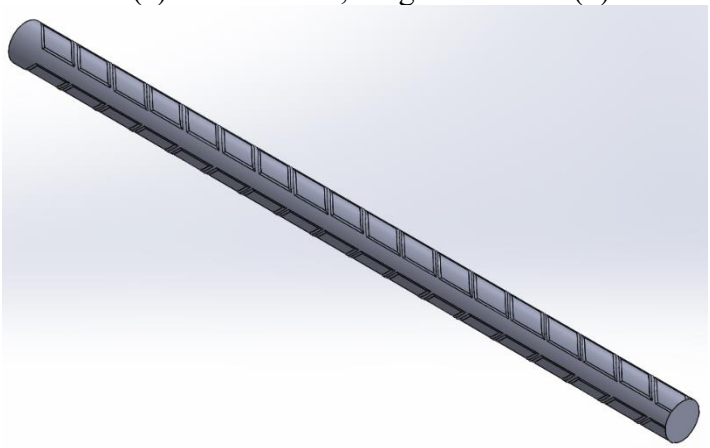

Figure 3.5 Chevron WG 3D CAD Model

The CSquare and OSquare are square cut patterns with the base area as the chevron and circle respectively. This was an intentional factor to help indicate the effect of area on the model response. These models can be compared in Figure 3.6. The OSquare model also had a slight variation in its side angle. One model had the top and bottom (when looking at the model with the longitudinal direction going left to right) chamfered at 60° with the left and right at 90°, while another had all sides at 90°. This consideration was because the test conducted was a pullout test with a force being applied in the longitudinal direction of the tendon. Therefore, to test if the indentation side angle does have an impact on the model, different side angles are created on walls in the longitudinal direction (left and right) than those on the circumferential direction (top and bottom).

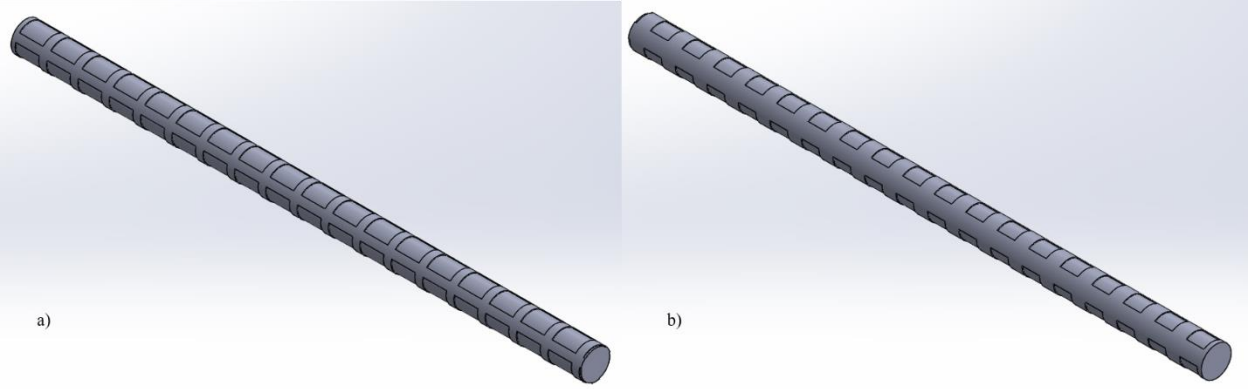

Figure 3.6 CSquare (a) and OSquare (b) 3D CAD Model Comparison

To somewhat mimic the chevron pattern, without the complexity of the geometry, the CSquare model was also rotated 30°. This rotation was chosen – as opposed to the 45° tilt on the chevron model – because the center-to-center spacing between cuts was intentionally kept constant and a 45° rotation would have the ends of the cuts overlap. The CSquare rotated 30° model is shown in Figure 3.7. This model was intended to highlight the effect of area as well as the effect the shape has on the response of the model.

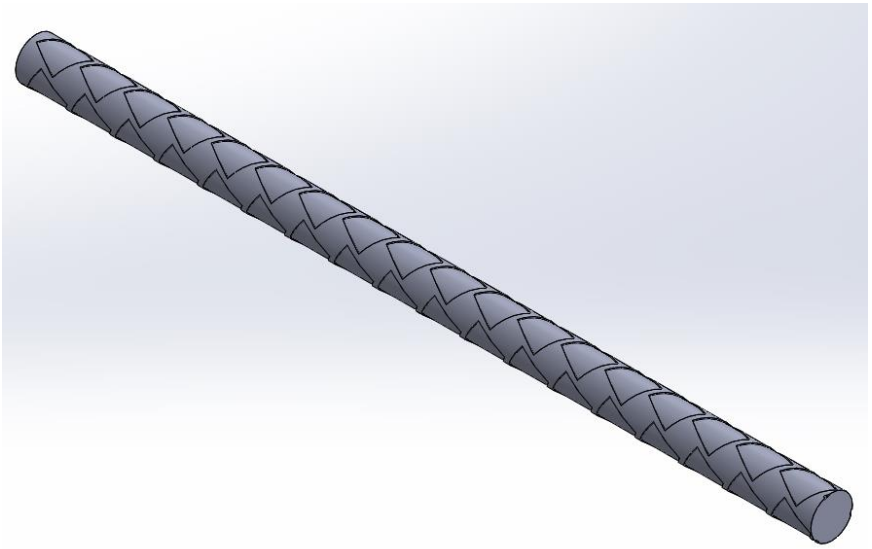

Figure 3.7 Csquare Rotated 30° 3D CAD Model

Larger-scale Prestressing Tendon Models

For the second group of tendons, which were used for the prestress analysis on the intermediate (34.5 in.) and full-size (51 in.) models. We decided to create three (3) different tendons. We made sure the three tendons we chose were very distinct in terms of their characteristics, in order to cover a wide range of indentations. The main characteristic that varied from tendon to tendon are the indentations. These indentations varied in size, shape and side wale angle. As depicted in Figure 3.8 from left to right the three tendons were the smooth tendon (WA) with no indentations,

the chevron patterned shallow indented tendon (WG) and the chevron patterned deep indented tendon (WP).

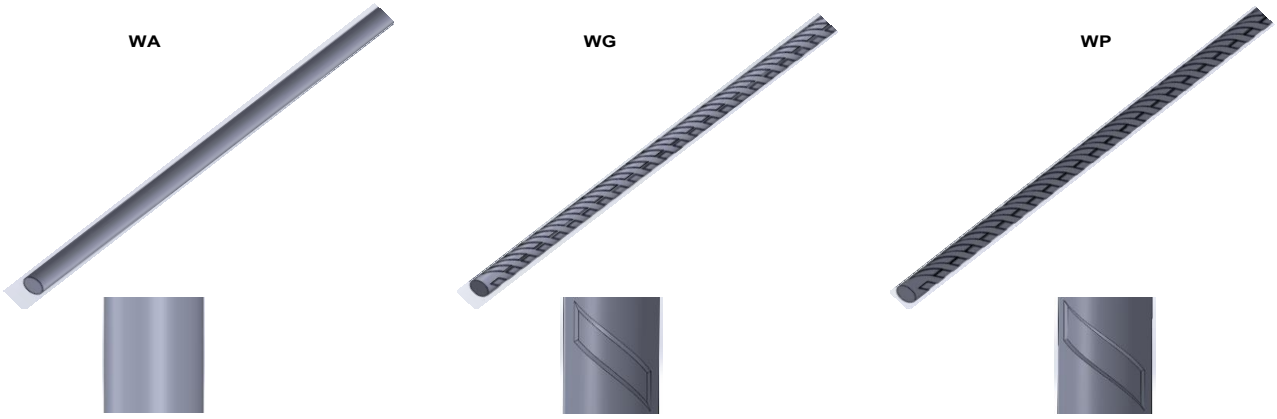

(a) (b) (c)

Figure 3.8 3D CAD wire models: (a) Smooth WA, (b) shallow-Chevron WG, and (c) deeper chevron WP.

3.1 Mesh

One of the most important considerations of the project is the appropriate meshing of the parts. Abaqus is used to generate mesh of the numerical models after importing 3C CAD files.

3.1.1 Separating the Pieces: Zoning

"Zoning" is a modeling technique that involves dividing a geometry into discrete parts to optimize the mesh generation process. Typically, complex systems require partitioning when different regions serve different functions or require different levels of analysis accuracy. In finite element modeling, regions with complex geometry or high stress concentrations require a much finer mesh than vast regions of monotonous, low-stress material.

To address this, the model was divided into five distinct sections:

- Coarse Concrete: The block periphery.
- Fine Concrete: The block immediately surrounding the interface zone.
- Intermediate Zone: The transition area between the fine and coarse concrete.
- Fine Steel: The tendon perimeter around the interface zone.
- Coarse Steel: The interior core of the tendon.

The first critical step involves separating the coarse interior of the reinforcement from the fine exterior section. The size and shape of this partition are dictated by element size requirements (detailed in Section 3.2.2). Since the bulk of the analysis focuses on the interface zone around the wire's circumference, the initial approach for small models (4-inch prisms) involved a circular partition concentric with the tendon. However, for intermediate and full-size models, a polygonal partition proved more effective for two reasons. First, a polygon provides distinct edges that

facilitate "seeding" (defining node density) compared to a circle. Second, it allows for better control over the total element count; this is crucial as the commercial software, ABAQUS CAE, tends to crash when the total element count exceeds a specific threshold (approximately 268,000,000 elements).

The wire features a nominal (uncut) diameter of 0.2094 inches (R_1 ~ 0.1047"). Three rows of indentations along the perimeter, each 0.0045 inches deep, reduce the actual diameter to 0.2004 inches (R_2 ~ 0.1002"). The partition for the interior section of the reinforcement on the small models was set at a maximum radius of R_3 ~ 0.098".

Regarding mesh density, a fine mesh element size of approximately 0.002 inches was achieved on the small models. However, to adhere to the element count constraints mentioned above, the fine mesh size on intermediate and full-size models was adjusted to 0.0041 inches. Both sizes yielded satisfactory results, ensuring at least two rows of elements were generated along the depth of each indentation and four rows along the side walls.

Because the interface zone represents the critical interaction between the concrete block and the steel, a partition is necessary around the outer diameter of the tendon (visible in Figure 3.9 as "Fine, concrete"). Similar to the steel partition, this section provides high-resolution data in the assembly's most impactful area. Ideally, there should be a minimum of two layers of elements surrounding the steel. For a nominal tendon diameter of 0.2094 inches (R_1 ~ 0.1047"), the partition diameter must be at least 0.2174 inches (R_4 ~ 0.1087"), though it is typically extended to R4 ~ 0.1107".

A final partition is created between the block periphery (Coarse) and the fine interface zone. This "Intermediate Zone" acts as a transition area. While the block edges experience minimal stress and can utilize large elements, the mesh must refine as it approaches the tendon. Creating this intermediate partition—typically placed around 0.25 inches from the center (R_5 ~ 0.25")—allows for optimization between analysis quality and file size, smoothing the transition from coarse to fine elements.

For larger models, datum planes—orthogonal reference planes offset from major axes—were essential for successful meshing. When mesh alignment errors occur at boundaries, the solution typically involves adjusting mesh density or partitioning the section with datum planes. In this study, both solutions were implemented; longitudinal datum planes partitioned sections, while horizontal datum planes split the model's length.

Once partitions are created, each zone is assigned a "set." While the five zones described above are useful for organization, efficient parallel computing requires minimizing the number of distinct sets. Therefore, for the final analysis, the model was consolidated into just two material sets: Set 1 (Concrete) and Set 2 (Rebar, meaning tendon).

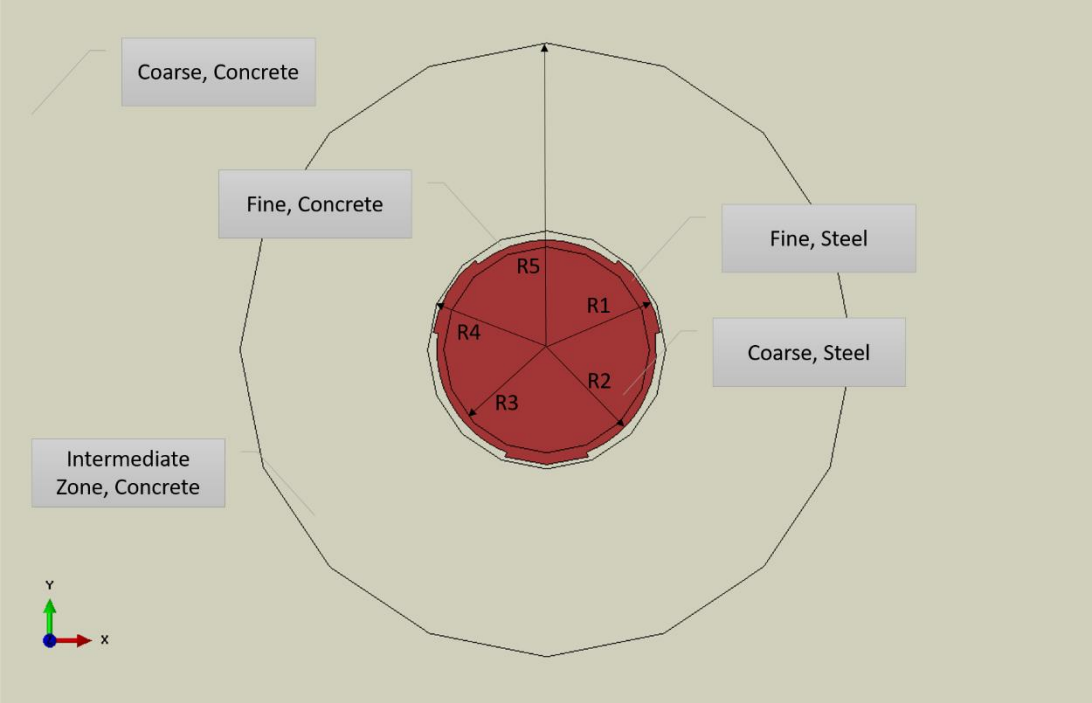

R1 = 0.1047”
R2 = 0.1002”
R3 < 0.098”
R4 > 0.1087”
R5 ≈ 0.25"

Figure 3.9 Partition Zone Labels (Small scale model)

On the larger models, as previously mentioned a polygon shaped partition was used as interior of the tendons and outer edge of the Fine Concrete. Different shapes were used in the process of trying to find the best fit in terms of meshing for each model, mainly rectangular and octagonal. As seen on the Figure 3.10-(a) rectangular shape was used as the inner edge of the fine steel and circular shape as the outer edge of the of the fine concrete for reinforced quarter crosstie embedded by the Chevron WG, whereas both edges were octagonal for the reinforced quarter crosstie embedded by the smooth and Chevron WP tendons.

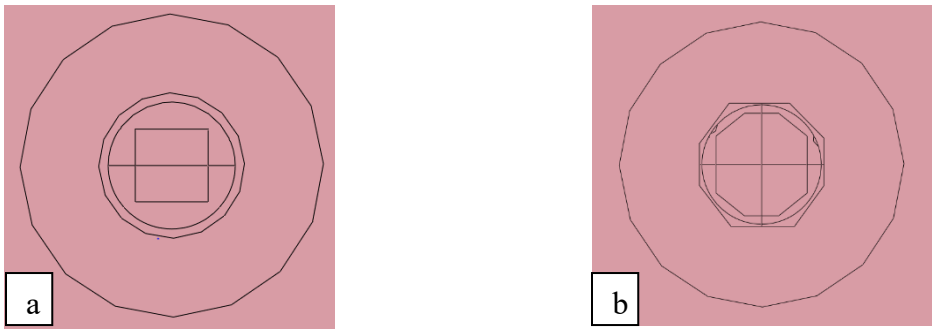

Figure 3.10 (a) Zones on Prestressed Concrete (PSC) WG Model and (b) Zones on Prestressed Concrete (PSC) WA&WP Models

Different sections of the reinforced concrete will require a different resolution of data points. Therefore, in order to optimize the final file size with the accuracy of the model, a one-size-fits-all seeding arrangement must be dismissed in favor of local seeds. Local seeds allow the user to apply element sizes in relation to the geometry. For example, Figure 3.11 shows the local seeding for the fine mesh of the tendon around the interface zone, and the coarser mesh on the interior of the bar. The nodal points are depicted by purple triangles when the seed is applied. Note the size difference between elements and nodal spacing on the inner radius versus those on the outer.

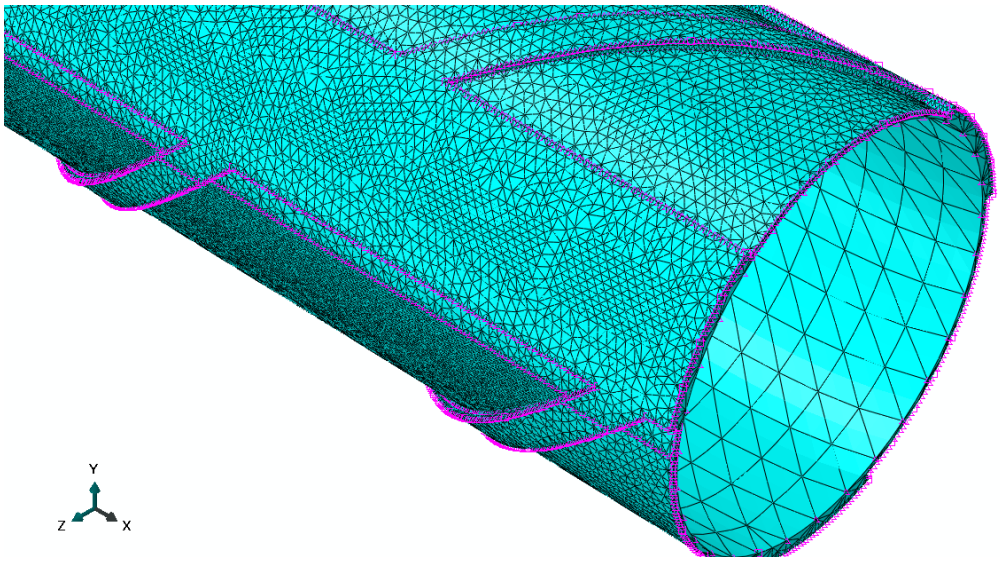

Figure 3.11 Local Seeds of Chevron Reinforcement at the Interface Zone

As previously discussed, the interface zone governs the interaction between the steel and concrete, necessitating a significantly finer mesh. To ensure high-confidence results, the mesh topology required multiple rows of elements along both the walls and the depth of the wire indentations.

Table 3.5 lists the radii and respective thicknesses for the various zones discussed in Section 3.2.1. These zone thicknesses were calculated to establish a standard "Zone Thickness to Approximate Element Size" ratio (Table 3.6), which serves as a guideline for future modeling efforts. The approximate element sizes presented in Tables 3.6 and 3.7 were determined through a rigorous mesh sensitivity analysis (iterative meshing and re-meshing). Once the optimal element size was identified, reliable refinement ratios could be computed for each zone. For instance, given a zone thickness of 0.0153 inches in the "Fine Concrete" region, reliable results required an element size approximately eight (8) times smaller than the thickness for small models, and four (4) times smaller for large models. CS stands for Coarse Steel, FS for Fine Steel, FC for Fine Concrete, IC for Intermediate Concrete, and CC for Coarse Concrete.

Table 3.5 Set Radius and Thickness

	Radius from center of tendon (in)	Zone Thickness (t) (in)
CS:R3	0.09	0.09
FS:R1	0.1047	0.0147
FC:R4	0.12	0.0153
IC:R5	0.25	0.13
CC:R6	1	0.75

Table 3.6 Approximate Element Sizes by Zone (Pullout)

Zone	Approximate Element Size {E}	Approximate advisable ratio to expect good results per zone (t/E)
Coarse, Steel	0.02	4.5~5
Fine, Steel	0.002	7.35~7
Fine, Concrete	0.002	7.65~8
Intermediate Zone, Concrete	0.02	6.5~7
Coarse, Concrete	0.2	3.75~4

Table 3.7 Approximate Element Sizes by Zone (Prestress)

Zone	Approximate Element Size {E}	Approximate advisable ratio to expect good results per zone (E/t)
Coarse, Steel	0.029	3.10~3
Fine, Steel	0.0041	3.59~4
Fine, Concrete	0.0041	3.73~4
Intermediate Zone, Concrete	0.02	6.50~7
Coarse, Concrete	0.07-0.5	10.71~11

Table 3.8 details the mesh variations across the four-inch models. It should be noted that earlier model iterations lacked the specific "coarse versus fine" partitioning of the tendons, resulting in lower element totals. Additionally, the smooth wire models contain no indentations and were meshed coarsely throughout, yielding a significantly lower element number.

Conversely, larger models with WA, WG, and WP tendons registered a very high number of elements (Table 3.9) due to the decreased element size required at the interface. This massive element count strained the computational resources; to prevent ABAQUS from crashing during the meshing process, the "Show native mesh" feature in the View tab had to be deactivated to reduce the graphical rendering load. Across all simulations, the models maintained an element-to-node ratio between 5 and 6, indicating that each node is shared by five to six elements on average.

Table 3.8 Number of Nodes and Elements in Each Small Model

Shape	Number of Nodes	Number of Elements
Circle	846,927	4,204,557
Chevron	729,389	3,670,678
Chevron (Single Reverse)	282,511	1,698,963
OSquare	205,506	1,230,563
Osquare_T60	220,126	1,314,998
Osquare_T90	247,128	1,476,912
Csquare	217,531	1,304,018
Chevron_WG	1,551,952	8,850,816
CSquare_Rotated30	232,594	1,396,301
Smooth	27,157	160,495

Table 3.9 Number of Nodes and Elements in Each Larger Model

Shape	Number of Nodes	Number of Elements
PSC WA	26,374,196	136,698,500
PSC WG	41,877,435	235,047,309
PSC WP	48,960,188	268,223,102

3.1.3 Element Shape

Finite element shapes are selected based on geometric topology and the required level of analysis accuracy. In this study, the tetrahedral element family was selected for this analysis due to its superior ability to conform to complex geometries, such as the indented surface of the prestressing wires.

Within the tetrahedral family, two specific formulations were utilized based on the computational resources available and the stage of analysis:

1. C3D10 (Quadratic Tetrahedron): This is a 10-node modified quadratic tetrahedron. It provides significantly more refined stress data and captures complex behavior more

accurately than linear elements. However, due to the higher node count per element, using C3D10 elements in models with millions of elements drastically increases the degrees of freedom and, consequently, the calculation time.

2. C3D4 (Linear Tetrahedron): This is a 4-node linear tetrahedron. While less precise than the quadratic formulation, it is computationally efficient and sufficient for geometry checks and preliminary calculations, particularly in regions with extremely high mesh densities.

For valid finite element analysis, elements sharing a boundary must typically share coincident nodes to ensure proper load transfer. While mesh blending tools exist to transition between different element shapes or orders, no such techniques were employed in this study to avoid potential continuity errors. Instead, a consistent tetrahedral mesh topology was maintained throughout.

The project adopted a hybrid processing strategy to balance accuracy with efficiency: C3D4 (linear) elements were utilized during local processing for mesh generation and model verification, while C3D10 (quadratic) elements were utilized for the final high-fidelity numerical analyses performed using the parallel computing algorithm on the supercomputer.

3.2 Material Properties

3.2.1 Properties of Steel

Steel is assumed not to yield and only has elastic property definitions. The material properties of the steel are shown in Table 3.10.

Table 3.10 Elastic Properties of Steel

Young's Modulus (E_{steel}, ksi)	Poisson's Ratio (ν_{steel})
30,000	0.32

3.2.2 Properties of Concrete

Like steel, the elastic properties of concrete can be defined by two inputs: Young's Modulus and Poisson's Ratio. The Young's Modulus (E_0), can be defined by the empirical relationship with the compressive strength (f'_c) of the concrete, provided by ACI Code 8.5.1 [43]

$$E_0 = 57{,}000 * \sqrt{f'_c} \tag{3.1}$$

The compressive strength of the concrete is taken to be 5000~12,000 psi. The Poisson's Ratio (ν) is taken to be 0.15.

The concrete damaged plasticity (CDP) model allows for analysis of the nonlinear behavior of concrete. The two major components are the analysis of damage (from microcracking, coalescence, and decohesion, etc.) and plasticity (strain softening, progressive deterioration, and volumetric expansion, etc.).

ABAQUS includes many detailed inputs for the model; for this CDP model there will be three sections of focus: plasticity, compressive behavior, and tensile behavior. The plasticity parameters are shown in Table 3.11 and include more general terms like dilation angle, eccentricity, f_{b0}/f_{c0}, K, and the viscosity parameter [44].

Table 3.11 Plasticity Parameters for Concrete Damaged Plasticity Model.

Dilation Angle (ψ)	**Eccentricity (ϵ)**	$\frac{f_{b0}}{f_{c0}}$	**K**	**Viscosity Parameter (μ)**
Amount of plastic volumetric strain developed during plastic shearing	Rate at which the hyperbolic flow potential approaches its asymptote	Ratio of initial equibiaxial compressive yield stress to initial uniaxial compressive yield stress	Ratio of the second stress invariant on the tensile meridian, $q_{(TM)}$, to that on the compressive meridian, $q_{(CM)}$	Visco-plastic regularization of the concrete constitutive equations

The next section of the model is the compressive behavior of concrete. In this section ABAQUS seeks an experimental stress-inelastic strain relationship and includes the degraded modulus of elasticity and damage factors associated with plastic strains. CDP defines the inelastic region as the total strain value minus the elastic strain value as:

$$\varepsilon^{in} = \varepsilon_c - \varepsilon^{el} = \varepsilon_c - {}^{f_c}/_{E_0} \tag{3.2}$$

In the inelastic region beyond the peak stress value – called the tension stiffening or strain softening stages – the concrete will unload according to degraded Young's modulus E, not the undamaged Young's modulus E_0. This behavior is visually represented in Figure 3.12, which shows typical stress-strain responses in tension (a) and compression (b).

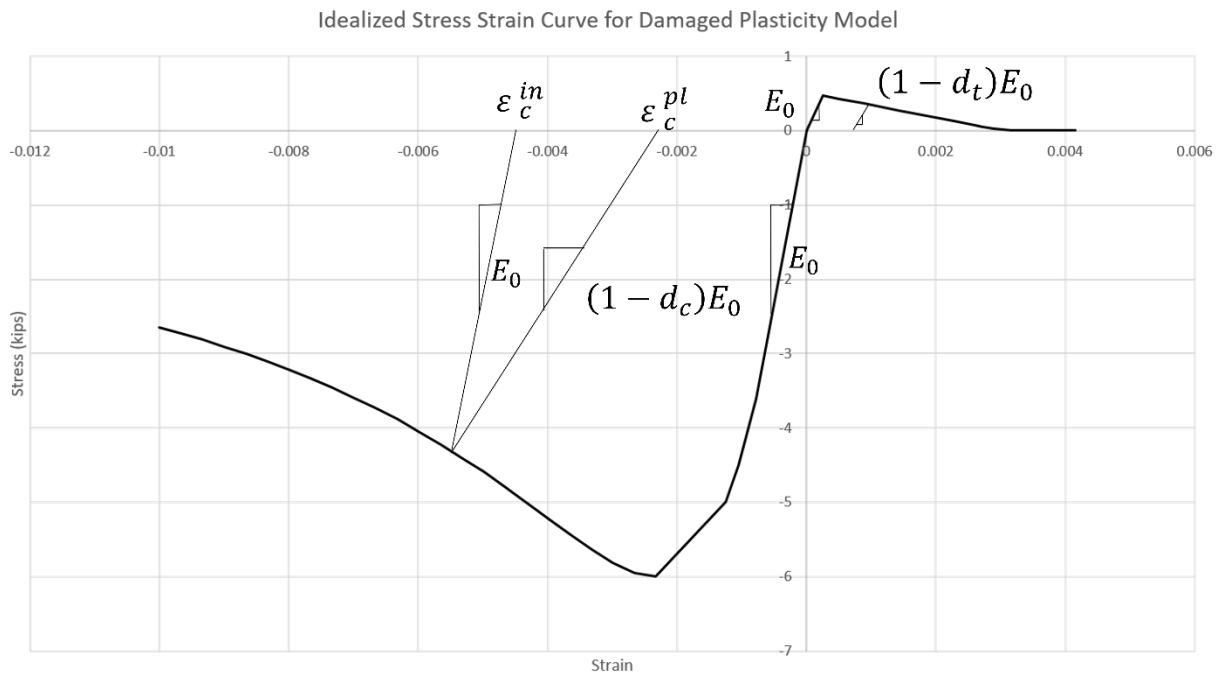

Figure 3.12 Concrete Stress-Strain Responses to Uniaxial Tension and Uniaxial Compression [44].

The degraded Young's modulus in each case is proportional to one minus some damage factor which is unique to each point on the curve as seen in Eqs. 3a and 3b:

$$E_C = (1 - d_c)E_0 \quad (3.3a)$$
$$E_t = (1 - d_t)E_0 \quad (3.3b)$$

3.3 Constraints

3.3.1 Boundary Conditions

Longitudinal Constraints: The application of longitudinal constraints varies depending on the analysis type:

- Pullout Test Models (Small Concrete Prism Model): A longitudinal restraint is applied to the "Coarse Concrete" section of the X-Y face opposite the origin (Figure 3.12a). This setup simulates the reaction face of a physical pullout test. Crucially, the "Fine Concrete" zone remains unconstrained to allow for natural deformation, stretching, and crack propagation as the tendon slides.

- Pre-stress Analysis Models: For the intermediate and full-sized models, the longitudinal boundary condition is applied to the entire cross-section of the X-Y face at the origin (Figure 3.12b, c). This serves as a symmetry boundary condition, simulating the structural continuity of the other half of the crosstie.

Lateral and Vertical Constraints: The remaining boundary conditions are consistent for both the Pullout and Pre-stress simulations. To anchor the model against horizontal displacement, a constraint is applied to the entirety of the Y-Z face. Careful consideration was given to Poisson's effect; since axial compression induces lateral expansion, constraining all lateral faces would result in an over-constrained model with unrealistic confinement stresses. Finally, vertical movement is restricted on the bottom surface (Z-X face).

These boundary conditions, visually represented by the orange cones in Figure 3.12, function together to replicate the boundary physics of the real-world environment as accurately as possible.

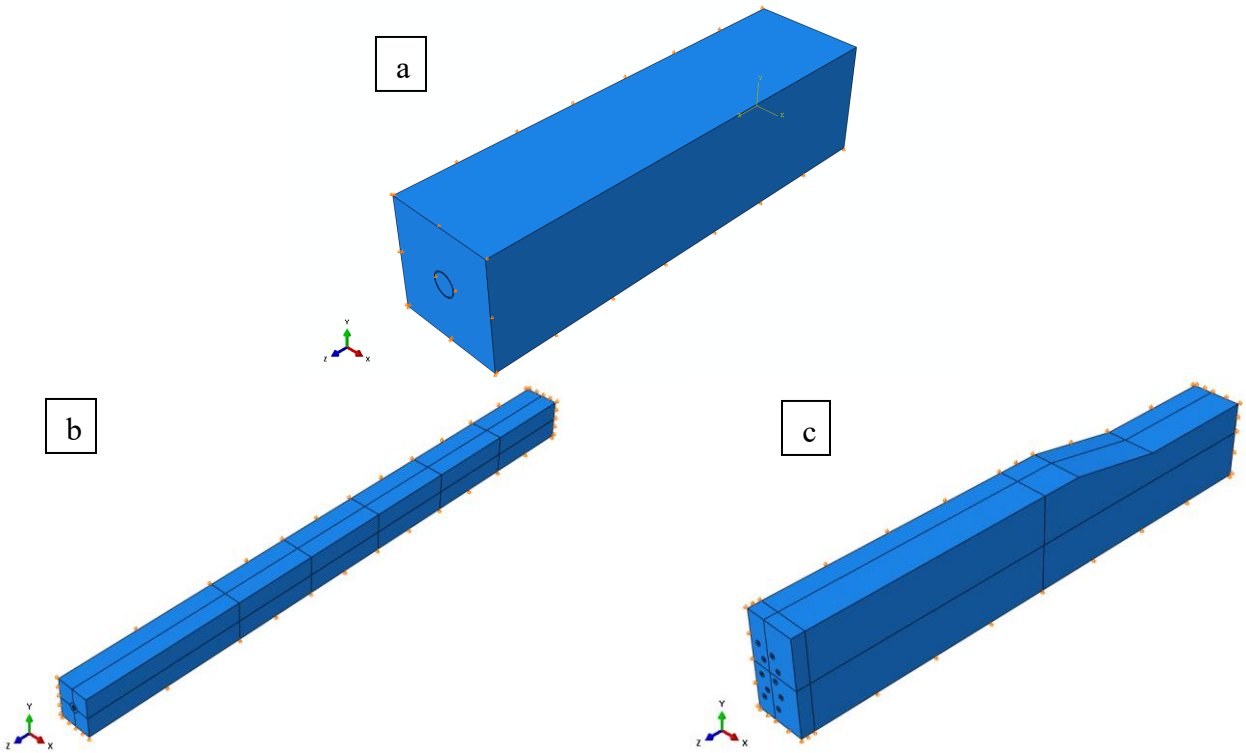

Figure 3.13 Boundary condition of Reinforced Block (a) Small (b) Intermediate (c) Full size
Boundary conditions are shown in Figure 3.12 (a) through (c) with the direction in which displacement is equal to zero, a roller. Note that none of these boundary conditions restricts rotation about an axis. The tendon is not fixed at any point. This is important because, in addition to sliding, the radial expansion of the tendon due to longitudinal compression from pretensioning will be vital during the analyzation of the interface zone due to the role it plays in the bond strength of steel and concrete.

3.3.2 Prestress and External Load

Prestressing the concrete is a simple process in modeling terms. Like the boundary conditions, prestress is assigned at the initial state of the model as a predefined variable. A stress of 203 ksi is applied in tension along the longitudinal axis (Z-axis in Figure 3.13- (a) through (c))

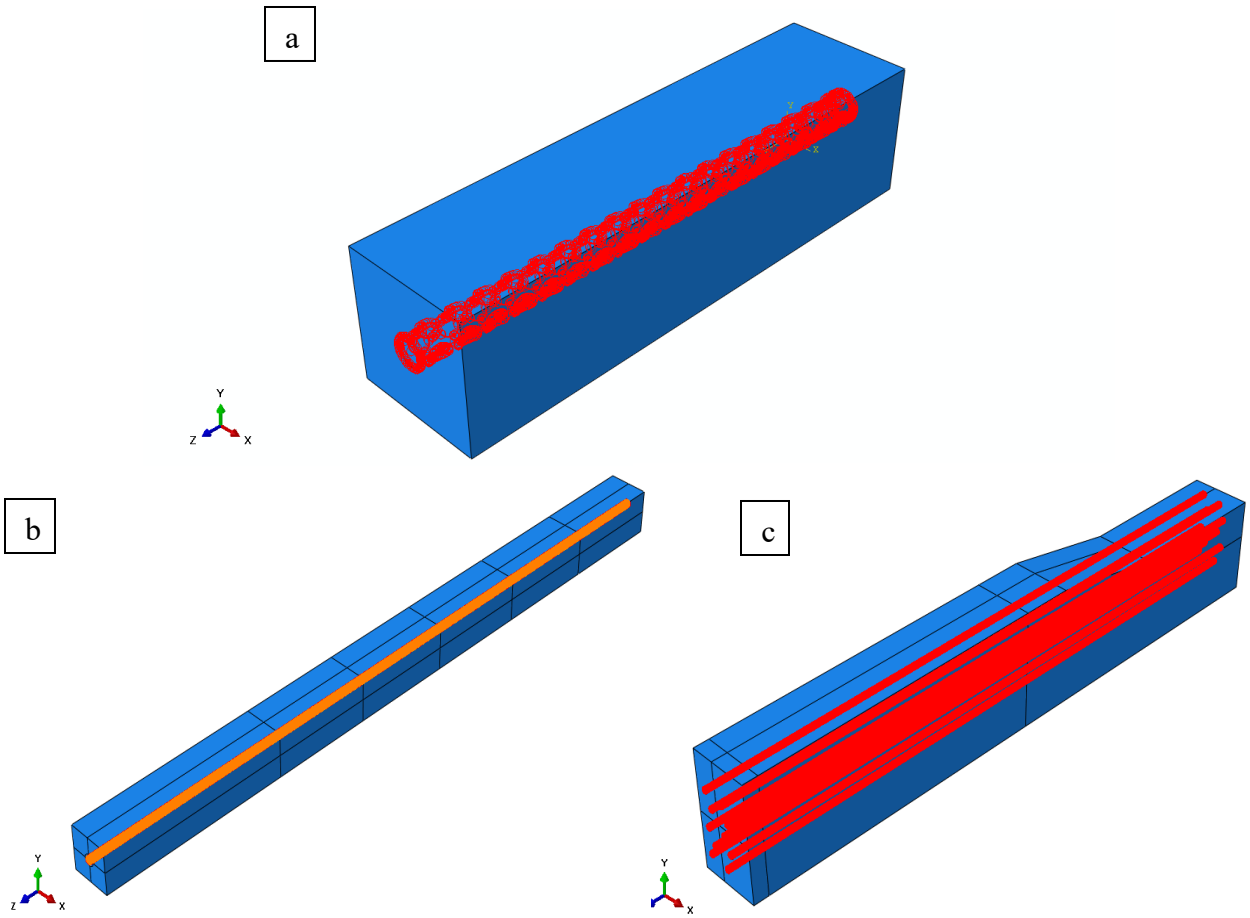

Figure 3.14 Prestressed Member in Reinforced Concrete (a) Small (b) Intermediate (c) Full size

In ABAQUS static analysis, the external load can be applied in a number of ways. For the elastic model which will be covered in Section 5.1 The Elastic Model, there are multiple control tests which explore each of these methods. The first is to apply a displacement control. This is also applied as a boundary condition, but unlike those described above it is applied during the analysis step. Additionally, the displacement is only applied to the face of the tendon opposite the origin and is nonzero. This is shown as orange arrows in Figure 3.14. Another method is force or pressure control, in which loads can be applied as a pressure on the entire face of the tendon. The pressure is applied under the load tab on ABAQUS. The results of these loading scenarios are explored in chapter 5.

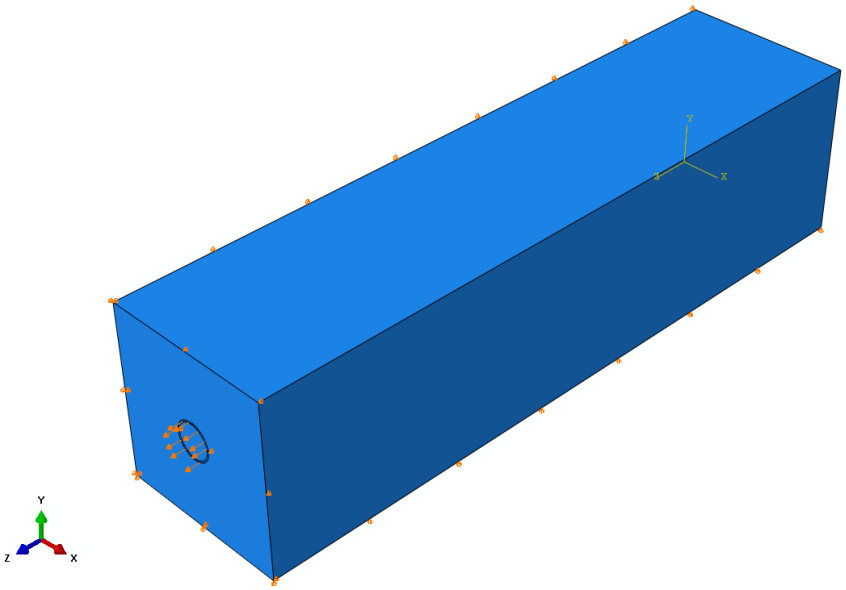

Figure 3.15 Displacement Control Loading (Pullout)

Chapter 4 : Parallel Computing

4.1 Transforming the Model

The model created in Abaqus is only used for the generation of the mesh and the text file (.inp file) containing the geometric points of the nodes in the mesh. This file then requires a host of software packages and some creative file conversions to analyze the input and visualize the response. A general walkthrough of the process is as follows in Figure 4.1:

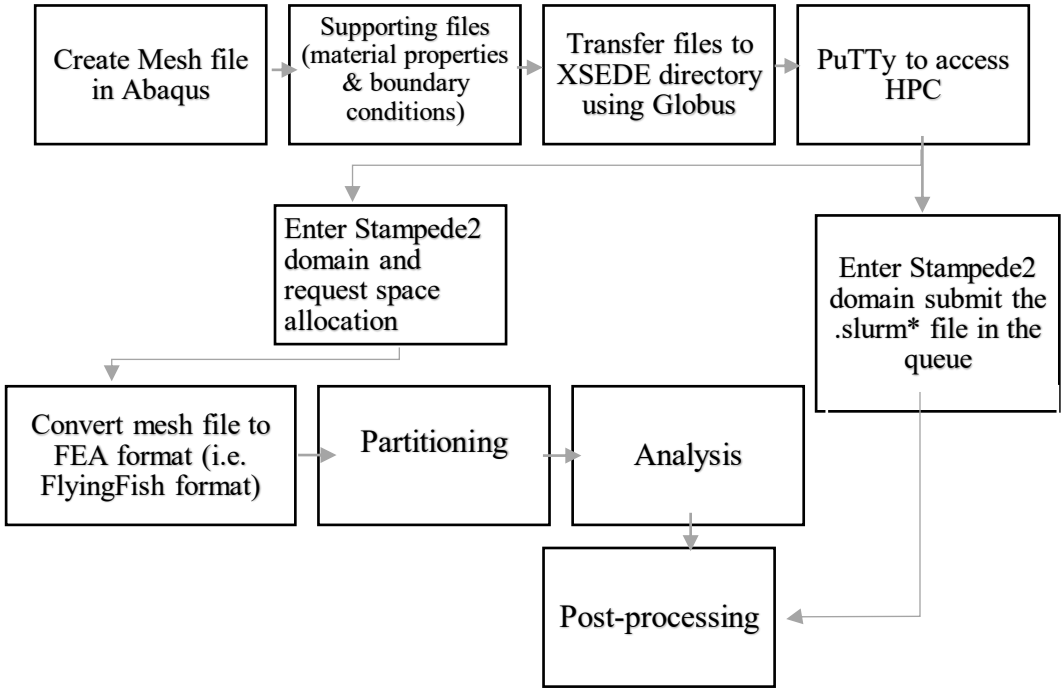

Figure 4.1 Parallel Computing Steps

The computational workflow begins by establishing a connection to the XSEDE research environment using a terminal emulator, PuTTY. The input files representing the meshed reinforced block are initially generated on the local network using ABAQUS. To transfer these input files and necessary supporting scripts from the local machine to the high-performance computing (HPC) environment, the Globus file transfer service is employed.

Once the data migration is complete, the simulation is executed using "FlyingFish," a parallel computing numerical simulator (in-house code developed by a research programmer when he was at the National Center for Supercomputing Applications). This finite element analysis in-house code is architected upon several advanced scientific computing libraries—specifically MPI, PETSc, and METIS—to optimize parallel processing efficiency. Upon completion of the analysis, the resulting solution output files (.VTK format) are visualized and interpreted using the ParaView visualization toolkit [45].

4.2 Numerical Analysis Using a Parallel Computing Algorithm

4.2.1 Mesh File Conversion

A critical pre-processing step involves converting the mesh input file into a format compatible with the finite element analysis in-house code for parallel computing. This operation is executed within the Stampede2 terminal environment. Stampede2 utilizes Intel Xeon Platinum 8160 ("Skylake") nodes; consequently, the processing queues are designated with the 'skx' prefix.

Two primary queues are available for these tasks: `skx-dev` and `skx-normal`. While the initial input conversion can technically be executed in either queue, this walkthrough assumes a consolidated workflow where file transformation and numerical analysis are performed sequentially in a single job submission. Therefore, the `skx-normal` queue is selected to accommodate the full duration and resource requirements of these combined processes.

idev –p skx-normal –N **X** –n **Y** –m **Z**

In this command structure, **X** and **Y** represent the user-defined parameters for resource allocation, where **X** denotes the number of compute nodes and **Y** denotes the total number of processor cores. The variable **Z** specifies the requested runtime duration in minutes. Upon the execution of this command, the session transitions to the allocated high-performance computing (HPC) environment, where all subsequent instructions are processed. To prepare the model for simulation, the standard ABAQUS input file must be converted into the proprietary Flying Fish format (.ff). This conversion is initiated using the following command:

login1$ ibrun –n **Y** ./FlyingFish –task INP2FF –inp **InputFileName**.inp

Where **Y** is again the number of cores ($1 < \mathbf{Y} < 48*\mathbf{X}$, due to there being a maximum of 48 cores per node). Unlike the analysis step, simply converting the input file is not computationally taxing, and requires a minimal number of cores. The result of this line is a file with the same name as the input file, but with the extension .ff.

4.2.2 Partitioning

In order to utilize multiple cores, the input file needs a partition. In this case, the partition allows different cores to analyze different pieces of the file concurrently, dramatically increasing the processing speed. The partition is performed with the nparts command shown below:

login1$ ibrun -n **X** ./FlyingFish -task FFPART -inp Input_File_Name.ff -nparts **Y** –reordering

where **X** is again the number of cores and **Y** is the number of parts that the model will be divided into.

Again, the queues entered during the simulation are all in the SKX node type domain. Table 4.1 shows the core and node information for the two domains this research is done in. Skx-dev is used only during the file transformation stage. It has a much shorter wait time and less than, but still sufficient power compared to the skx-normal queue. The shorter wait to get into the queue is

helpful when the less taxing stages of the analysis need to be conducted. Even when conducting the analysis, if the file is small (like a test file) 192 cores is enough to conduct the analysis.

Table 4.1 Queue, Node, and core Information [46].

Queue Name	Node Type	Max Nodes per Job (assoc'd cores)*	Max Duration	Max Jobs in Queue*	Charge Rate (per node-hour)
development	KNL cache-quadrant	16 nodes (1,088 cores)*	2 hrs	1*	0.8 Service Unit (SU)
normal	KNL cache-quadrant	256 nodes (17,408 cores)*	48 hrs	50*	0.8 SU
large**	KNL cache-quadrant	2048 nodes (139,264 cores)*	48 hrs	5*	0.8 SU
long	KNL cache-quadrant	32 nodes (2,176 cores)*	120 hrs	2*	0.8 SU
flat-quadrant	KNL flat-quadrant	32 nodes (2,176 cores)*	48 hrs	5*	0.8 SU
skx-dev	SKX	4 nodes (192 cores)*	2 hrs	1*	1 SU
skx-normal	SKX	128 nodes (6,144 cores)*	48 hrs	25*	1 SU
skx-large**	SKX	868 nodes (41,664 cores)*	48 hrs	3*	1 SU

4.2.3 Analysis

The analysis command within FlyingFish that is used to run the simulation is hereby in referred to as FFSIMU. The Linux command is as follows:

login1$ ibrun -n **X** ./FlyingFish -task FFSIMU -inp Input_File_Name.ff.p**Y** -ksp_type cg -pc_type jacobi

where **X** is the number of cores requested, which as shown in Figure 4.2, is equal to the number of partitions specified in the FFPART command. **Y** must be equal to the number of parts specified in order to examine how many cores (or CPUs) is an optimal number for the size of simulation. The four-inch long small concrete prism with about 18 million DOFs was first analyzed locally, using the local workstation and then analyzed using the FlyingFish program on the high performance computer using a varying number of cores (MPIs). In each test on the high performance computer, the model was partitioned into 1000 parts and the run time was recorded relative to the number of cores requested for the analysis. This speed up test was done on a four-inch Chevron model prestressed at 203 ksi with no external load. The results of this test are tabulated in Table 4.2 and plotted in Figure 4.2.

Table 4.2 Number of Cores Versus Time.

Mesh Nodes	Elements	Nodes Requested	Cores	Parts	Time (Sec)
6,062,431	35,876,186	25	25	1000	1003
6,062,431	35,876,186	25	75	1000	479.8
6,062,431	35,876,186	25	125	1000	311.7
6,062,431	35,876,186	25	175	1000	233.2
6,062,431	35,876,186	25	225	1000	189
6,062,431	35,876,186	25	275	1000	155.6
6,062,431	35,876,186	25	325	1000	134.7
6,062,431	35,876,186	25	375	1000	116.8
6,062,431	35,876,186	25	425	1000	110.5
6,062,431	35,876,186	25	475	1000	97.95
6,062,431	35,876,186	25	525	1000	90.71
6,062,431	35,876,186	25	575	1000	83.18
6,062,431	35,876,186	25	625	1000	75.42
6,062,431	35,876,186	25	675	1000	72.98
6,062,431	35,876,186	25	725	1000	69.58
6,062,431	35,876,186	25	775	1000	65.86
6,062,431	35,876,186	25	825	1000	60.75
6,062,431	35,876,186	25	875	1000	59.43
6,062,431	35,876,186	25	925	1000	56.46
6,062,431	35,876,186	25	975	1000	55.62
6,062,431	35,876,186	25	1000	1000	52.02

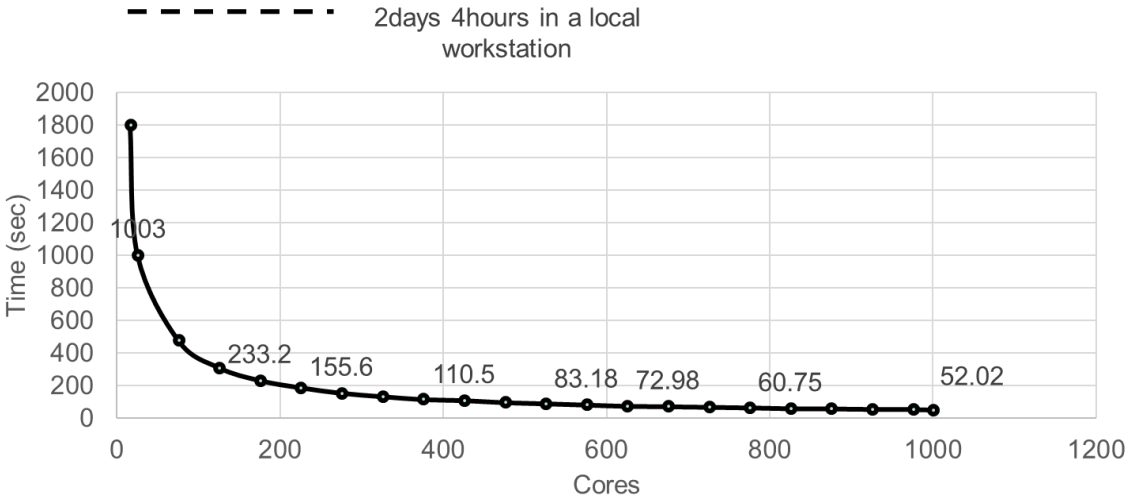

Figure 4.2 Speed up test (# Cores vs Time)

As illustrated in Figure 4.2, increasing the number of allocated cores from 2 to 1,000 on the HPC yielded a dramatic reduction in computational runtime. An analysis that previously required 2 days and 4 hours to complete on a local workstation using commercial software (ABAQUS) was accelerated to a mere 52 seconds. Given this significant improvement in efficiency, the High-Performance Computer (HPC) was utilized for the analysis of all subsequent PSCP models, proving to be both a fast and reliable computational resource.

Instead of requesting an interactive allocation cession from the stampede2 terminal, it is possible and preferable to submit the jobs on the stampede2 queue. To perform that task the following Slurm command is used:

login1$ sbatch myjobscript

Whereas "myjobscript" is the name of a text file containing #SBATCH directives and shell commands that describe the particulars of the job being submitted. The details of the job script's contents depend on the type of job intended to be run.

4.3 Postprocessing and Visualization: ParaView

ParaView is a robust visualization platform that enables the creation of custom "filters" to visualize any user-defined parameter. While the software includes a suite of standard prebuilt tools (such as Threshold, Reflect, Plot Over Line, Clip, and Slice), it also allows users to generate specialized filters using Python scripts. A prime example of this capability is the custom stress filter, which was developed internally to facilitate the stress analysis of the larger prestressed concrete prisms or crossties.

The post-processing workflow varied depending on the scale of the simulation. For smaller, test-size elastic models, visualization was primarily conducted using the native tools within ABAQUS. However, for the large-scale models analyzed using the FlyingFish software, ParaView proved to be an indispensable tool for managing and interpreting the complex datasets.

An example of the 34.5-inch, prestressed reinforced concrete member is shown in Figure 4.3. This model was subjected to a prestress of 10 ksi with and restricted longitudinally at the origin. It has been slightly modified using the warp by vector filter. This filter allows for the magnification of a certain parameter – in this case displacement.

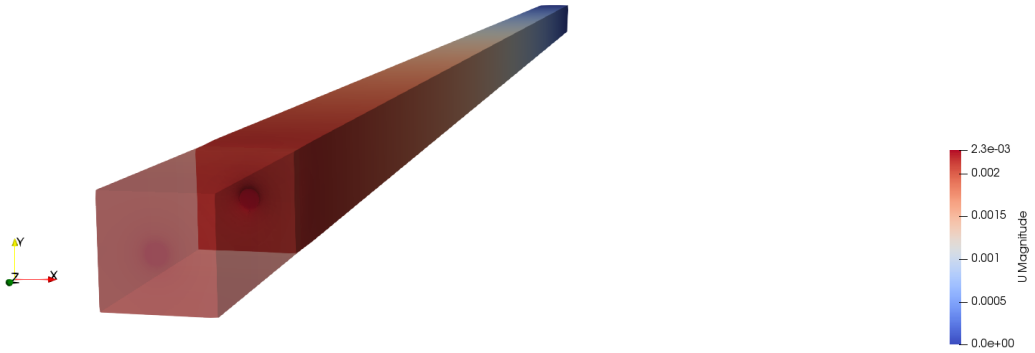

Figure 4.3 Circular Reinforcement Pattern after A PSC Prism with WA (a smoother tendon)

Figure 4.4 illustrates the analysis results for a prestressed crosstie containing tendons subjected to an initial prestress of 203 ksi immediately following de-tensioning. In this visualization, the highlighted regions identify specific elements where the maximum principal stress exceeds the defined tensile cracking threshold of 500 psi.

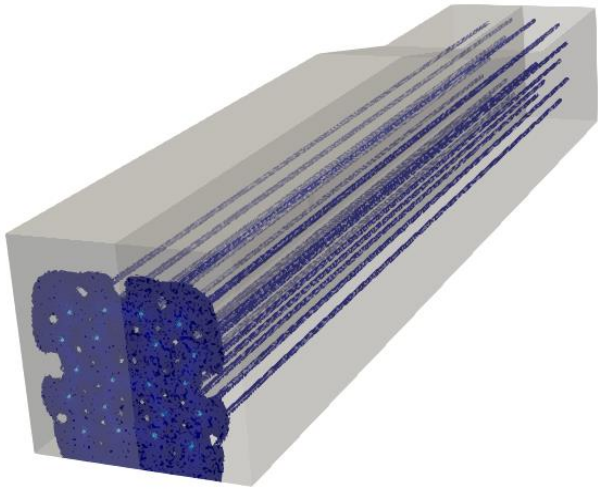

Figure 4.4 Elements less than or equal to 500 psi: PSC-WG

Chapter 5 : Numerical Analysis

5.1 Pull-out Aanalysis

A pull-out test on the elastic model of the four-inch concrete prisms was carried out. The initial stiffness of the concrete prism with each tendon can be measured. The stiffness coefficient, k, is defined as Force/Displacement.

This was the chosen metric due to the pull-out test shown in ABAQUS in Figure 3.14 as well as the schematic of the experimental analysis in Figure 5.1. In ABAQUS known maximum displacement of 0.02 inches was applied to the tendon and the reactionary force on the Z-boundary condition (described in section 3.3.1 Boundary Conditions the face of the coarse concrete section opposite the origin in the longitudinal direction) was measured. This was intended to mimic the experiment to be performed on a real concrete prism where a maximum force or displacement can be controlled.

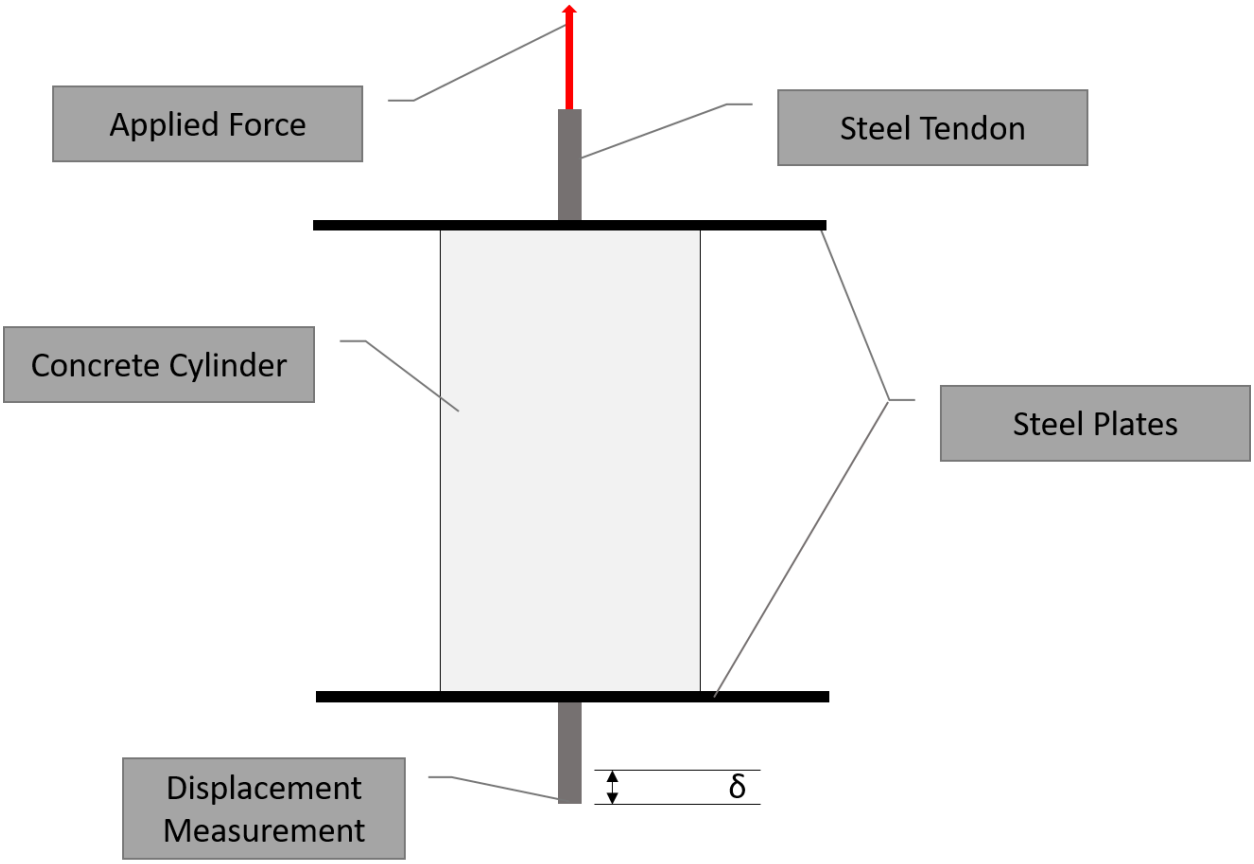

Figure 5.1 Pull-Out Test Schematic.

For the model, the displacement tests were standardized by the displacement (0.02 inches), length (L = 4 inches), and as closely as possible by mesh density. Mesh density, as opposed to number of elements, was deemed more easily normalized due to the varying number of elements and nodes inherent to wire models with different geometry.

The factors which influence stiffness that we seek to explore are the shape effect of the indentation pattern, depth of the indentation, average area of the cut (commonly referred in this report to as $^{V}/_{d}$ or Volume/depth of indentation), side angle, and the cover depth. The stiffness results per model are shown in Table 5.1 and Figure 5.2. Also shown in Table 5.1 are the parameters each model was created to explore.

Table 5.1 Models Sorted by Stiffness.

Shape	k	Parameter
Chevron (WG)	5045.88	Depth, Side Angle
OSquare (Top 60)	5368.645	Side Angle, V/d
OSquare (Top 90)	5390.21	Side Angle, V/d
CSquare (A1190)	5392.635	V/d
OSquare (All 90)	5416.6825	V/d
Chevron (Single Reverse)	5426.855	Shape
CSquare (Rotated 30)	5429.895	Shape, V/d
Circle	5922.09	Shape
Chevron	6540.24	Shape

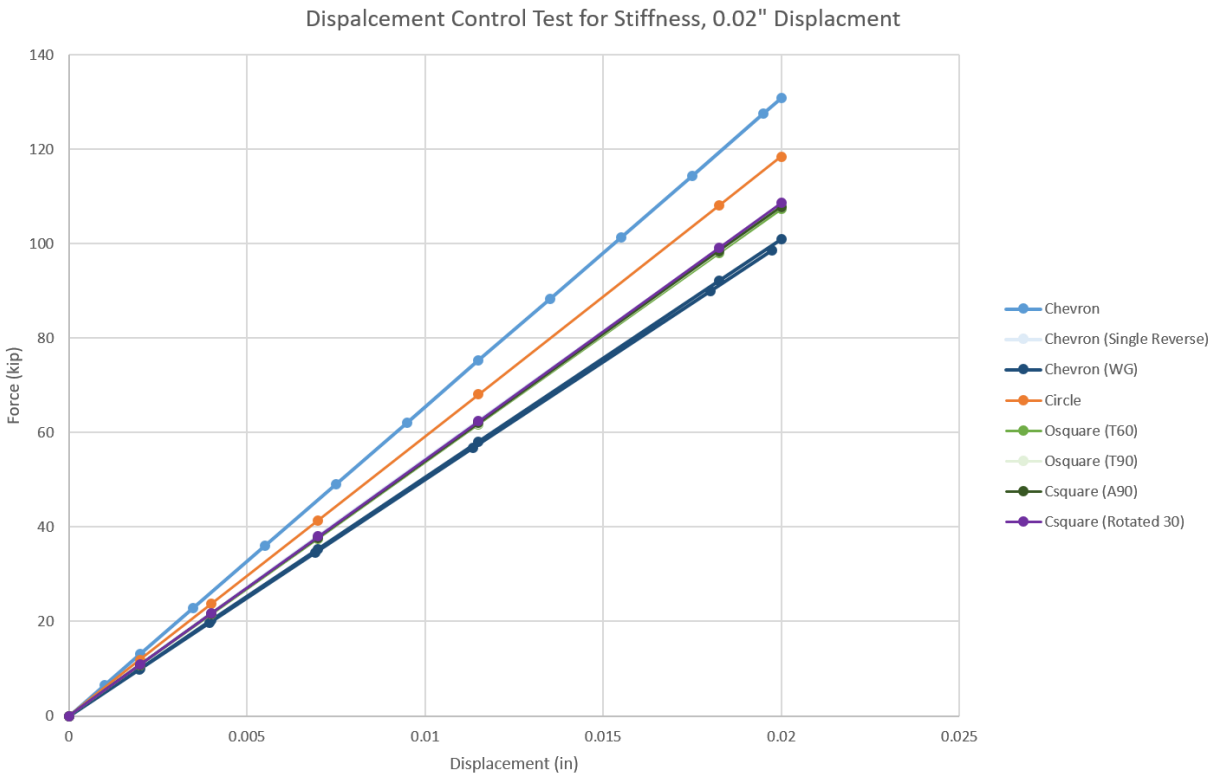

Figure 5.2 Force Displacement Results, All Models.

Based on the analysis of the four-inch pullout tests, the sidewall angle appears to be the primary factor influencing stiffness. This is evidenced by the distinct performance gap between geometries: models with sidewall angles less than 90° exhibited lower stiffness coefficients ($5,045.88 – 5,390.21 kip/in), whereas models with 90° sidewall angles demonstrated significantly higher values ($5,392.64 – 6,540.24 kip/in). This data indicates that indentations with angles approaching 90° provide superior mechanical interlocking properties compared to those with shallower angles. However, implementing perfectly perpendicular angles presents manufacturing challenges due to the limitations of the stamping process. In addition, sharp corners results in higher stress concentrations.

The average area dimension (V/d) showed little to no correlation with stiffness during the elastic bonding stage. This lack of correlation was verified by comparing models with identical average areas but different shapes. For example, the OSquare and Circle patterns share an average area but yielded vastly different stiffness responses 5,416.68 kip/in) vs. 5,922.09 kip/in. Similarly, the CSquare and Original Chevron patterns differed significantly 5,392.64 kip/in vs. 6,540.24 kip/in, despite having equivalent areas.

Finally, the depth of cut was considered as a potential influence, but its impact remains difficult to isolate. The shallowest model, Chevron WG, also featured a very shallow sidewall angle, making it difficult to decouple the effects of depth versus angle.

5.2 Prestress Analysis: De-tensioning

As we previously discussed on the Chapter 3 the prestress analysis upon de-tensioing is performed on the intermediate and full scale model. Following are the results of the various studies we performed on the models.

5.2.1 2”x2”x34.5” Prism (Intermediate model)

5.2.1.1 Description of the model

The 2”x2”x34.5” prism is a model we developed to bridge the transition from the small-scale models (1”x1”x4” prism) to the full-scale model (PSC crosstie). While developing this model and subsequently exploring the results and responses from the analysis, we developed a deep understanding of various processes.

A major technical challenge involved achieving a sufficiently fine mesh within the larger volumetric domain of the model. The analysis prioritized the steel-concrete interface, as this region yields the most critical data regarding bonding behavior. Initially, computational constraints limited this zone to a coarse element size of 0.00811 inches (Model M1, Table 5.2). However, by implementing the partitioning techniques shown in Figure 5.3, the team successfully executed a progressive mesh refinement strategy. The element size was iteratively reduced to 0.006 (M2), 0.004 (M3), and 0.002 (M4) (Figure 5.4). This process continued until the output stabilized—meaning the results between iterations showed negligible difference—thereby confirming that the analysis had achieved mesh convergence.

Table 5.2 Element and Nodes.

	CC	IC	FC	FS	CS
M1	0.4	0.02	0.00811	0.00811	0.03
M2	0.1	0.02	0.006	0.006	0.006
M3	0.1	0.02	0.004	0.004	0.02

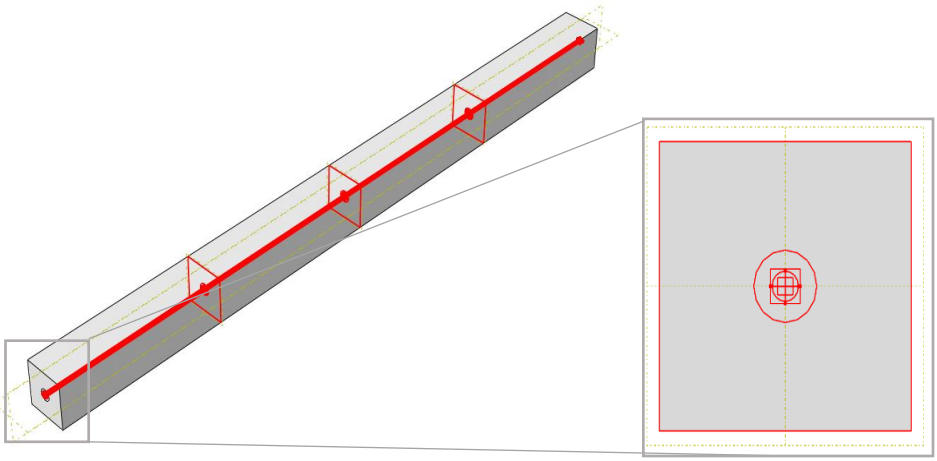

Figure 5.3 Model Partition.

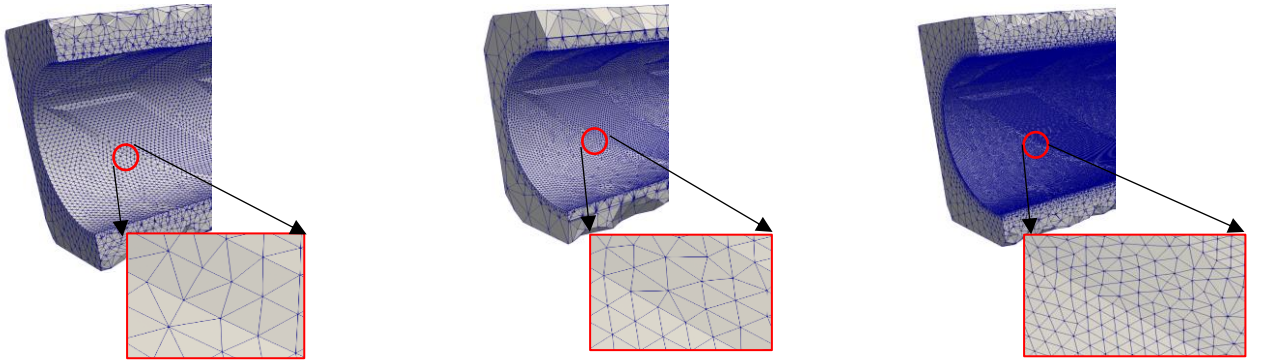

Element Size at interface: 0.006 Element Size at interface: 0.004 Element Size at interface: 0.002

Figure 5.4 PSC Prism – WG mesh refinement.

To validate the convergence of the numerical solutions, stress distributions were compared by extracting data along an identical path within the "Fine Concrete" zone across one model of three different mesh schemes (i.e. M1, M2, and M3). Figure 5.5 plots the Maximum and Minimum Principal Stress profiles for the PSC Prism-WA model under these varying schemes. A close examination of the data reveals a significant divergence in the curve produced by the coarsest mesh, M1 (0.0081 at interface). In contrast, the results obtained from the refined models—M2 (0.0061 at interface) and M3 (0.0041 at interface)—exhibit a strong correlation, indicating that the solution has stabilized at the finer mesh densities.

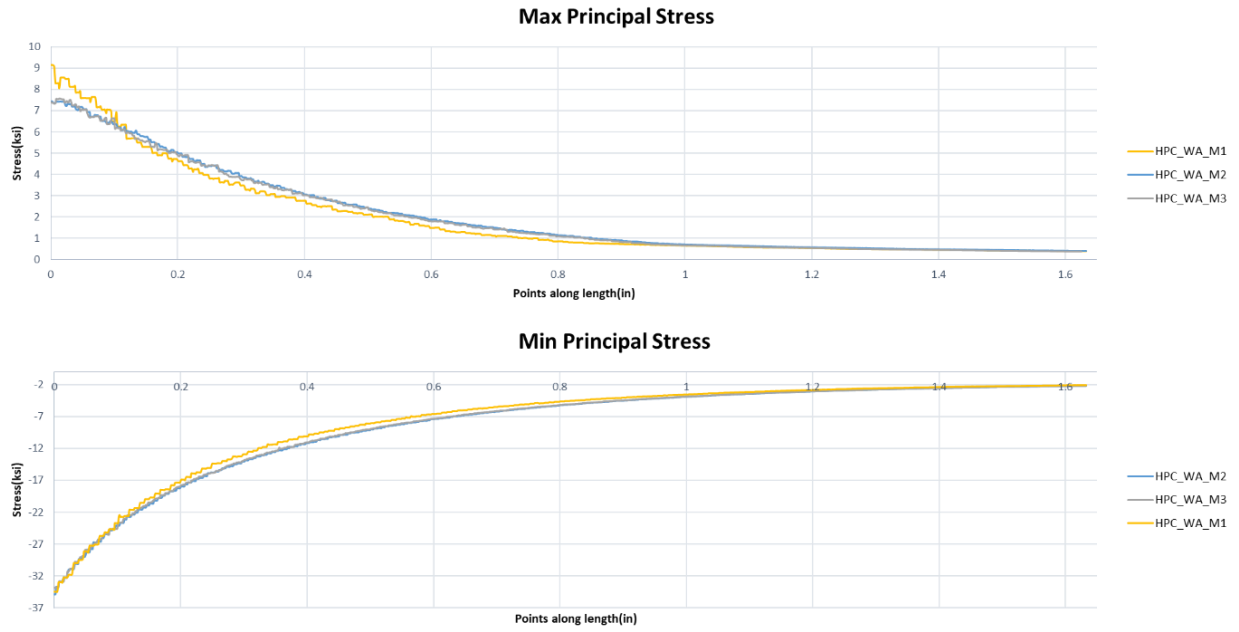

Figure 5.5 Sensitivity analysis: Mesh Size on PSC Prism-WA

5.2.1.2 Stress Distribution Along the Prestressing Tendons

To understand the stress variation (on the fine concrete) around the unconstrained end of the prism, we performed a line analysis along a length covering the first eight (8) indentations Figure 5.6. We performed this line analysis on each on the models (PSC Prism-WA; PSC Prism-WG and PSC Prism-WP).

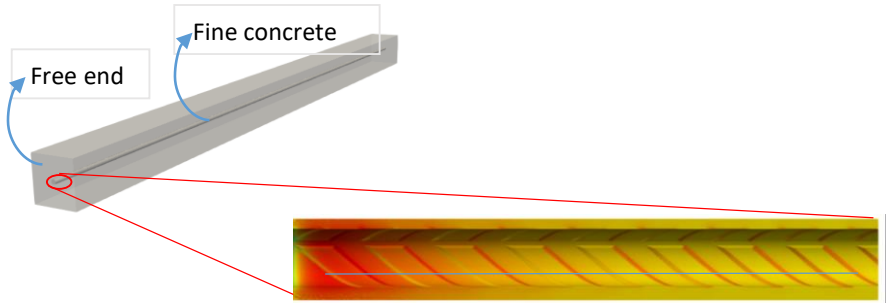

Figure 5.6 Line Analysis around free end.

PSC Prism-WA

This is the 2"x2"x34.5" prism embedded by the smooths tendon. Since there is no indentation on this tendon, we did not observe a fluctuation of the stresses at the surface of the fine concrete along the length. There is rather a constant (not linear) decrease of the intensity of the stresses as the points gets further from the free end Figure 5.7. Therefore, we conclude that the highest stresses (Tensile and Compressive) occur where the highest

displacement occurs, and the closer the points are to the constrained edge the less displacement they experience.

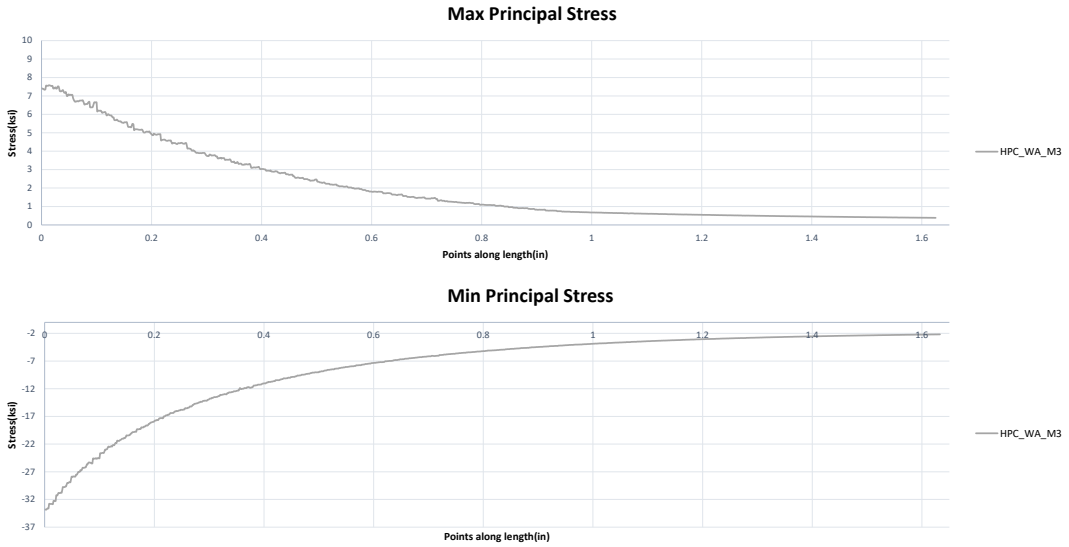

Figure 5.7 Max and Min Principal stress: PSC Prism-WA

PSC Prism-WG

Unlike the previous model, which was embedded by a smooth tendon, the PSC Prism-WG model is embedded by a chevron indentation (WG), which has indentations that are 0.0026 inch deep Figure 5.8.

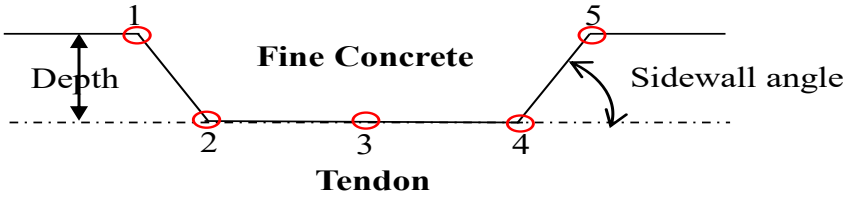

Figure 5.8 Indentation Profile

Upon plotting the stress distribution along the line of the fine concrete, a general trend of decreasing stress was observed as the distance from the free end increased. However, significant fluctuations were noted at specific intervals along this curve. To elucidate the mechanical influence of the wire indentations, it was determined that these fluctuations needed to be correlated with their precise geometric locations. Consequently, stress levels were monitored at five distinct reference points corresponding to specific features of the indentation profile (Figure 5.8). This targeted tracking allowed for the precise localization of critical zones on the concrete surface that are susceptible to stress concentrations.

As shown in Figure 5.9, the most significant tensile stress fluctuations occur at positions 1 and 5; the accompanying stress contour plots provide a visual correlation for these data points. In the region of the first three indentations, stress magnitudes at positions 1 and 2 are markedly lower than those at positions 4 and 5. However, from the fourth indentation onward, the stresses at

these respective locations begin to equilibrate. Additionally, an increasing stress gradient is observed along the sidewalls, specifically transitioning from positions 1 to 2 and from 3 to 4.

Conversely, the compressive stress analysis (minimum principal stress) reveals a consistent pattern across all indentations. Peak stress concentrations are identified immediately preceding (position 1) and succeeding (position 5) each indentation. Furthermore, the data indicates a distinct localized gradient characterized by a stress decrease between positions 1 and 2, followed by an increase between positions 4 and 5.

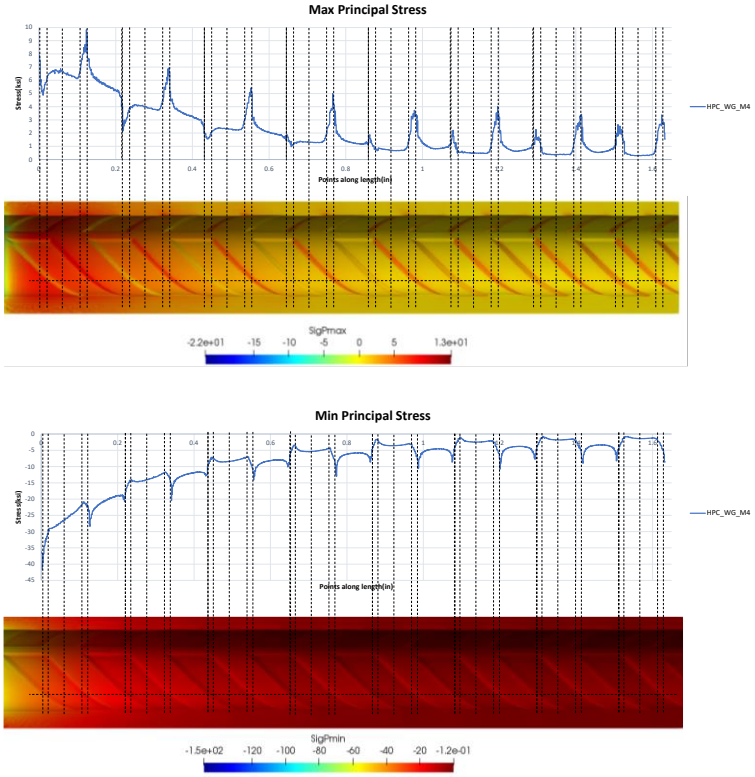

Figure 5.9 Max and Min Principal stress, PSC Prism-WG

PSC Prism-WP

The model, PSC Prism-WP is also a model embedded by an indented tendon with an indentation depth of 0.0046 inches**,** almost double of that of the WG model. The observed pattern as shown on Figure 5.10 is practically similar to that of PSC Prism-WG. They only differ in terms of magnitude. The stress surges from the PSC Prism-WP are more accentuated. Therefor we concluded that there might be a high probability for that accentuation to be caused by the depth of the indentation.

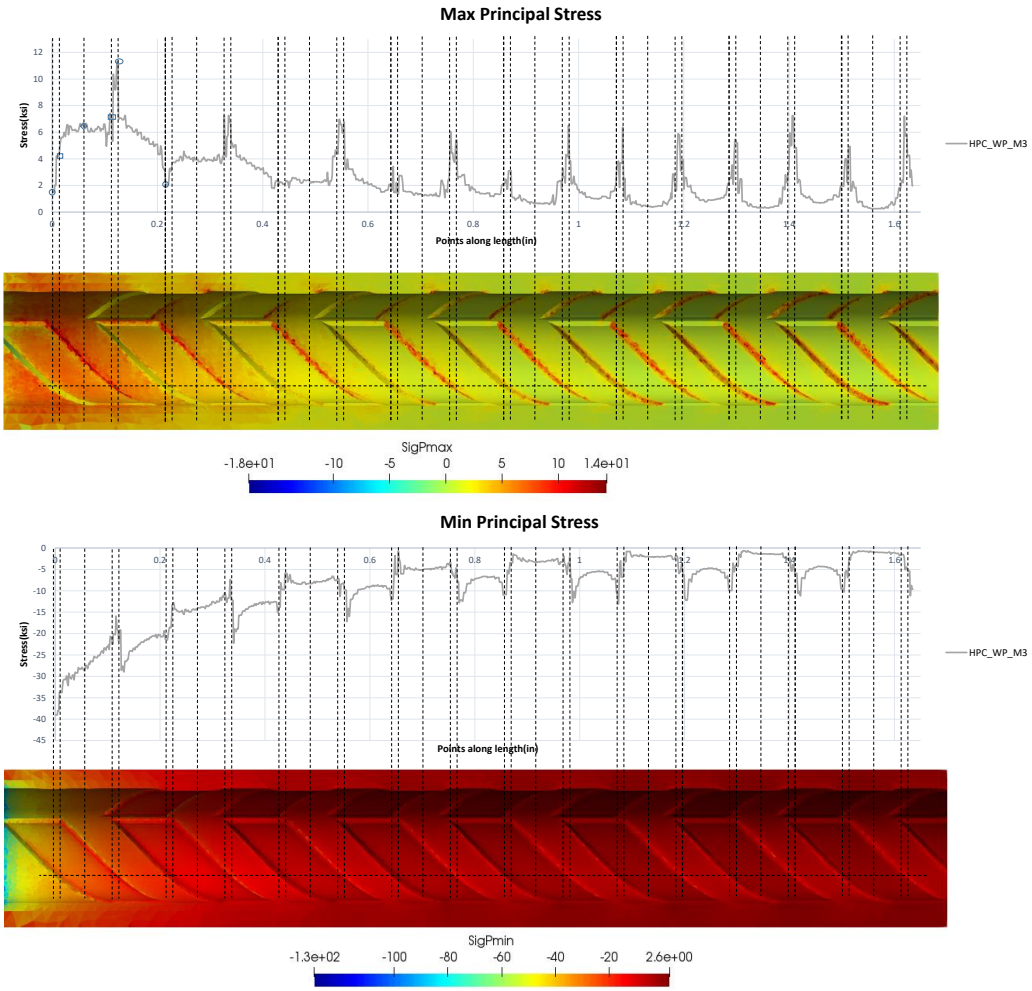

Figure 5.10 Max and Min Principal stress, Chevron_WP_Prism_M3.

Figure 5.11 is a comparison on which all three models are represented (Max and Min Principal Stress). From this comparison, we observe the difference in stress fluctuation, and gauge how much one curve is more accentuated compared to the other.

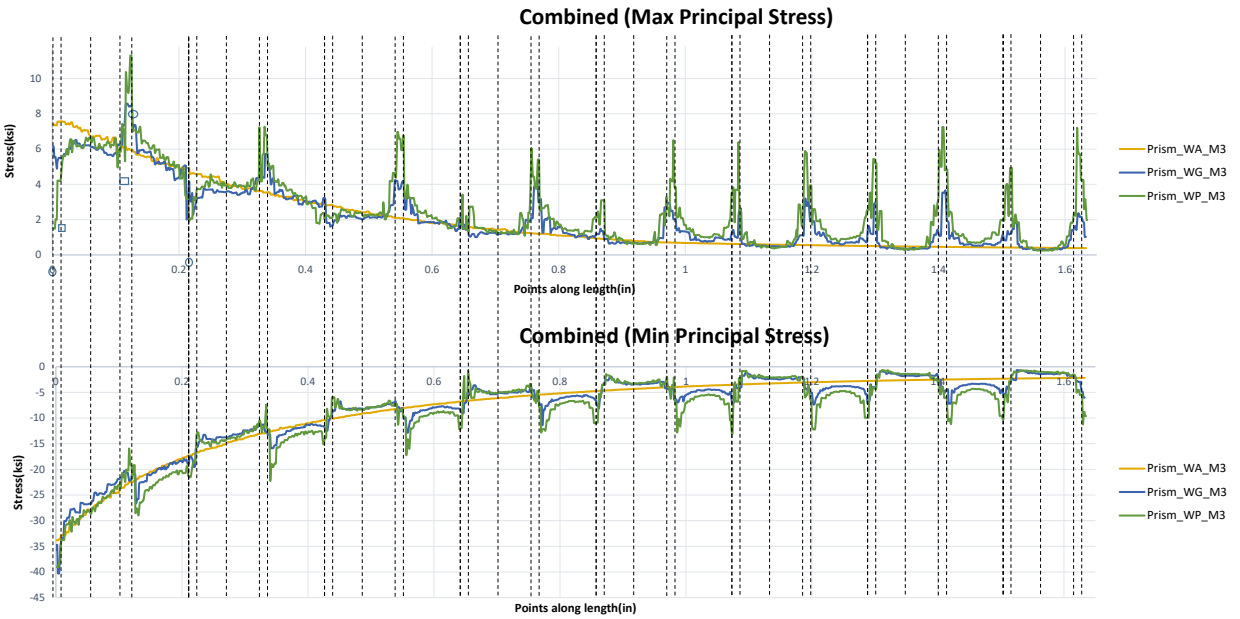

Figure 5.11 Comparisons of three prisms.

5.2.1.3 Radial Damage Study around the free end

The tensile strength of hardening concrete is directly dependent on its maturity. For the purposes of this study, the material properties at the time of de-tensioning were defined as 600 psi for tensile strength and 6,000 psi for compressive strength. By establishing these failure thresholds, the analysis was able to identify and visualize damaged elements within each model, allowing for the precise measurement of the damage radius extending from the steel-concrete interface. In this subsection, we explore the area expected to sustain critical damage upon de-tensioning.

PSC Prism-WA

For this model, because it is embedded by the non-indented tendon (Smooth tendon), the damage was concentrated around the free end (Figure 5.12.)

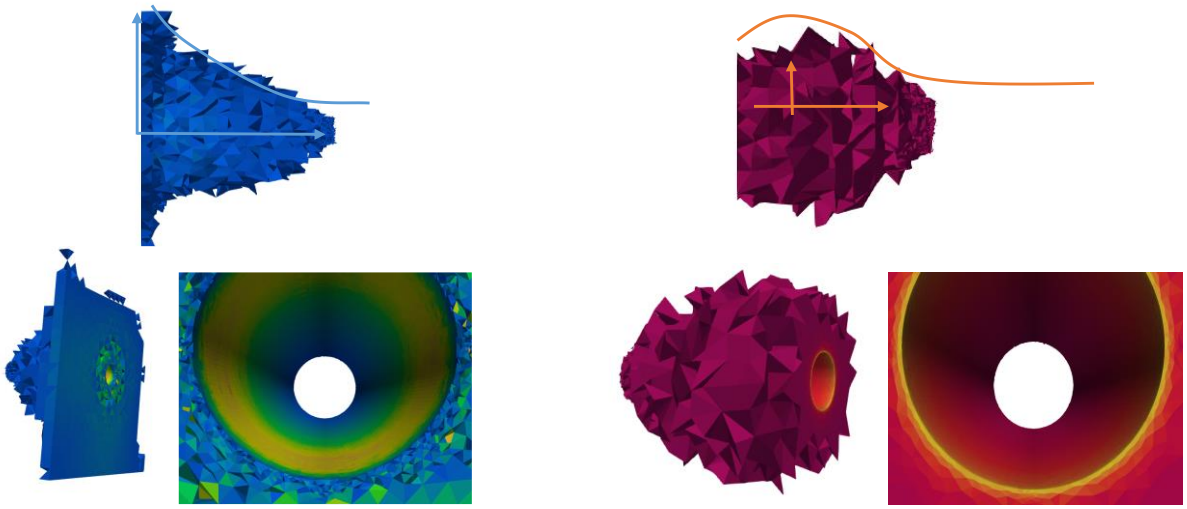

Tension Compression

Figure 5.12 Damaged portion of the PSC Prism-WA model due to tensile and compressive stresses.

From these images, we see that, more damage is caused by the tensile stresses. In addition, the free end face would be totally subjected to tensile stresses. The damage extends a length of about 1.2 in for both tension and compression Figure 5.13 in the Z direction.

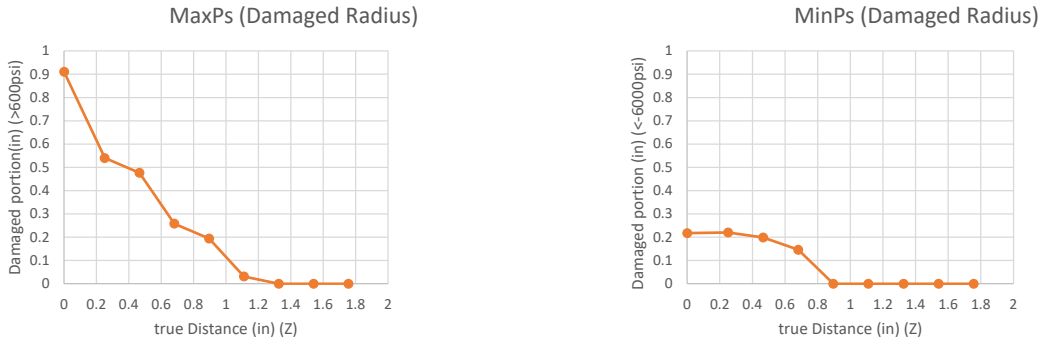

Figure 5.13 Damaged Radius of the PSC Prism-WA (Maximum Principal Stress and Minimum Principal Stress).

PSC Prism-WA

In this model, damaged elements were not confined solely to the free end region. As illustrated in Figure 5.14, damage at the steel-concrete interface propagated along the entire length of the model. This extensive damage distribution is attributed to the stress concentrations induced by the wire indentations.

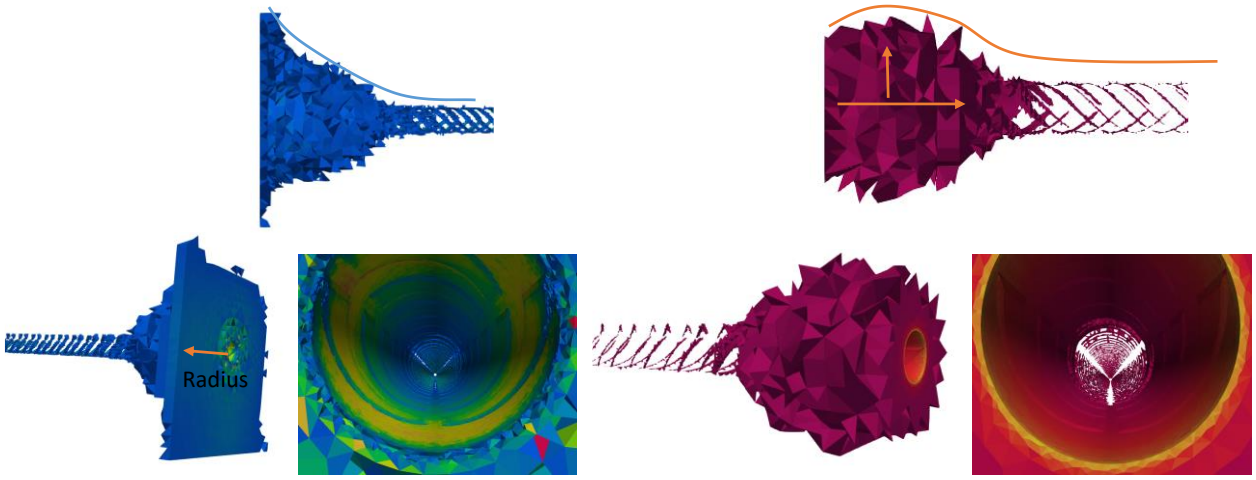

Figure 5.14 Damaged portion of the PSC Prism-WG model due to tensile and compressive stresses.

Consistent with previous observations, a distinct disparity in material damage is evident, with the damage induced by tensile stresses being significantly more extensive than that caused by compressive stresses. Figure 5.15 illustrates the substantial volume of damage concentrated around the free end, which propagates approximately 1.3 inches along the Z-axis.

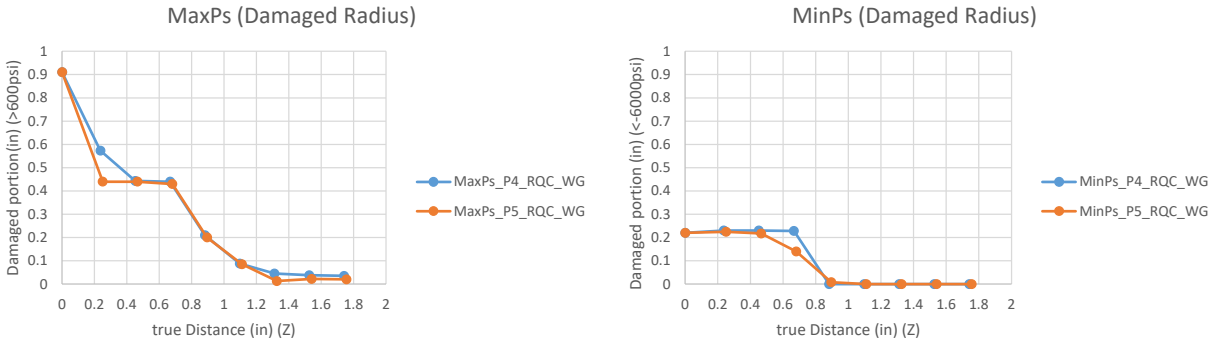

Figure 5.15 Damaged Radius of the PSC Prism-WG (Maximum Principal Stress and Minimum Principal Stress).

PSC Prism-WP

Given that the indentation depth of the WP tendon is double that of the WG, a corresponding increase in material damage—both at the indentations and the free end—is anticipated (Figure 5.16). This hypothesis is substantiated by the damage radius profile of the PSC Prism-WP shown in Figure 5.17. The analysis reveals a significantly larger damage radius, with the zone of extensive material degradation propagating approximately 1.5 inches along the Z-axis, surpassing the damage lengths observed in previous models.

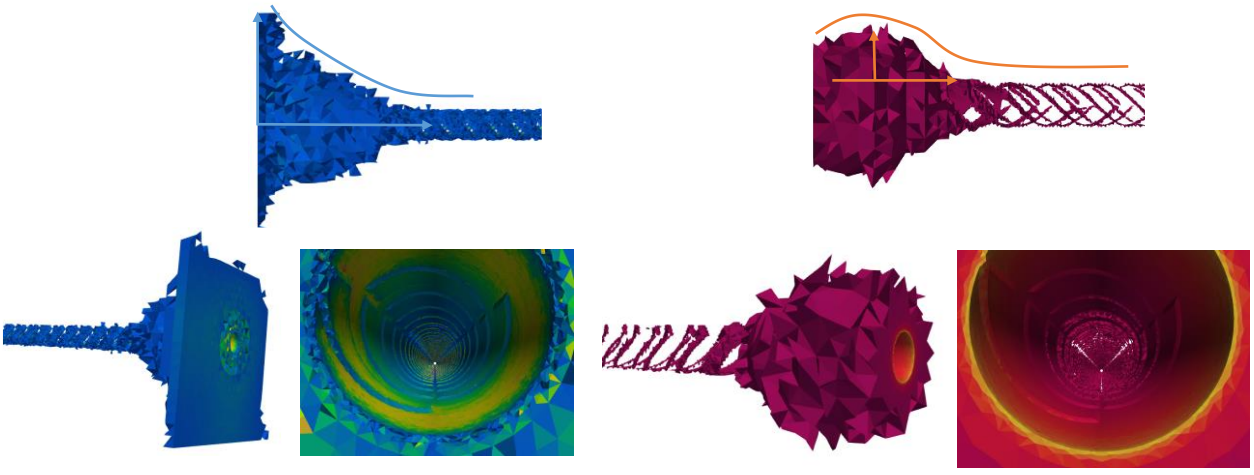

Tension Compression

Figure 5.16 Damaged portion of the Smooth_WP_Prism model due to tensile and compressive stresses.

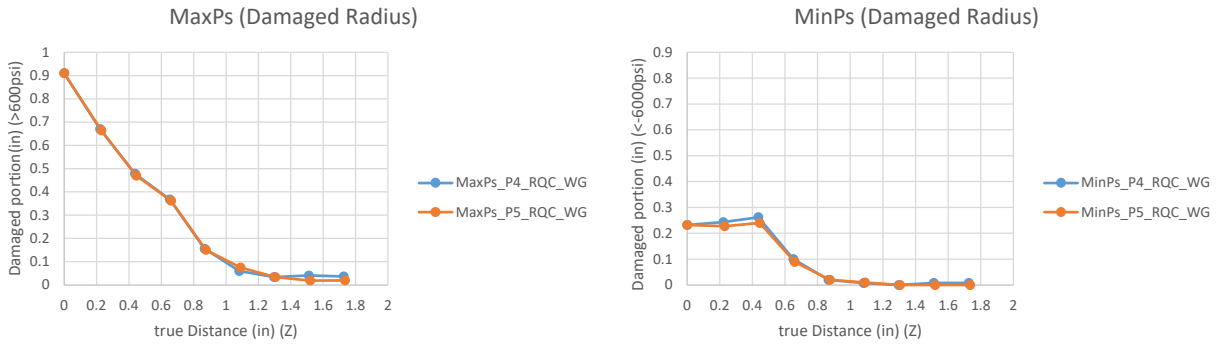

Figure 5.17 Damaged Radius of the PSC Prism-WG (Maximum Principal Stress and Minimum Principal Stress).

A brief conclusion from this study would be first to acknowledge that tensile stresses cause more damage to the prestress concrete of the prism. Secondly, the deeper the indentation the more damaged material there would be around the interface and at the free end.

5.2.1.4 Damaged volume study with respect to various stress intervals

In this subsection, the resulting volume of damaged material was computed and compared. The comprehensive data obtained from this analysis are presented in Figure 5.18. As illustrated in Figure 5.18, the fundamental damage patterns remain consistent regardless of the specific tensile or compressive strength intervals applied, despite minor fluctuations in magnitude. Regarding tensile stress-induced damage, the prism embedded with the smooth tendon (WA) exhibits the least damaged material, followed by tWG and then WP models. This hierarchy is directly attributed to indentation size, with deeper indentations correlating to increased damage.

Conversely, under compressive stress, the WG model demonstrates the lowest damaged volume However, as the interval narrows and concrete compressive strength increases, the damaged volumes across all three models tend to converge, showing comparable levels of degradation.

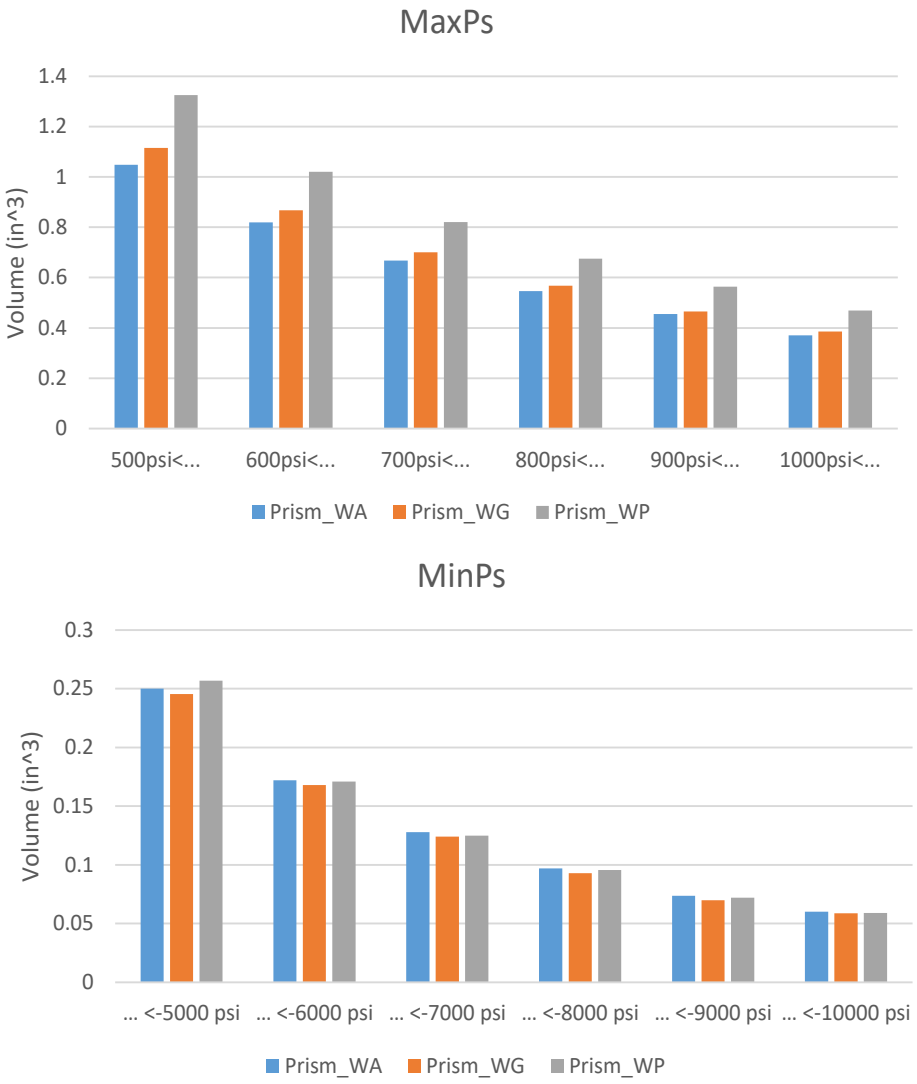

Figure 5.18 Damaged volume study.

5.2.2 Prestressed Concrete Crosstie - PSCC (Full Scale Model)

5.2.2.1 Description of the PSCC model

To investigate the mechanisms of crack initiation at the steel-concrete interface, a Finite Element Analysis (FEA) was conducted on a full-scale prestressed concrete crosstie (PSCC). To optimize computational efficiency, the model leveraged the crosstie's inherent cross-sectional and longitudinal symmetries (Figure 5.19b). Consequently, only one-quarter of the physical geometry was simulated (Figure 5.19c). This geometric reduction not only significantly lowered computational costs but also allowed for higher mesh resolution in critical regions, specifically permitting the assignment of smaller element sizes at the steel-concrete interface. All models

were developed using the commercial software ABAQUS, based on geometric specifications provided by one of the prestressed concrete crosstie manufacturers.

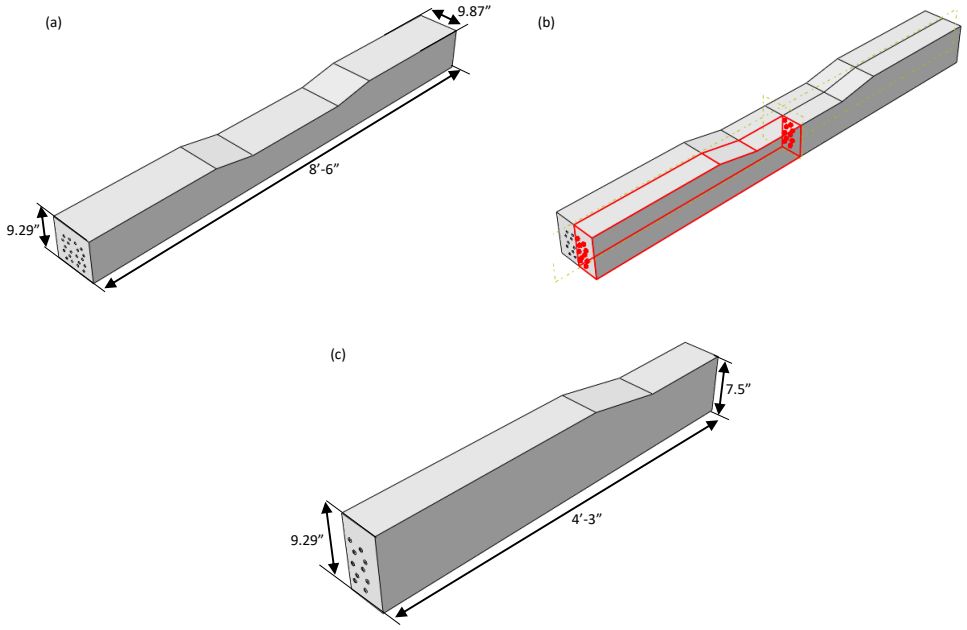

Figure 5.19 (a) Full crosstie model, (b) Divided Full model (with PSCC highlighted), (c) Quarter PSCC model

The PSCC models were in most part modeled in Abaqus. The tendons imported from SolidWorks are assembled with the Quarter Crosstie, followed by the assignment of Material properties to the concrete and steel (Figure 5.20(a)), then, assignment of boundary conditions and prestress force to the tendons. Another important task that is very essential to FEA that was undertaken in Abaqus is the meshing of the models. With emphasis put around the steel/concrete interface, location at which we consecrated a lot of time studying the stress field. The meshing schemes were assigned such that the finer seeding is used around the interface. Figure 5.21 shows one example of the quarter PSCC model with detailed mesh.

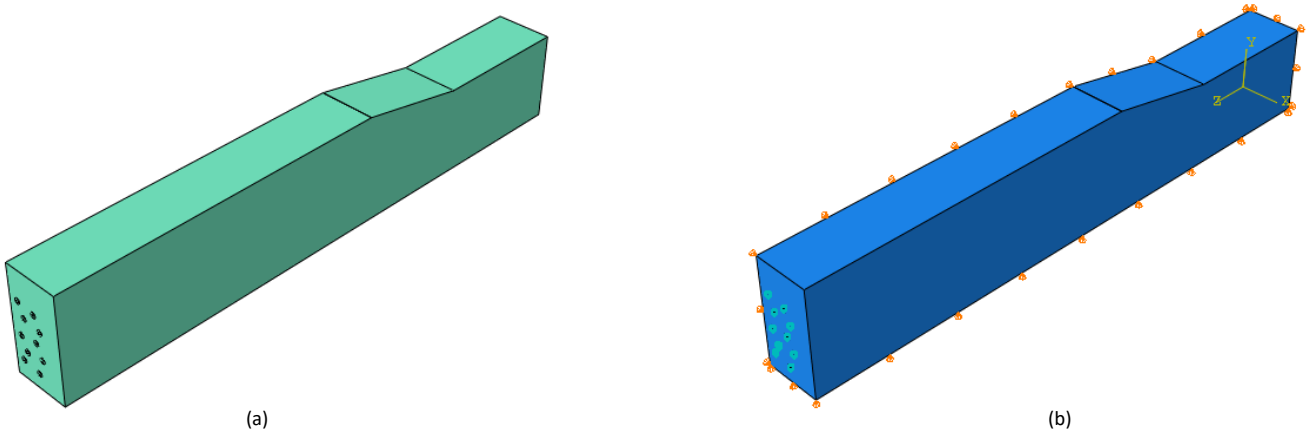

Figure 5.20 (a) Material property assigned, (b) boundary conditions applied and prestress applied to the tendons

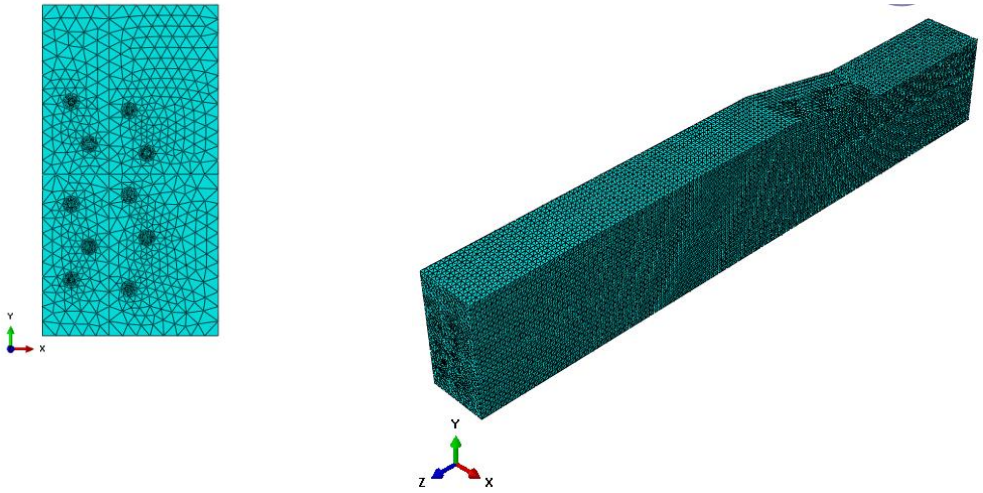

Figure 5.21 Meshing.

All the parameters (material properties, boundary conditions, Prestressing level, Meshing scheme) used during the modeling of the PSC models (PSCC-WA, PSCC-WG and PSCC-WP) were kept identical, so that the analysis could be performed on common basis. After the modeling, instead of submitting the analysis on the commercial software Abaqus we judged necessary to only write the .inp file and afterward use the High Performance Computer (HPC) available at TACC [46] to run the analysis . As with prior experience we knew the commercial Software to be very expensive in terms of computational cost, we developed an in-house code that will enable us to run effectively the simulation on the HPC. While exploring the results during the post-processing phase, we undertook various studies to develop a better understanding of the behavior and damage mechanism of the prestress prism when embedded by tendons characteristically different.

5.2.2.1 Effect of having the reinforcement tendons rotated

In this subsection, the prestressing tendons were rotated 120 degrees from their conventional orientation to evaluate potential variations in deformation behavior. The analysis revealed that, regardless of the rotational alignment, the deformation patterns remained consistent. Figure 5.22 depicts the 3D configuration of the prestressing wires following this 120^{o} rotation.

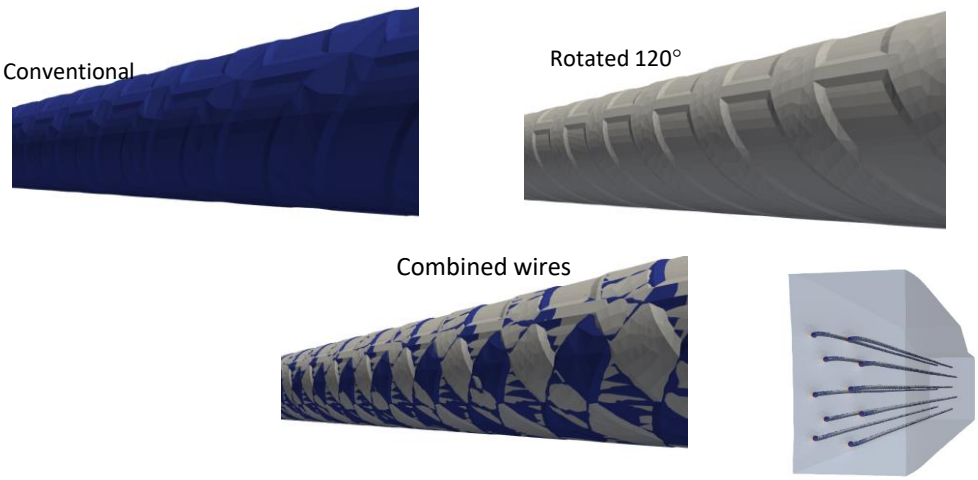

Figure 5.22 Effect due to rotating the tendons.

5.2.2.3 Effect of rearranging the position of the wires

In this subsection, the prestressing tendons were reconfigured to evaluate the impact of geometric distribution. Unlike the conventional staggered arrangement, the new configuration aligns the tendons into parallel vertical columns within the PSC cross-section. Analysis indicates that this alternative arrangement (Setup 2) results in a marginal increase in displacement magnitudes, while the overall deformation patterns remain largely consistent with the baseline. Figure 5.23 illustrates the two distinct prestressing wire configurations, while Figure 5.24 provides a comparative analysis of the displacement profiles for three prestressing wires following de-tensioning.

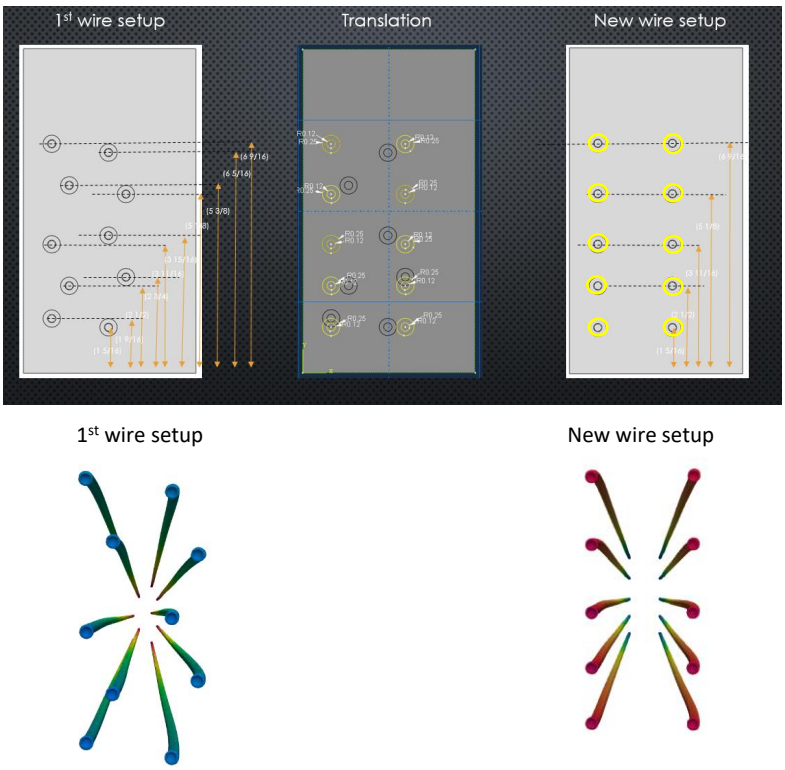

Figure 5.23 1st and 2nd Tendon Arrangement.

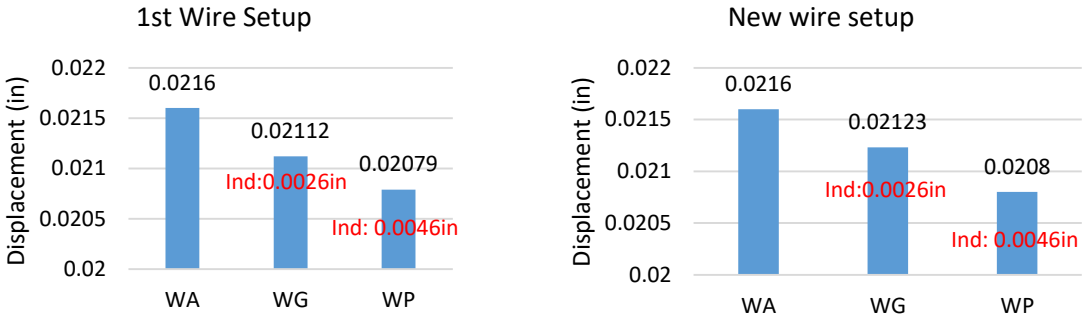

Figure 5.24 Displacement Comparisons.

5.2.2.4 Effect of indentation size, shape and sidewall angle

This study was conducted to quantify the influence of tendon indentation geometry—specifically size and shape—on mechanical interlocking mechanisms. Three distinct PSCC models were developed, each reinforced with a specific tendon configuration: the WA tendon (smooth/non-

indented), the WG tendon (shallow indentations), and the WP tendon (deep indentations). Prestress simulations were executed on the high-performance computing cluster.

The resulting deformed meshes were superimposed to isolate the locations of maximum displacement across all three models. As illustrated in Figures 5.25 and 5.26, the analysis revealed an inverse relationship between indentation depth and longitudinal contraction. The PSCC-WA model (visualized in blue) exhibited the highest magnitude of contraction following prestress release. In contrast, the PSCC-WG (white) and PSCC-WP (red) models demonstrated progressively reduced displacements. Specifically, due to the enhanced mechanical interlocking provided by the indentation depth and sidewall angle, the PSCC-WG and PSCC-WP models experienced 2% and 4% less displacement, respectively, compared to the smooth PSCC-WA baseline (Figure 5.27). This suggests that the radial dilation of the WA prestressing wires is likely to be the most pronounced. Furthermore, the WG wires are expected to exhibit greater dilation than the WP wires, despite the fact that the shallower indentation depth of the WG profile induces lower stress concentrations. These findings empirically demonstrate the significant contribution of indentation geometry to the system's interlocking capacity.

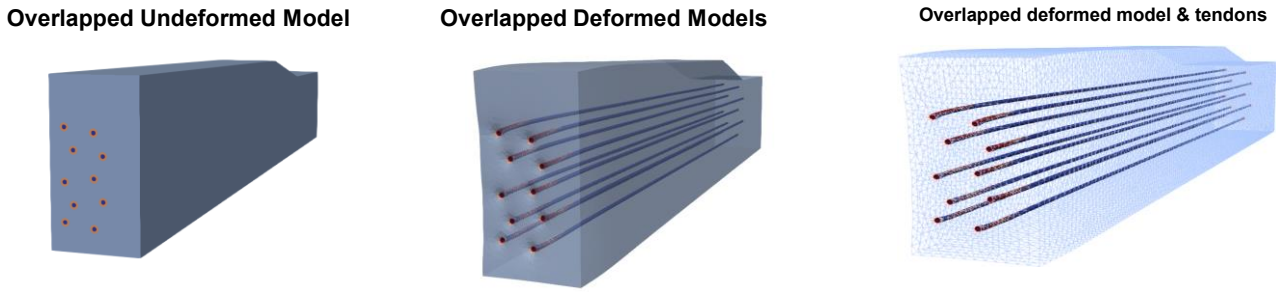

Figure 5.25 Overlapped PSCC models.

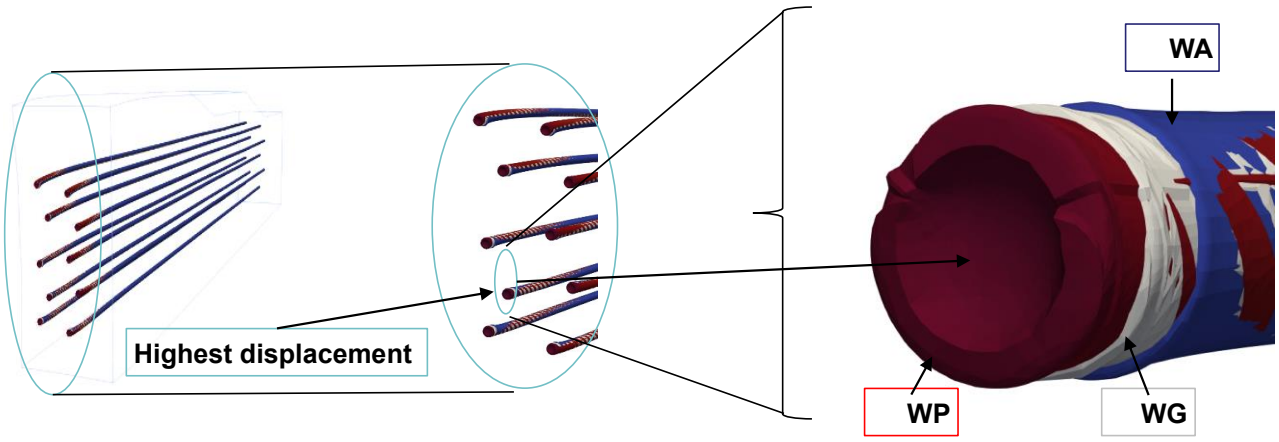

Figure 5.26 Interlocking effect Explained, Overlapped tendons.

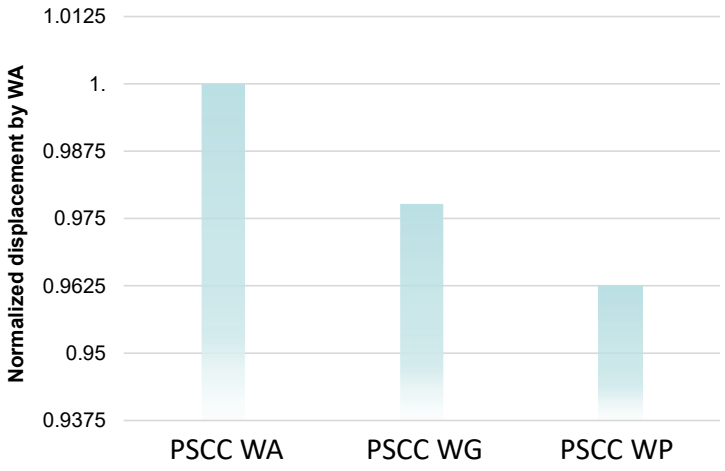

Figure 5.27 Normalized Displacement Comparisons of PSCC models.

5.2.2.5 Comparison of stress distribution

To characterize the stress distribution at the steel-concrete interface, a line stress analysis was performed along a path bisecting the center of the concrete indentations surrounding Tendon #8 (Figure 5.28). Starting from the embossed indentation closest to the free end of the indentation #8, we plotted the tensile and compressive stresses along the line (Figure 5.29).

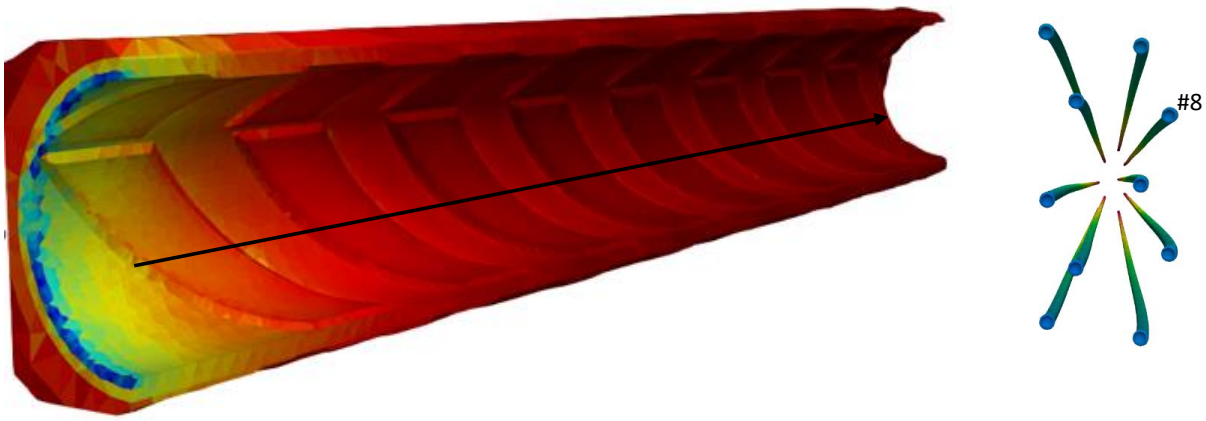

Figure 5.28 Line Stress Analysis.

Figure 5.29 presents a comparison graph illustrating the tensile and compressive stress profiles for the PSCC-WA, WG, and WP models. To facilitate comparison, all curves were normalized with respect to the absolute compressive principal stress observed in the PSCC-WP model. This normalization immediately highlights that the PSCC model reinforced with the WP tendon exhibits the highest stress magnitudes at the steel-concrete interface. Throughout the analyzed length (indentations 1 through 8), the PSCC-WP profile consistently displays the most pronounced peak stresses in both tension and compression. These concentrations are attributed to the synergistic geometry of the steep sidewall angle and the significant indentation depth.

A distinct phase shift is observed in the stress behavior of the WA tendon (represented by gray and yellow curves for maximum principal stress (MaxPs) and minimum principal stress (MinPs), respectively) compared to the indented models. While the WP tendon records peak stresses directly at the indentation locations, the WA tendon exhibits its relative maxima in the regions between indentations; this alternating pattern holds true for both tensile and compressive stress states. Regarding spatial distribution, the tensile stress spikes predominantly occur at the distal edge of the embossed indentation—specifically, the sidewall furthest from the free end.

To further investigate the precise localization of these stress concentrations, a detailed analysis focused on Indentation #4 (Figure 5.30) was conducted, isolating the PSC_WP curves (MaxPs_WP and MinPs_WP). In Figure 5.30, the red marker on the left identifies a critical zone approximately 0.006–0.009 inches from the leading edge of the indentation, coinciding with a distinct compressive stress concentration. A symmetrical peak is observed at an equivalent distance from the trailing edge. Regarding tensile stresses, a minor concentration is detected immediately preceding the proximal sidewall, while a more pronounced magnitude occurs at the distal end.

This analysis provides essential insight into the stress distribution mechanisms, facilitating a comparative performance evaluation of the three tendon profiles (WA, WG, and WP). Based on these findings, the WG tendon is identified as the optimal configuration. It achieves a critical balance: the shallow indentations provide sufficient mechanical interlocking, yet the profile exhibits significantly mitigated stress concentrations in critical zones compared to the deeper WP design.

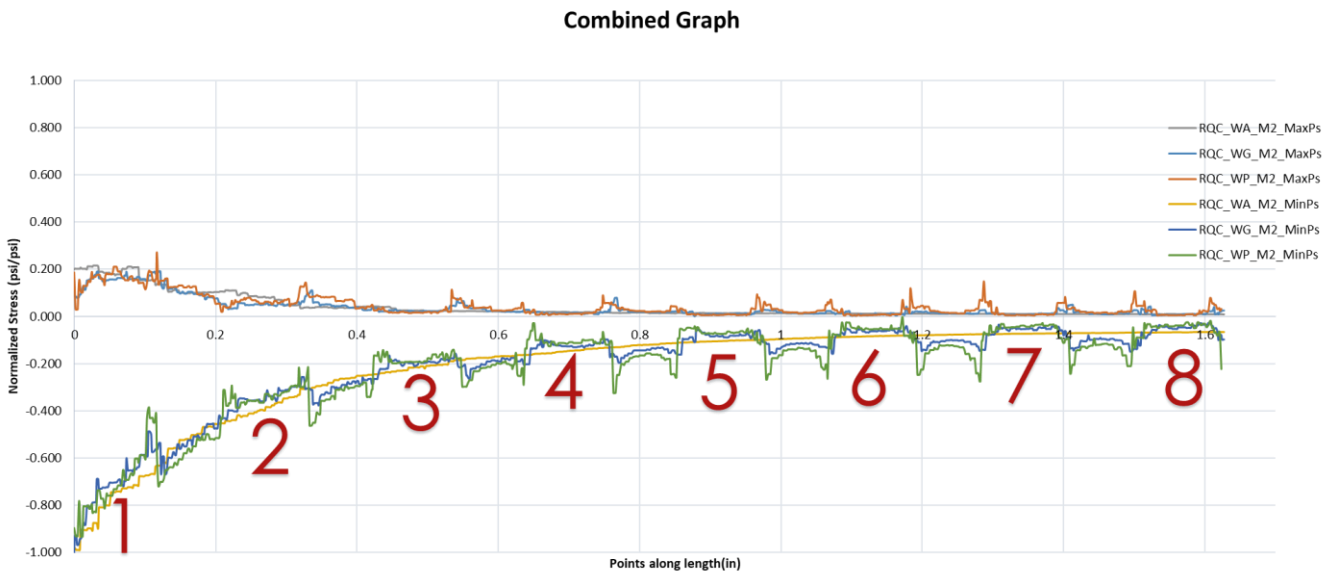

Figure 5.29 Line Stress Analysis on Indentations # 1-8 from PSCC models.

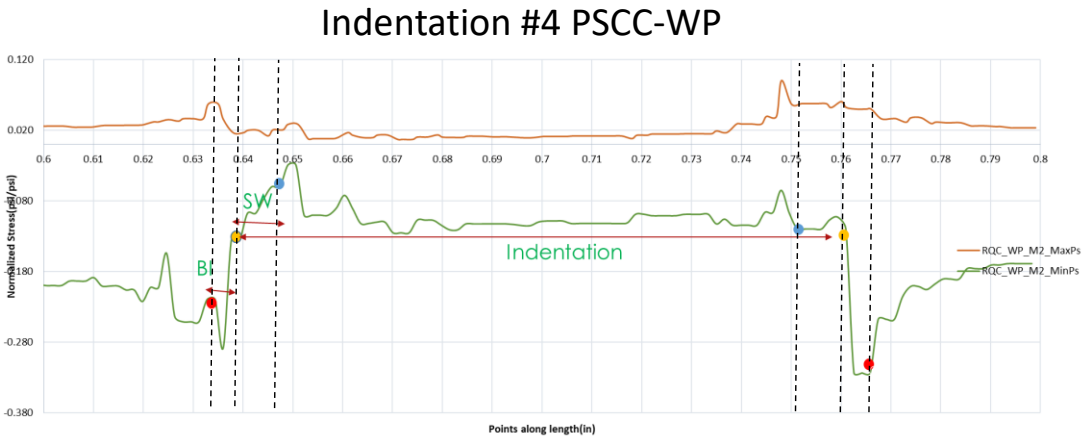

Figure 5.30 Stress curves (MaxPs &MinPs) from the indentation #4

5.2.2.6 Damaged material

This subsection quantified the extent of damaged material (volume) by parametrically varying the tensile and compressive stress thresholds since de-tensioning strength can vary. The study elucidated two fundamental aspects: (1) the optimal concrete mechanical properties required for crosstie fabrication, and (2) the comparative magnitude of damage induced by distinct tendon geometries.

Figure 5.31 presents the damage volume data categorized by stress type and strength threshold interval. In the compressive stress analysis, the PSCS-WG model exhibits the lowest damage volume when the prestress is released at a compressive strength of 5,000 psi. However, as the compressive strength increases, the damage volumes across all three models converge to comparable levels.

Conversely, under different level of tensile cracking strength, the relative performance hierarchy remains consistent regardless of the threshold interval: the PSCC-WP model sustains the highest volume of damage, followed by the PSCC-WG, and finally the PSCC-WA. Notably, an inverse relationship is observed where the total damage volume diminishes as the defined tensile strength increases from 500 psi to 1,000 psi. Figures 5.32 through 5.37 provide visual representations of the tensile stress-induced damaged regions from multiple viewing angles, plotted according to their respective stress intervals of PSCC-WA, WG, and WP models.

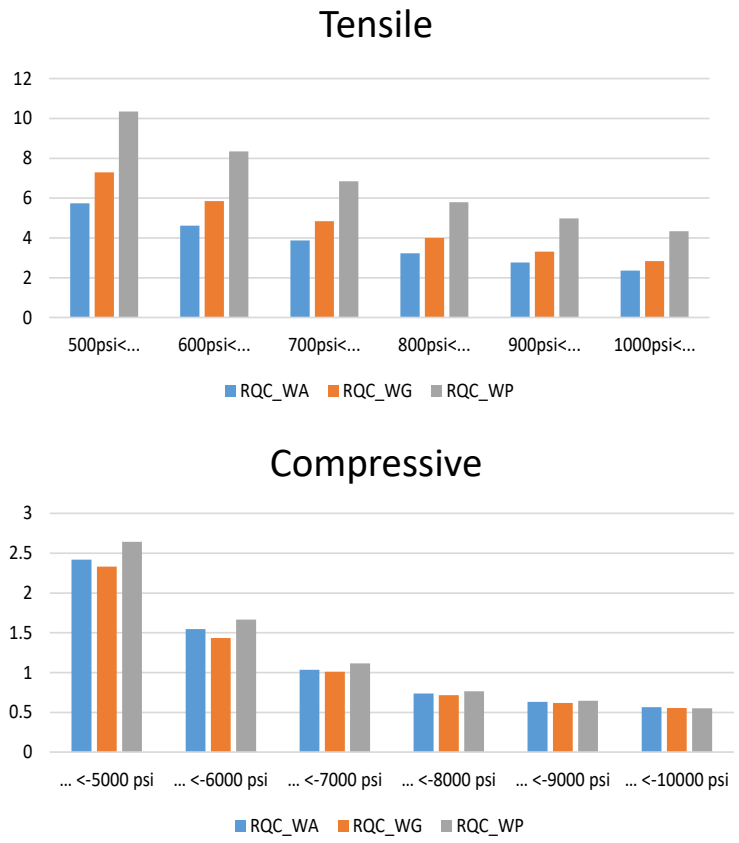

Figure 5.31 Volume of damaged material with respect to stress interval

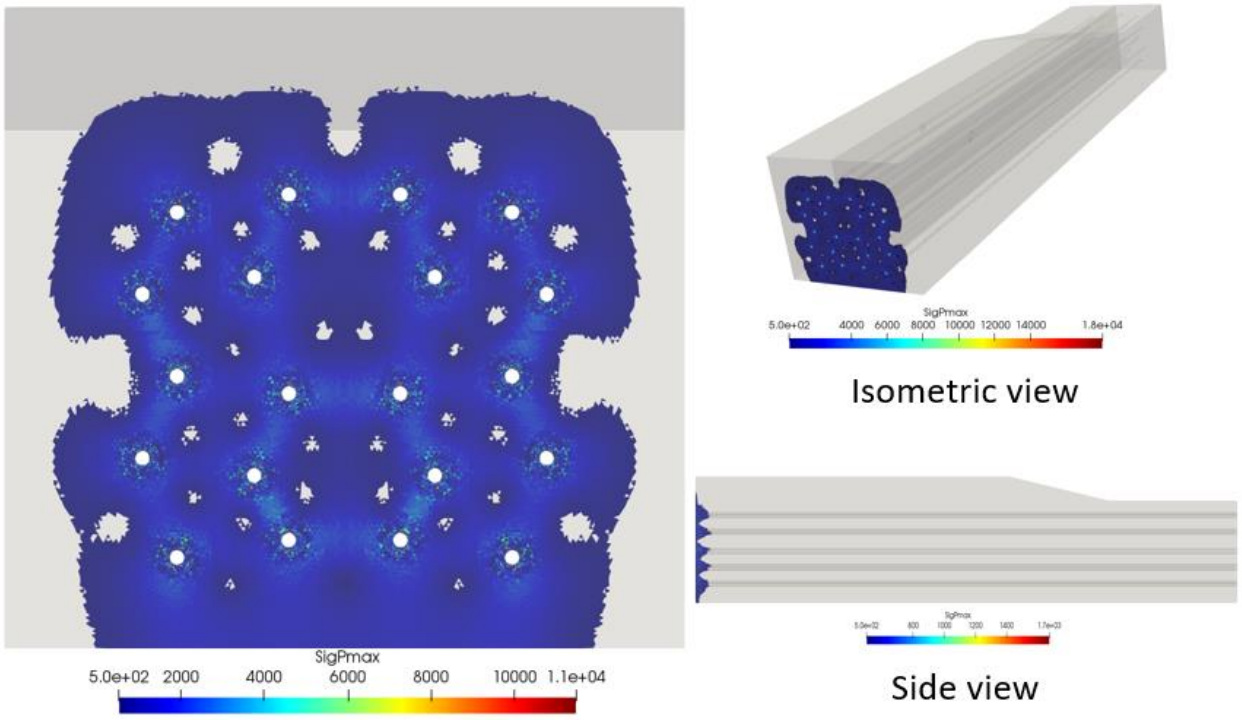

Figure 5.32 PSCC-WA: Tensile strength of 500 psi

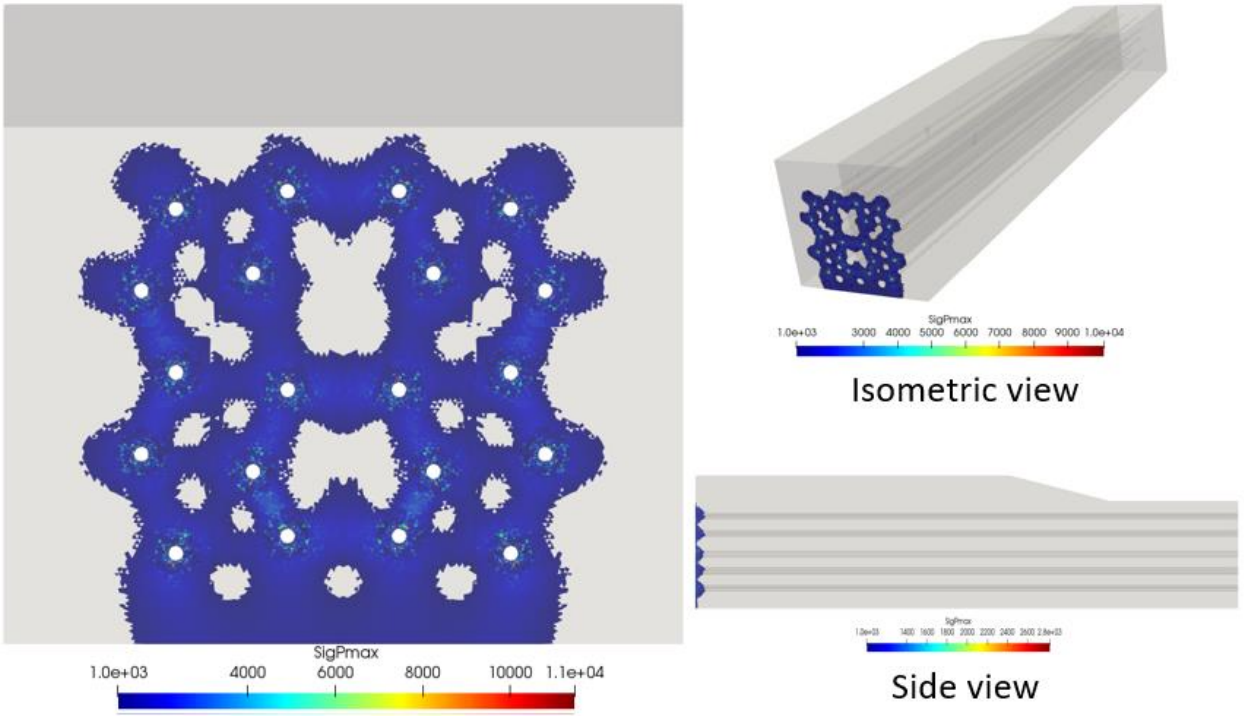

Figure 5.33 PSCC-WA: Tensile strength of 1000 psi

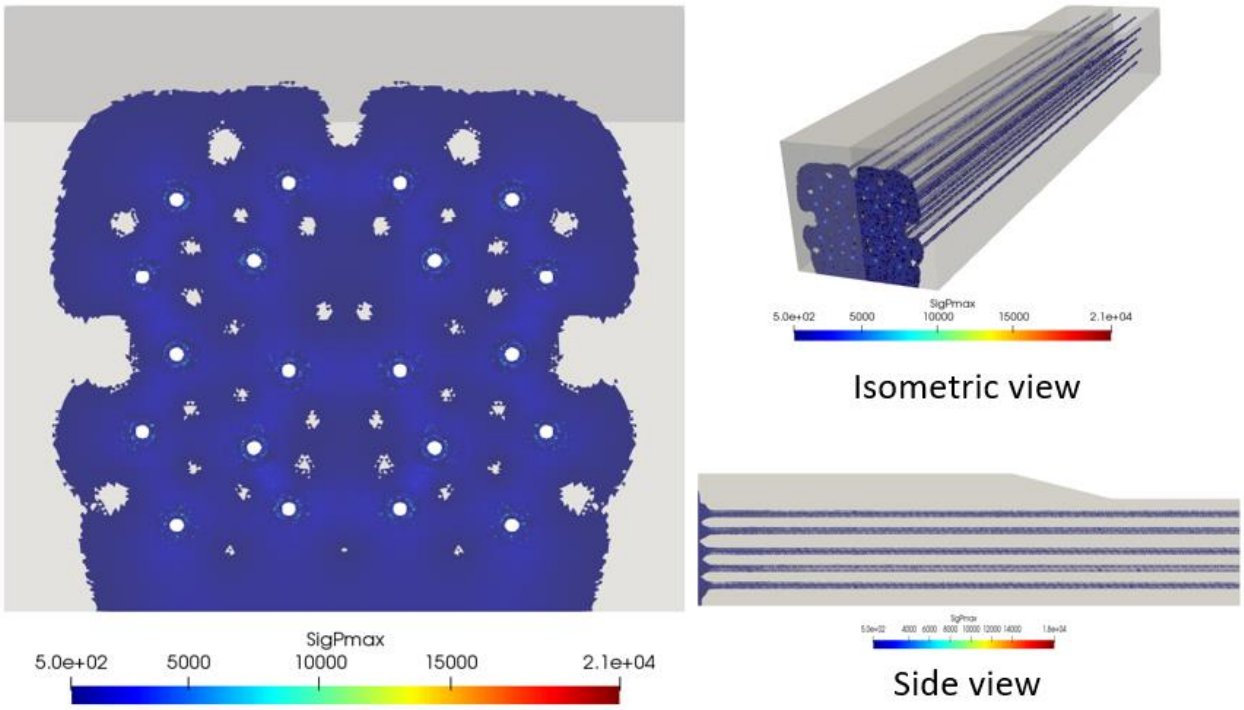

Figure 5.34 PSCC-WG: Tensile strength of 500 psi

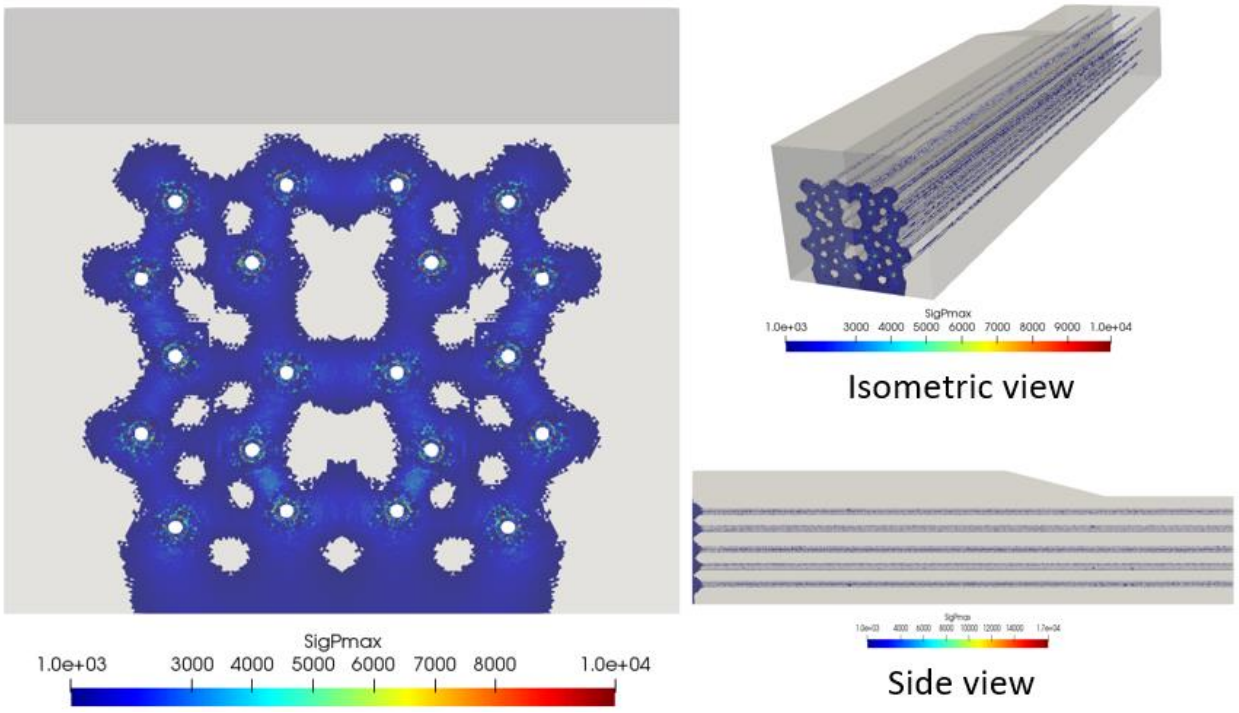

Figure 5.35 PSCC-WG: Tensile strength of 1000 psi

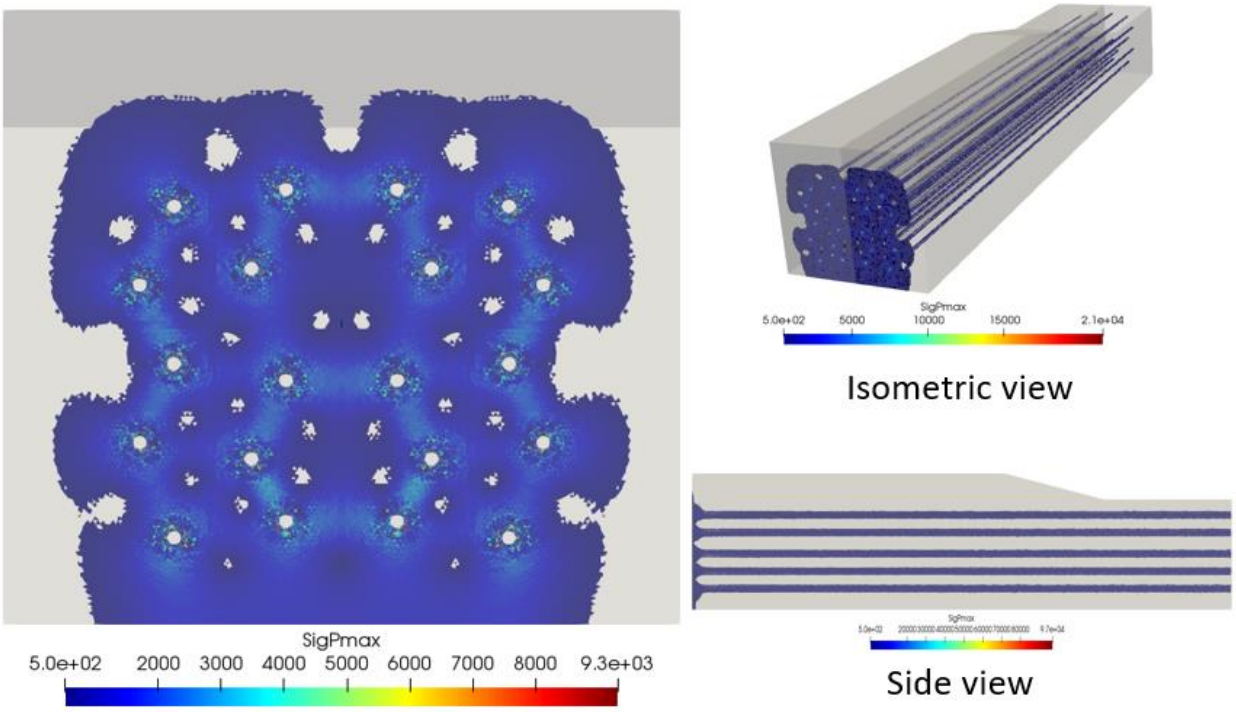

Figure 5.36 PSCC-WP: Tensile strength of 500 psi

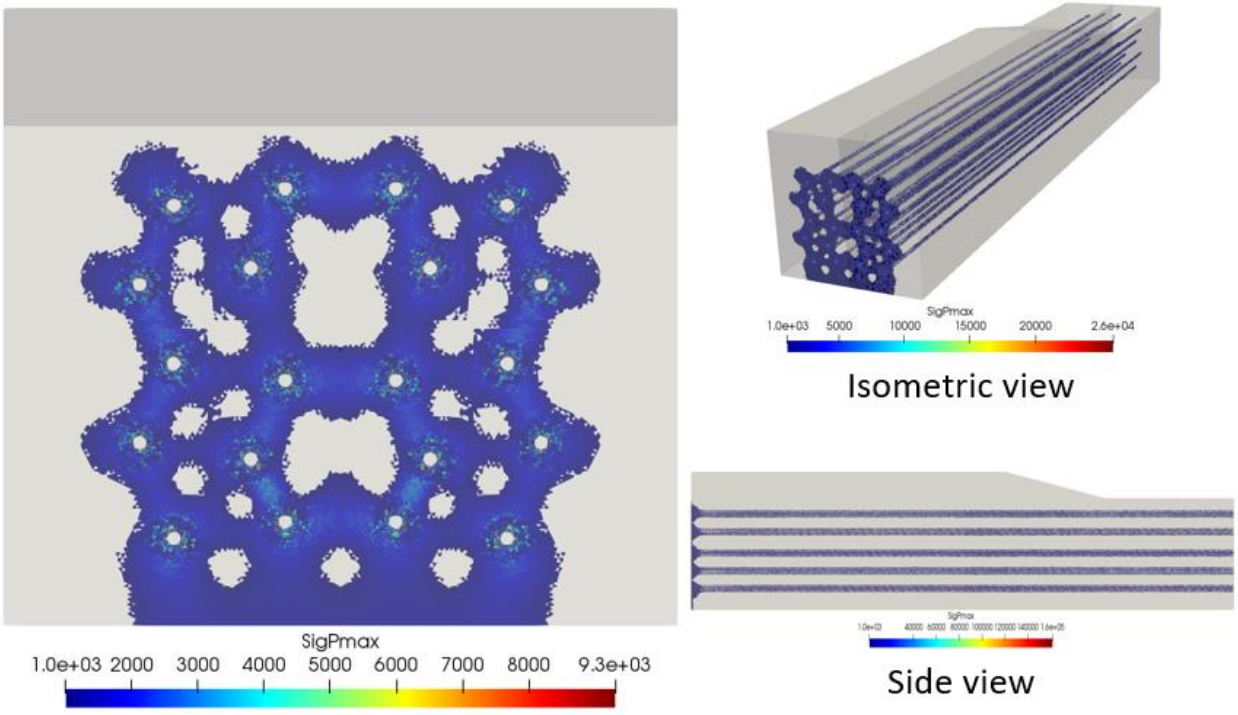

Figure 5.37 PSCC-WP: Tensile strength of 1000 psi

Chapter 6 : Development Performance-Base Engineered Cementitious Materials for Railroad Crossties

6.1 Determination of the Reference Mixture Design based on State Qualified Construction Materials List

To establish the appropriate range for mixture constituents, it is essential to understand the proportions currently used in industry practice. State Departments of Transportation (DOTs) typically approve mixture designs submitted by producers, and state-funded projects generally require the use of these approved mixtures. Accordingly, reviewing the mixture proportions endorsed by state DOTs is a necessary step in defining practical and regionally relevant design parameters.

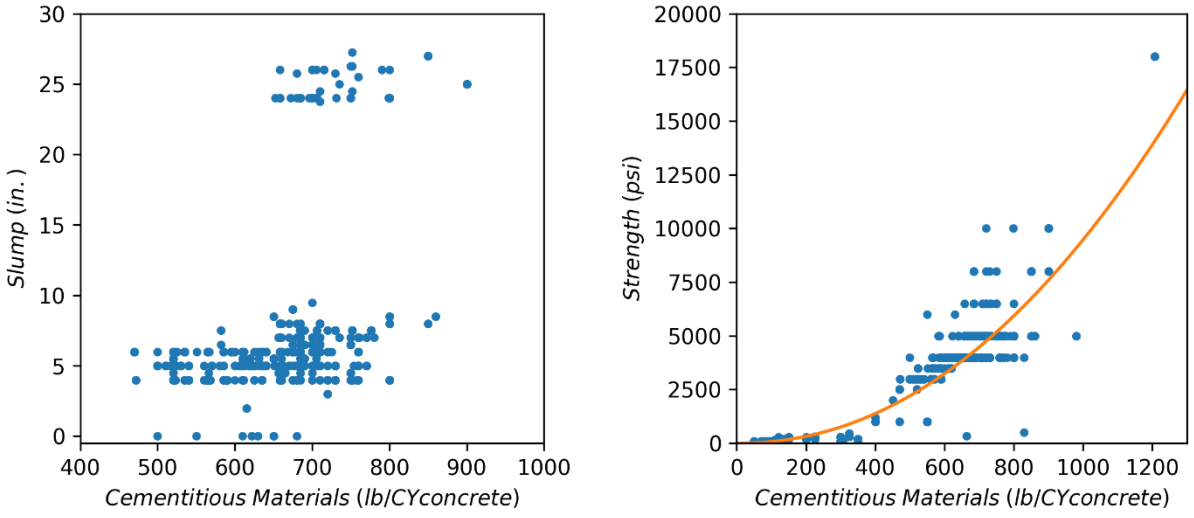

(a) (b)

Figure 6.1 Relationship amongst Design Strength, Total Cementitious Material Content, and Slump in QCML Database

Similar to other states, the Massachusetts Department of Transportation (MassDOT) [47] annually updates its Qualified Construction Materials List (QCML). Although the information provided for each mixture is limited, the database serves as a valuable reference for developing new concrete mixtures. Each entry includes: (1) producer, (2) producer location, (3) mixture identification, (4) concrete type (e.g., high-strength concrete), (5) design strength, (6) slump, (7) air content, (8) maximum nominal aggregate size, and (9) total cementitious material content. In total, 1,082 mixture proportions are available in the database, excluding mixtures with zero cementitious content. The reported design strengths range from 50 psi to 18,000 psi, covering a broad spectrum of structural applications. Figure 6.1 (b) shows that some mixes produce the slump higher than 23 inches, which is classified by the self-consolidating concrete.

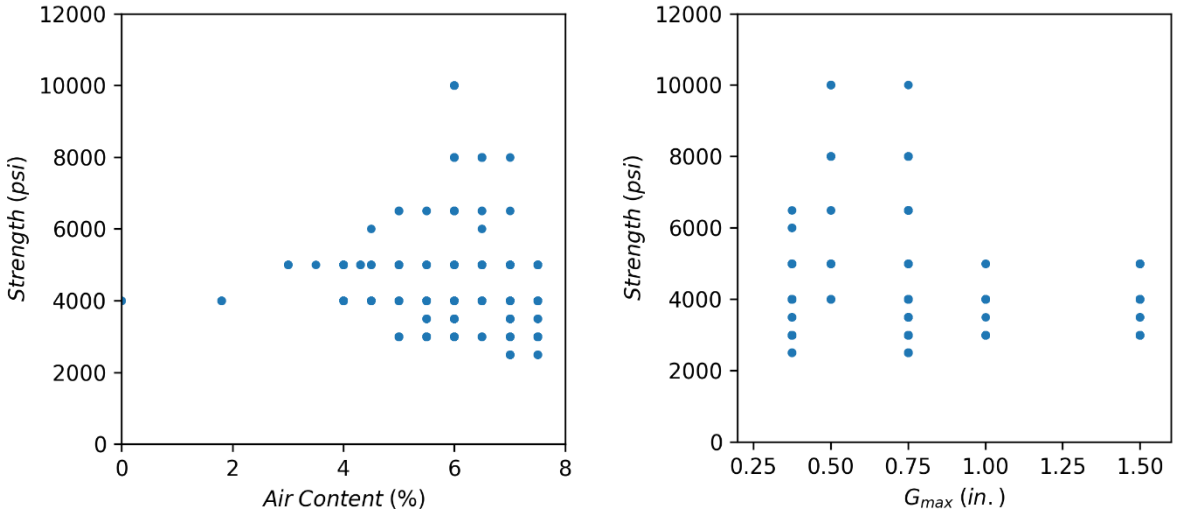

Figure 6.2 Relations of Design Strength, Air Content, and Nominal Maximum Aggregate Size

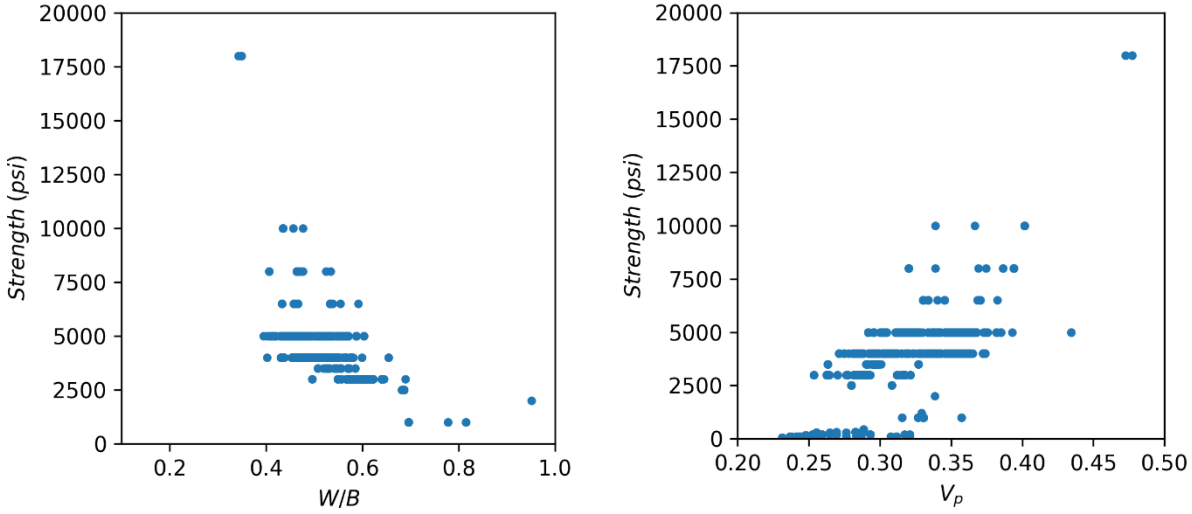

Figure 6.3 Estimated W/B ratio and Paste volume fraction (relative to 1 cubic yard of the concrete) with respect to strength

Presumably, the listed material is referenced to the ACI specifications [18], [48], and Figure 6.1 and Figure 6.2 show the relations amongst the available mixture information. Therefore, using the relationship between the water demand and the slump per the ACI211.1 [48], the corresponding paste volume content and water-to-binder ratios are estimated. Figure 6.3 illustrates the estimated water-to-binder (W/B) and paste volume ratios in relation to compressive strength. The results indicate that lower W/B ratios and higher paste volumes generally lead to higher strength. Therefore, as shown in Figure 4, the paste volume fraction and the water-to-binder (W/B) ratio exhibit a reciprocal relationship. For mixtures with design strengths between 7,000 psi and 15,000 psi, the W/B ratio ranges from 0.40 to 0.54, while the corresponding paste volume fraction varies from 0.32 to 0.40. It is worth noting that higher paste

content increases the potential for drying shrinkage [30], [49]. Accordingly, AASHTO PP-84 [27] limits the paste content to 25% by volume for mitigating shrinkage cracking. Nonetheless, the paste content is key for determining the workability of the concrete (i.e., about 5 in. of the slump at the job site).

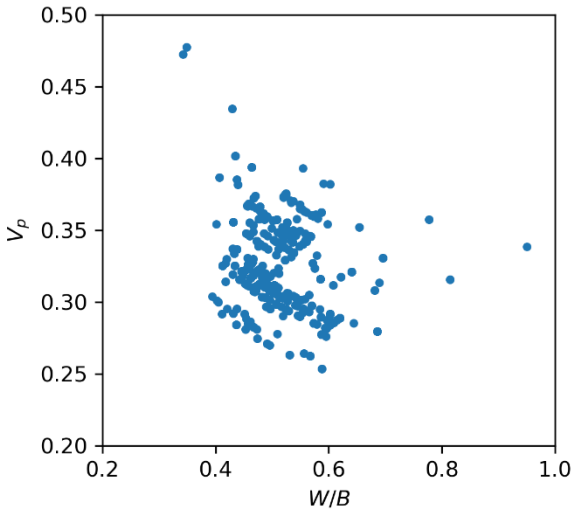

Figure 6.4 Relation between W/B and Paste volume fraction

Table 6.1 Limits on Cementitious Materials by ACI 318 [50] (for exposure class F3) and ACI 350R-20 [51]

SCMs	Max. % of Total Binder by Mass (exposure class F3)	Min. % of Total Binder by Mass (sulfate attack)	Min. % of Total Binder by Mass (corrosion)
Fly Ash	25	15	15
Slag Cement	50	50	35
Silica fume	10	5	5
Fly Ash + Natural Pozzolan or Silica Fume	35	–	–
Total of Fly Ash or Natural Pozzolan, Slag, and Silica Fume	50	–	–

Furthermore, it should be noted that mixture information related to supplementary cementitious materials (SCMs) is not provided in the QCML database. Nevertheless, ACI 318 [50] and ACI 350 [51] specify limits on SCM usage for the F3 (or EF3) exposure categories associated with freezing–thawing cycles, sulfate attack, and corrosive environments, as summarized in Table 6.1. In addition, ACI 232.3R [52] permits the use of high-volume fly ash mixtures, typically defined as those incorporating more than 50% cement replacement. Such mixtures can enhance durability and reduce permeability; however, their use requires careful consideration of early-age strength development and appropriate curing practices.

Table 6.2 Range of Mixture Parameters

Mixture Parameters	Minimum	Maximum
Binder Contents (lb / CY concrete)	608	1366
W/B	0.17	0.47
Silica Fume (%)	0	15
Fly Ash (%)	15	55
GGBFS (%)	15	45
Paste Content (% volume of the concrete)	30	47
Basalt Fiber (% volume of the concrete)	0	2

Considering the factors discussed above and the analysis of QCML-approved mixtures, the ranges of mixture parameters adopted in this study are summarized in Table 6.2. The binder content varies from 608 to 1,366 lb per cubic yard of concrete, with the upper bound corresponding to UHPC mixtures that exclude coarse aggregates. Because binder content is closely correlated with the water-to-binder ratio required to maintain designated workability, the resulting paste volume fraction for the mixtures examined in this study ranges from approximately 30% to 47%. It should be noted, however, that one objective of the mixture optimization process is to reduce paste content to the minimum practical level. In addition, the replacement ratios of supplementary cementitious materials (SCMs), specifically silica fume, fly ash, and GGBFS, were selected in accordance with the limits specified in ACI 318, ACI 232.3R, and ACI 350. Particular attention was given to the potential retardation of hydration associated with pozzolanic SCMs, ensuring that early-age strength development remains sufficient to satisfy the relevant AREMA requirements.

Chapter 7 : Experimental Program for Developing ECM for Railroad Crossties

7.1 Mixture Compositions

In this study, a total of 73 concrete mixture proportions were prepared and tested to develop a mix suitable for railroad crossties. Of these, 31 mixtures were used to identify the influence of mixture parameters on the targeted performance of the concrete. The reference ranges of the selected parameters are summarized in Table 6.2. Mixtures were systematically designed by varying binder content, cement type, and the replacement levels of supplementary cementitious materials. Additional variables included the water-to-binder ratio, the volumetric ratio of fine to coarse aggregates, paste volume fraction, and fiber dosage. These parameters were chosen to capture a representative range of mixture characteristics relevant to developing high-performance and ultra-high-performance concrete using locally available materials.

The cements used in this research were Type I, I/II, and III, supplied by Heidelberg Materials. The same manufacturer also provided the supplementary cementitious materials, including ground granulated blast-furnace slag (GGBFS), fly ash, and silica fume. The chemical admixtures used were a high-range water-reducing admixture and an air-entraining agent, both produced by Mapei. Basalt fibers, marketed under the trade name 'Minibar' and manufactured by Reforcetech, were incorporated as fiber reinforcement in selected mixtures.

The aggregates were obtained from a local supplier, Ondrick Natural Earth. The coarse aggregate consisted of granite and basalt, while the fine aggregate was a blend of quartz and mason sands. Figure 7.1 illustrates the particle size distributions of the aggregates used in this study. The coarse aggregate labeled "basalt" had a maximum nominal size of 1/2 in., whereas the "granite" coarse aggregate had a maximum nominal size of 3/8 in. The fine and coarse aggregates were proportioned in accordance with the gradation method proposed by Fuller and Thompson [53], targeting the 0.45 power-law curve to achieve an optimized particle packing.

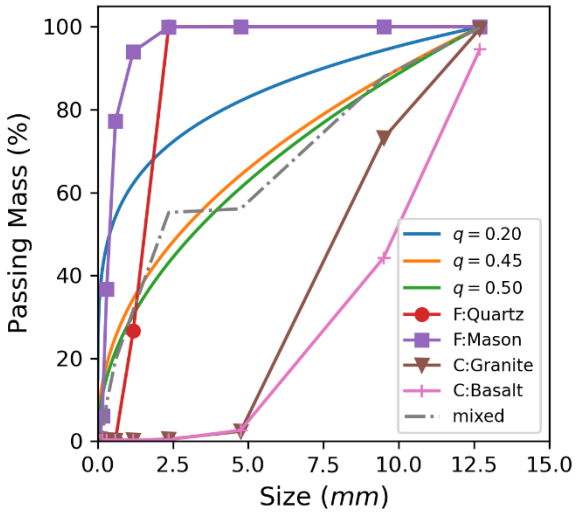

Figure 7.1 Passing Percent of Fine, Coarse, and Mixed Aggregates

Table 7.1 to Table 7.4 summarize the mixture proportions evaluated in this study, organized into four groups according to their intended purpose. Group 1, presented in Table 7.1, was developed to assess the effective dosage and fiber length of basalt fibers. The 28-day design strength for this group ranged from 5,000 to 6,200 psi; however, with the application of steam curing, the expected strength increased to approximately 6,000 to 7,000 psi.

Table 7.1 Mixture proportion of Group 1 (per a cubic yard of concrete)

Ingredients	M1	M2	M3	M4	M5	M6	M7	M8	M9
Cement (lb) (Type)	767 (III)	767 (III)	767 (III)	767 (III)	767 (III)	767 (III)	767 (III)	767 (III)	767 (III)
Silica Fume (lb) (Mass Ratio, %)	0 (0)	0 (0)	0 (0)	0 (0)	0 (0)	0 (0)	0 (0)	0 (0)	0 (0)
Fly Ash (lb) (Mass Ratio, %)	0 (0)	0 (0)	0 (0)	0 (0)	0 (0)	0 (0)	0 (0)	0 (0)	0 (0)
GGBFS (lb) (Mass Ratio, %)	0 (0)	0 (0)	0 (0)	0 (0)	0 (0)	0 (0)	0 (0)	0 (0)	0 (0)
Water (lb)	345	345	345	345	345	345	345	345	345
W/B	0.45	0.45	0.45	0.45	0.45	0.45	0.45	0.45	0.45
V_p (%)	35	35	35	35	35	35	35	35	35
S_A (%)	60	60	60	60	60	60	60	60	60
Coarse Aggregate (lb)	1062	1062	1062	1062	1062	1062	1062	1062	1062
Fine Aggregate (lb)	1594	1594	1594	1594	1594	1594	1594	1594	1594
V_f (%)	0.0	0.5	0.5	1.0	1.0	1.5	1.5	2.0	2.0
Fiber Type	-	L	S	L	S	L	S	L	S
Air (%)	5.0	4.5	4.5	4.0	4.0	3.5	3.5	3.0	3.0

V_p =volume fraction of paste
S_A =volume fraction of sand relative to the total aggregate volume
V_f =volume fraction of fibers, L =44mm fiber, S =22mm fiber

Table 7.2 Mixture proportion of Group 2 (per a cubic yard of concrete)

Ingredients	M10	M11	M12	M13	M14	M15	M16
Cement (lb)	641	624	628	618	611	775	775
(Type)	(I/II)	(I/II)	(I/II)	(I/II)	(I/II)	(III)	(III)
Silica Fume (lb)	0	0	0	0	0	179	179
(Mass Ratio, %)	(0)	(0)	(0)	(0)	(0)	(15)	(15)
Fly Ash (lb)	0	0	0	0	0	238	0
(Mass Ratio, %)	(0)	(0)	(0)	(0)	(0)	(15)	(0)
GGBFS (lb)	0	0	0	0	0	0	238
(Mass Ratio, %)	(0)	(0)	(0)	(0)	(0)	(0)	(20)
Water (lb)	301	293	295	291	287	357	357
W/B	0.47	0.47	0.47	0.47	0.47	0.30	0.30
V_p (%)	30	30	30	30	30	45	45
S_A (%)	50	50	50	50	50	30	30
Coarse Aggregate (lb)	1483	1445	1454	1431	1414	1657	1657
Fine Aggregate (lb)	1483	1445	1454	1431	1414	710	710
V_f (%)	0.0	0.0	0.5	1.0	1.5	0.0	0.0
Fiber Type	-	-	S	S	S	-	-
Air (%)	3.0	5.5	4.4	5.4	6.0	3.0	3.0

V_p =volume fraction of paste

S_A =volume fraction of sand relative to the total aggregate volume

V_f =volume fraction of fibers, L =44mm fiber, S =22mm fiber

Group 2 consists of air-entrained concrete mixtures reinforced with 22-mm basalt fibers at varying dosages (M10 to M14), along with two mixtures evaluated under steam curing conditions (M15 and M16). Although the water-to-binder ratio is identical to that of Group 1 (W/B=0.47), the proportion of fine aggregate relative to total aggregate volume is lower in Group 2. The 28-day compressive strengths range from approximately 5,000 to 6,200 psi, which is comparable to the strengths obtained for Group 1. It is noteworthy that the mixtures in Groups 1 and 2 do not meet the compressive strength requirements specified in the AREMA Manual. This outcome is attributable to the more pronounced influence of basalt fibers in lower-strength concretes, where their contribution to mechanical performance is relatively more significant than in higher-strength mixtures.

Table 7.3 Mixture proportion of Group 3 (per a cubic yard of concrete)

Ingredients	M17	M18	M19	M20	M21	M22	M23	M24
Cement (lb)	796	739	683	626	569	512	455	512
(Type)	(I/II)	(I/II)	(I/II)	(I/II)	(I/II)	(I/II)	(I/II)	(I/II)
Silica Fume (lb)	171	171	171	171	171	171	171	0
(Mass Ratio, %)	(15)	(15)	(15)	(15)	(15)	(15)	(15)	(0)
Fly Ash (lb)	171	228	284	341	398	455	512	626
(Mass Ratio, %)	(15)	(20)	(25)	(30)	(35)	(40)	(45)	(55)
GGBFS (lb)	0	0	0	0	0	0	0	0
(Mass Ratio, %)	(0)	(0)	(0)	(0)	(0)	(0)	(0)	(0)
Water (lb)	228	228	228	228	228	228	228	228
W/B	0.20	0.20	0.20	0.20	0.20	0.20	0.20	0.20
V_p (%)	35	35	35	35	35	35	35	35
S_A (%)	60	60	60	60	60	60	60	60
Coarse Aggregate (lb)	1062	1062	1062	1062	1062	1062	1062	1062
Fine Aggregate (lb)	1594	1594	1594	1594	1594	1594	1594	1594
V_f (%)	1.0	1.0	1.0	1.0	1.0	1.0	1.0	1.0
Fiber Type	S	S	S	S	S	S	S	S
Air (%)	4.0	4.0	4.0	4.0	4.0	4.0	4.0	4.0
V_p =volume fraction of paste S_A =volume fraction of sand relative to the total aggregate volume V_f =volume fraction of fibers, L =44mm fiber, S =22mm fiber								

Groups 3 and 4, summarized in Table 7.3 and Table 7.4, were designed to investigate the effects of fly ash and GGBFS, respectively. The binder mass-replacement ratio was varied from 15% to 45%, and the resulting compressive strength, impact resistance, and abrasion resistance were evaluated. To maintain the target workability (i.e., a slump of 3–5 in.), the W/B ratio and corresponding volume fractions in the mixture were adjusted as needed. Group 3 mixtures achieved compressive strengths ranging from 10,000 to 13,000 psi, whereas Group 4 mixtures produced strengths ranging from 10,000 to 14,000 psi at 28-days. Therefore, when applying the steam curing for those groups of concrete, the strength can be achieved within shorter curing time.

Table 7.4 Mixture proportion of Group 4 (per a cubic yard of concrete)

Ingredients	M25	M26	M27	M28	M29	M30	M31
Cement (lb)	726	674	622	571	519	467	415
(Type)	(I/II)	(I/II)	(I/II)	(I/II)	(I/II)	(I/II)	(I/II)
Silica Fume (lb)	156	156	156	156	156	156	156
(Mass Ratio, %)	(15)	(15)	(15)	(15)	(15)	(15)	(15)
Fly Ash (lb)	0	0	0	0	0	0	0
(Mass Ratio, %)	(0)	(0)	(0)	(0)	(0)	(0)	(0)
GGBFS (lb)	156	207	259	311	363	415	467
(Mass Ratio, %)	(15)	(20)	(25)	(30)	(35)	(40)	(45)
Water (lb)	259	259	259	259	259	259	259
W/B	0.25	0.25	0.25	0.25	0.25	0.25	0.25
V_p (%)	35	35	35	35	35	35	35
S_A (%)	60	60	60	60	60	60	60
Coarse Aggregate (lb)	1062	1062	1062	1062	1062	1062	1062
Fine Aggregate (lb)	1594	1594	1594	1594	1594	1594	1594
V_f (%)	1.0	1.0	1.0	1.0	1.0	1.0	1.0
Fiber Type	S	S	S	S	S	S	S
Air (%)	4.0	4.0	4.0	4.0	4.0	4.0	4.0

V_p =volume fraction of paste

S_A =volume fraction of sand relative to the total aggregate volume

V_f =volume fraction of fibers, L =44mm fiber, S =22mm fiber

7.2 Preparation of Specimens

The mixture design process began with determining the normal consistency of the cements used, following the procedures outlined in ASTM C187-11 [54]. The measured normal consistency values for the Type I/II and Type III cements were 0.265 and 0.292, respectively. The higher consistency requirement of the Type III cement is attributed to its finer particle size, which increases its surface area and water demand. These observations are consistent with findings reported in previous studies [55]. Specimens were subsequently cast and cured in water maintained at 73F until the designated testing ages, in accordance with ASTM C192 [56] regardless of different experiments.

7.3 Compressive Strength Measurement

The compressive strength of the developing mixture proportions of the concrete is measured in accordance with ASTM C39 [57]. For compressive strength and impact load tests, cylindrical specimens with the dimension of 3 in. diameter and 6 in. length are prepared.

7.4 Impact Load Test

The impact resistance of the developed concrete mixtures was evaluated using a custom testing method designed by the research team. The experimental setup for the test apparatus is illustrated in Figure 7.2. This method can be readily implemented as a field test to provide a relative comparison of different concrete mixture proportions. Although additional research is required to assess the precision and repeatability of the method, at least two cylinders with identical mixture proportions were tested for each case, and the average value of the measurements is reported herein.

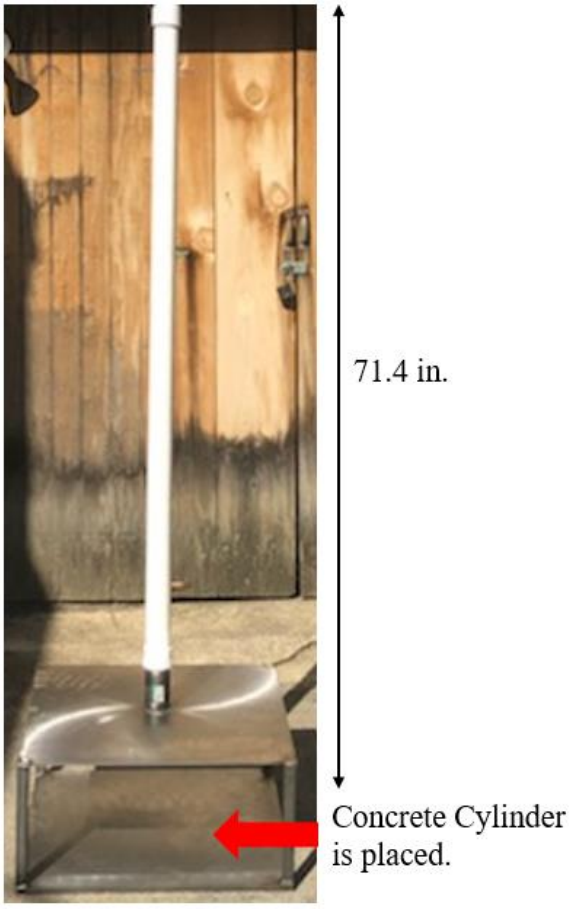

Figure 7.2 Apparatus of Impact Loading Test

A steel hammer weighing 18.3 lb (8.33 kg) was dropped from a height of 71.4 in. (1.81 m), imparting approximately 148 J of kinetic energy to the concrete cylinder during each free fall. After every hammer drop, the resulting mass loss of the specimen was recorded. This process was repeated until the cumulative mass loss exceeded 20% of the specimen's original mass. The test was conducted using standard concrete cylinders measuring 3 in. in diameter and 6 in. in length.

Mass loss was recorded whenever any portion of the specimen detached from the original cylinder, regardless of the number or size of cracks induced by the impact loading. Accordingly, mixtures that required a greater number of impact events to exceed 20% mass loss were considered to exhibit superior impact-loading resistance.

7.5 Surface Reflectance Measurement

The abrasion resistance of the developing concrete was evaluated by measuring the light reflectance of the concrete surface. Although ASTM C1138 [40] provides a standardized method for assessing abrasion resistance by rotating steel grinding balls across a submerged concrete surface, the procedure is destructive and unsuitable for repeated or nondestructive evaluation. Therefore, this study employed the Labsphere LiDAR Reflectometer Kit as a nondestructive alternative. To minimize potential interference from ambient sunlight, a reflectometer equipped with multiple LiDAR wavelengths was used, as shown in Figure 7.3. Among the available options, the 850 nm LiDAR light source was selected for measuring the surface roughness of the concrete.

Figure 7.3 LabSphere Portable Reflectometer Kit

It is important to note that the surface roughness of concrete is influenced by numerous factors, including mixture proportions (e.g., aggregate characteristics), curing and finishing processes, and damage sustained during service. Consequently, establishing a practical and standardized property directly related to surface roughness for the developing mixtures is challenging. Therefore, the results reported herein may have limited applicability for practical use. For consistency, specimens with dimensions of 4in.×4in.×1in. were prepared for each mixture. As shown in Figure 7.4, acrylic molds were used to minimize potential surface defects associated with conventional formwork materials.

(a) Acrylic Molds for Reflectance Samples

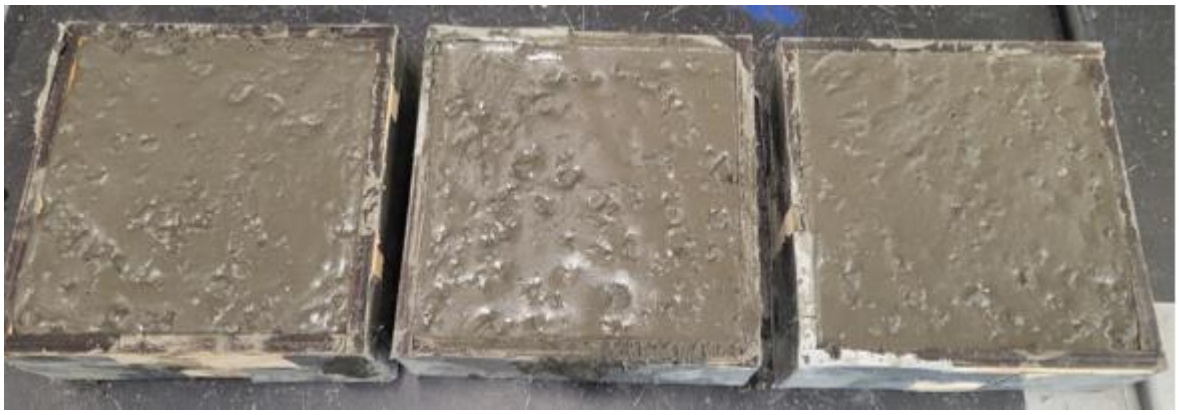

(b) Cast Reflectance Specimens

Figure 7.4 Preparation of Specimens for Measuring Reflectance of Concrete Surface

The cast specimens were de-molded after 24 hours and subsequently cured under the designated environmental conditions. The initial surface reflectance of each specimen was recorded prior to environmental exposure. Specimens were then subjected to three curing regimes: (1) standard curing at 73F (23C) with over 95% relative humidity, (2) oven curing at 158F (70C), and (3) outdoor exposure during December-January 2023-2024 in Massachusetts. After curing, the surface reflectance of each specimen was measured to evaluate changes associated with the different curing environments. Note that the Labsphere reflectometer measures surface reflectance at 25 grid points, and the reported reflectance for a given surface is the average of these measurements.

Chapter 8 : Experimental Results and Discussions for Development of ECM for Railroad Crossties

8.1 Compressive Strength with Various Mixture Parameters

Based on the experimental results for the developing mixture proportions, the measured compressive strengths ranged from 3,644 psi to 14,505 psi across all testing ages. When estimating the potential design strength using the hyperbolic function prescribed in ACI 209 [58], [59], the corresponding asymptotic strengths at infinite time fall within a similar range, approximately 5,069 psi to 13,931 psi.

8.1.1 Effect of Water-to-Binder (W/B) Ratio on Strength

The water-to-binder ratio (W/B) is a key parameter governing the strength development of concrete. ACI 318 [50] specifies prescriptive limits for this ratio to mitigate potential durability issues under various exposure conditions. Figure 8.1 presents the relationship between compressive strength and the W/B ratio at different test ages. It is observed that an increase in the W/B ratio leads to an exponential decrease in compressive strength across all ages.

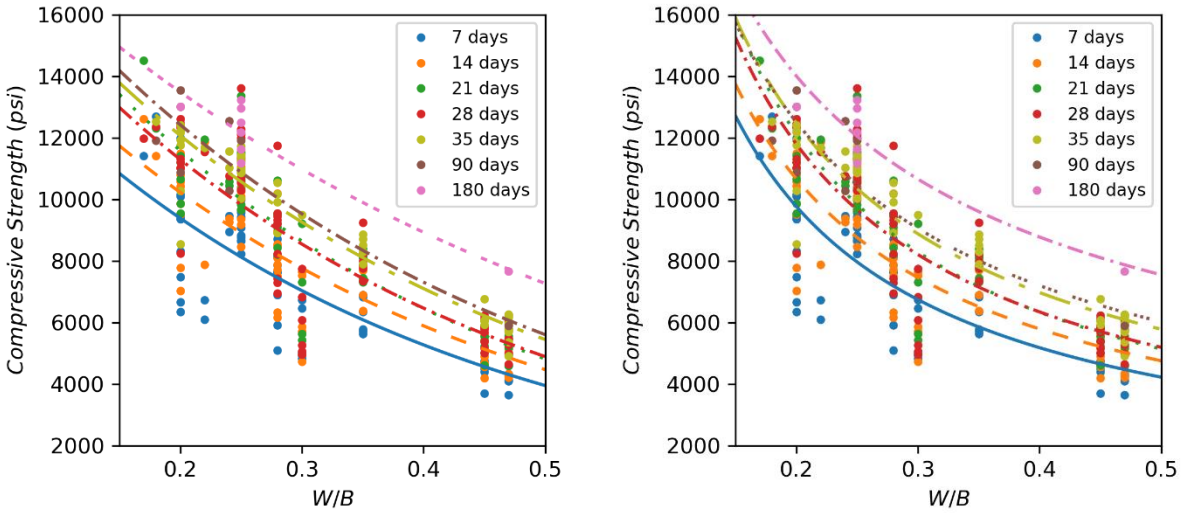

(a) Fitted with Exponential Function (b) Fitted with Power Function

Figure 8.1 Strength with varying W/B ratio

Abrams proposed an empirical relationship between compressive strength and the volumetric water-to-binder ratio (Wv/Bv) [60], [61], as expressed in Eq.(8.1).

$$S = \frac{14000}{7^{W_v/B_v}} \tag{8.1}$$

While the coefficients in the Abrams equation (e.g., 14,000 and 7) were originally calibrated using Abrams's experimental data, they may be adjusted based on the data obtained in this study. It should be noted that, in current practice, the W/B ratio is typically defined on a mass basis

rather than a volumetric basis; therefore, the corresponding coefficients may also require modification to reflect this convention. For the obtained data, both power and exponential functions were evaluated to assess their goodness of fit to the experimental data. The results indicate that the exponential function provides a slightly better representation of the relationship between the W/B ratio and compressive strength across all test ages, although the difference between the two functions is not substantial. It confirms that the Abrams equation (Eq. (8.1)), which uses the exponential function as the base form. It is also observed that reductions in the W/B ratio below 0.25 do not lead to significant improvements in compressive strength. Consequently, additional investigation results using supplementary trial mixtures designed to examine this trend in greater detail will be presented in a later section.

8.1.2 Effect of Inclusion of Basalt Fibers

Figure 8.2 illustrates the effect of varying basalt fiber dosages on the compressive strength development for mixtures incorporating 44 mm and 22 mm fibers, compared with the reference mixture without fibers (i.e., Group 1). In addition, Figure 8.3 presents the variation in compressive strength as a function of fiber dosage across different test ages.

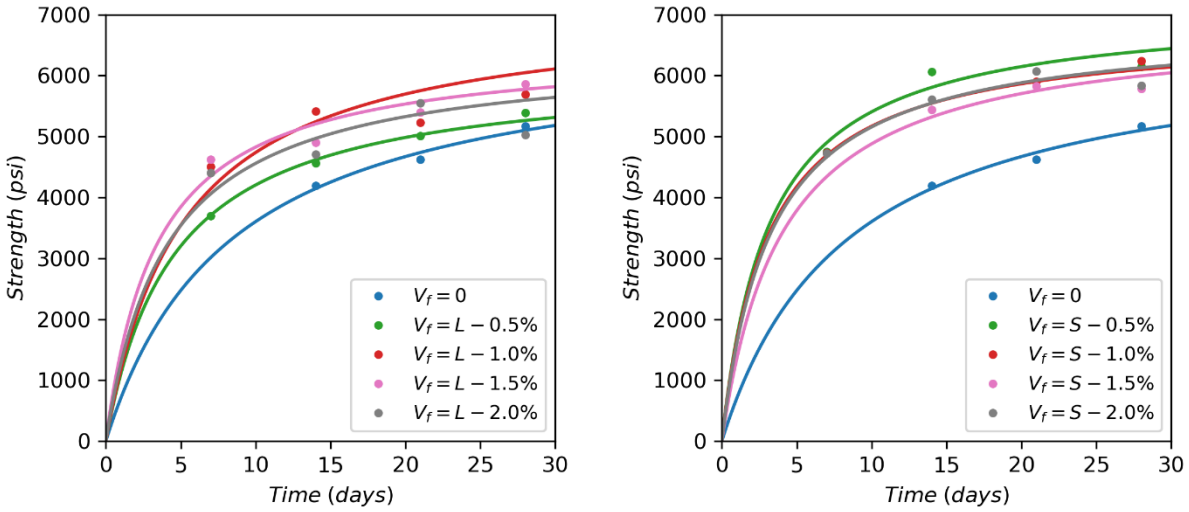

(a) (b)

Figure 8.2 Strength development of concrete with different dosage of Basalt fibers: (a) Inclusion of 44-mm fibers and (b) Inclusion of 22-mm fibers

It was observed that the inclusion of basalt fibers enhanced the compressive strength across all test ages. However, the magnitude of improvement varied with both fiber dosage and testing age. Based on regression analysis of the 28-day compressive strength results, each 1% increase in fiber dosage corresponds to an approximate strength gain of 660 psi. As shown in Figure 8.3, the maximum benefit from fiber inclusion was achieved within the dosage range of 0.5% to 1.5%, although the degree of enhancement varied slightly with the test age. When comparing the performance between the two fiber lengths (i.e., 44 mm and 22 mm), the 22 mm fibers exhibited slightly superior compressive strength, providing an average increase of approximately 511 psi

over the 44 mm fibers across all dosages, with statistical significance at the 95% confidence level.

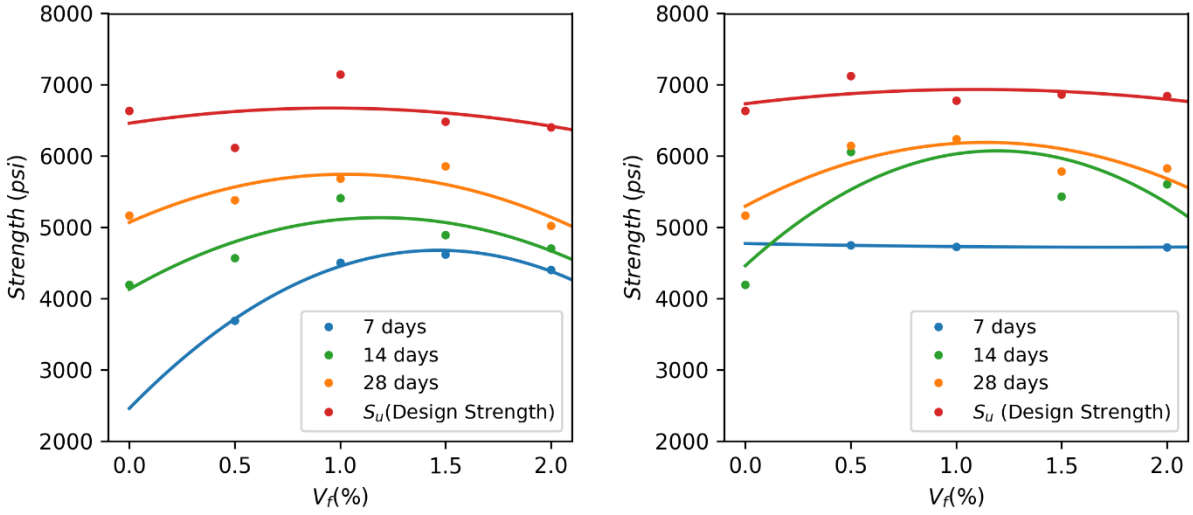

(a) (b)

Figure 8.3 Comparison of Strength with different dosage of Basalt fibers: (a) Inclusion of 44-mm fibers and (b) Inclusion of 22-mm fibers

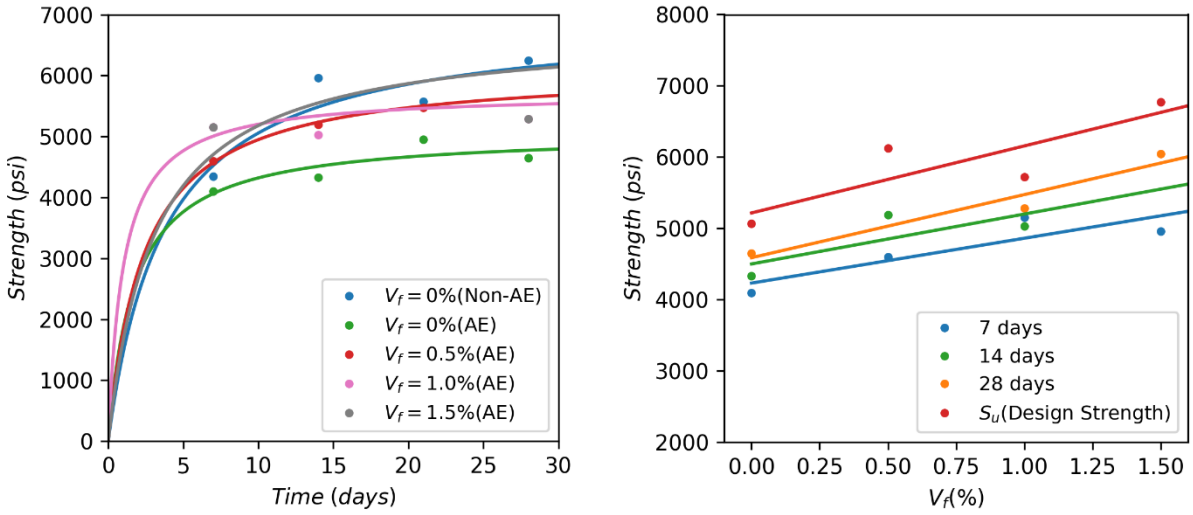

(a) (b)

Figure 8.4 Strength development of Air-Entrained Concrete with Different Dosage of 22-mm Basalt fibers

Figure 8.4 shows the strength development with different fiber dosages for the air-entrained concrete. (i.e., M10 to M14 in Group 2) The air contents of the concrete range from 4.4 to 6.0%. It was observed that the incorporation of entrained air in the concrete resulted in a reduction in compressive strength. Specifically, an increase of 1% in air content led to an approximate decrease of 409 psi in 28-day compressive strength. In contrast, the inclusion of basalt fibers exhibited a positive effect on compressive strength. Each 1% increase in fiber dosage yielded an

approximate strength gain of 660 psi at 28 days. It is noted that these results correspond to mixtures produced without air entrainment.

The literature reports mixed findings regarding the influence of basalt fibers on the mechanical and rheological properties of concrete [62], [63]. In some studies, basalt fiber incorporation has been shown to improve strength, whereas other studies have documented strength reductions under certain conditions. In contrast, the results of this research consistently demonstrated a strength increase of approximately 600 psi for every 1% increase in fiber dosage. For context, ACI 214 [64] specifies that the standard deviation for strength control in concrete with a specified compressive strength (f'c) below 5,000 psi typically ranges from 250 to 300 psi to be classified as "Good" control under laboratory condition, indicating that the observed improvements exceed typical strength variability thresholds.

8.1.3 Effect of Fly Ash on Compressive Strength

A ternary binder system was employed for this comparison, in which each mixture contained a fixed 15% silica fume while the proportions of Type I/II cement and fly ash were varied within a combined limit of 35% of the total paste content (See Group 3). Additionally, all mixtures incorporated 1% of 22-mm basalt fibers to evaluate the strength performance under consistent fiber reinforcement conditions. Figure 13 illustrates the strength development of concrete mixtures with fly ash contents ranging from 15% to 55%.

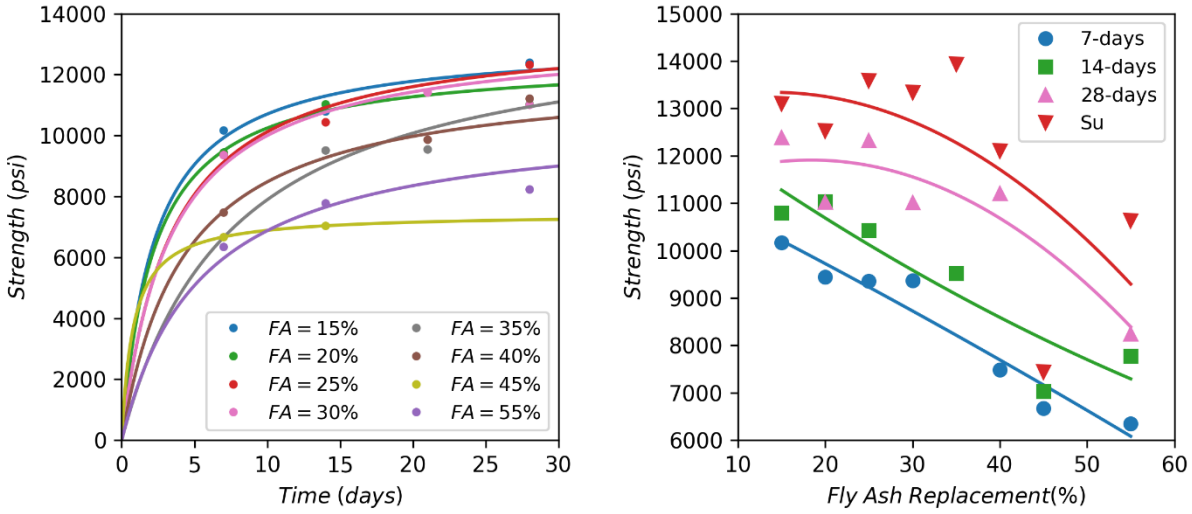

(a) (b)

Figure 8.5 Strength development with Different Replacement Ratios of Fly Ash

As shown in Figure 8.5 (b), the compressive strength at all test ages decreases with increasing fly ash content. When the fly ash replacement level is 15%, the concrete exhibits strengths ranging from approximately 10,000 psi to 13,000 psi. However, a pronounced reduction in strength is observed once the fly ash content exceeds 30%. An even greater loss in strength occurs when the replacement level surpasses 40%, indicating that high-volume fly ash usage significantly compromises both early- and later-age strength performance under the tested mixture conditions.

These results indicate a nonlinear relationship between fly ash content and compressive strength. While this nonlinearity is discernible at early ages, it becomes more pronounced at later ages, suggesting that the adverse impact of higher fly ash contents persists and intensifies over time.

As summarized in Table 6.1, ACI 318 and ACI 350 limit the fly ash replacement level to a maximum of 25% for concrete designated under exposure class F3. Based on the present results, every 10% increase in fly ash content leads to an approximate reduction of 1,000 psi in compressive strength, regardless of test age. Accordingly, a strength reduction of approximately 2,500 psi can be expected when 25% of the total cementitious content is replaced with fly ash per ACI 318 and 350.

8.1.4 Effect of Ground Granulated Blast Furnace Slag (GGBFS) on Compressive Strength

The concrete mixtures used to evaluate the effect of ground granulated blast furnace slag (GGBFS) on compressive strength contained 35% paste content with a water-to-binder ratio of W/B=0.20. A ternary binder system consisting of Type I/II cement, silica fume, and GGBFS was employed. Silica fume replacement was fixed at 15% of the binder in all mixtures, while the cement content was adjusted according to the varying GGBFS replacement levels. Additionally, 1% by volume (V_f=1%) of 22-mm basalt fibers was incorporated uniformly across all mixtures in this study.

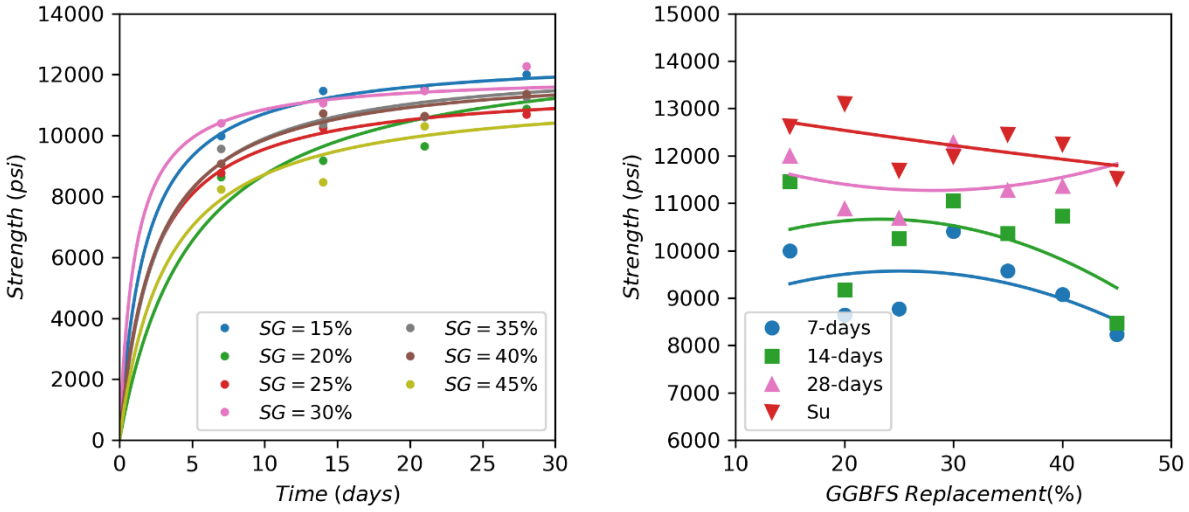

(a) (b)

Figure 8.6 Strength development with Different Replacement Ratios of GGBFS

The resulting compressive strength developments for the series of mixtures (Group 4) are presented in Figure 8.6. As shown, the incorporation of GGBFS influenced strength gain across different curing ages, with average strength increasing consistently over time. This trend differs from observations commonly reported in the literature [65], [66], [67], where higher GGBFS replacement levels typically result in lower early-age strength followed by enhanced later-age strength. In contrast, the current results do not clearly demonstrate this crossover behavior within

the tested replacement range and mixture conditions. Li et. al [67] reported that some proper amounts of the GGBFS provide the filling effect of particles, improving the strength. Nonetheless, the pozzolanic reaction delays the production of C-S-H, represented by the delayed strength development. It is noted that the measured compressive strengths ranged from 8,220 psi (corresponding to the mixture with 45% GGBFS at 7 days) to 13,604 psi (corresponding to the mixture with 15% GGBFS at 28 days). This strength range exceeds those commonly reported in the literature, which are typically on the order of 3,600 psi to 8,000 psi. Furthermore, the rate of strength reduction at earlier age is smaller than that of the mixture with varying fly ash. While the GGBFS delays hydration due to pozzolanic reaction [68], its degree appears to be smaller than that derived by fly ash.

8.1.5 Effect of Paste Content

Figure 8.7 illustrates the relationship between binder content (or paste ratio) and compressive strength across all mixture proportions. The binder content is expressed in two ways: as the total binder weight per cubic yard of concrete (lb/CY) and as the volumetric ratio of binder to the total concrete volume.

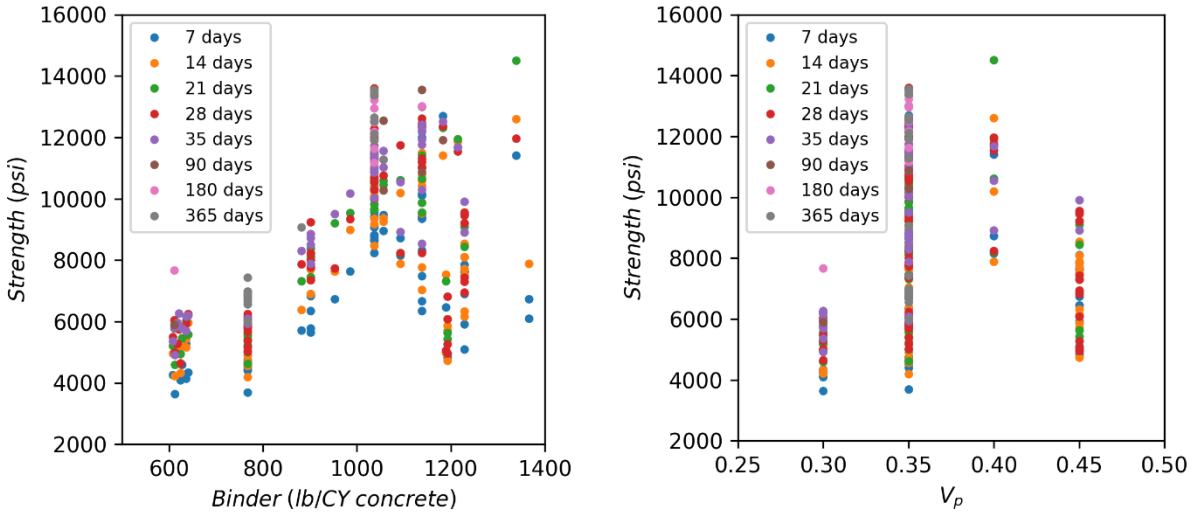

(a) (b)

Figure 8.7 Comparison of Compressive Strength with Different Paste Content (a) by Mass and (b) by Volume Ratio (V_p)

As a result, an increase in binder content generally leads to an improvement in compressive strength. However, when the binder volume fraction exceeds approximately 40% (e.g., 45%), no further enhancement in strength is observed. This trend is consistent with the results shown in Figure 3(b), where the compressive strength increases up to a paste volume fraction of 40%. Kolias and Georgiou [69] reported that compressive strength decreases with increasing paste content when the W/B ratio is held constant. In contrast, Jiang et al. [70] investigated the influence of excessive paste thickness (EPT) on the rheological and mechanical properties of concrete and found that the strength increases with EPT up to a certain limit, after which it decreases with further increases in paste thickness. It is also noteworthy that a higher paste

volume generally results in greater drying shrinkage [30], [71]; however, this aspect is beyond the scope of the present study.

8.1.6 Heat Treatment Effect on Compressive Strength at 1 day

The curing temperature significantly influences the rate of hydration, determining the different strengths [72]. To simulate the steam curing condition, a set of specimens prepared by M15 and M16 is cured in a chamber of which temperature is 176F (80C), and the resulting compressive strength at 1 day is shown in Figure 16. Note that the difference of two mixes is M16 used GGBFS instead of fly ash incorporated with Type III cement and 15% of the silica fume.

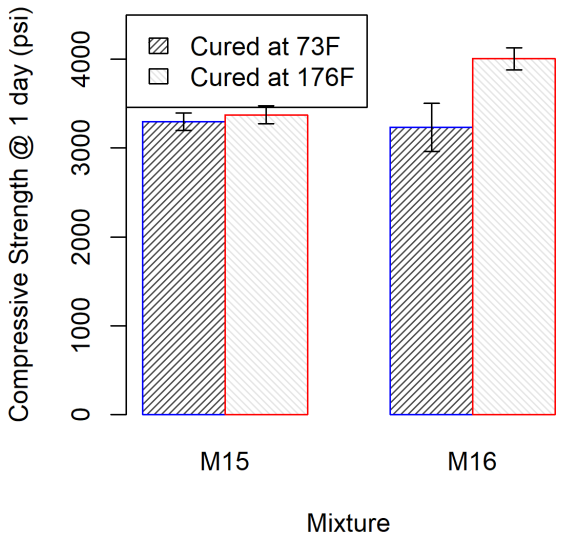

Figure 8.8 Heat Treatment Effect at 1 day

As a result, negligible differences are observed in M15, while about 24% increment was obtained for M16 specimens. It is known that higher curing temperatures accelerate hydration, leading to higher strength at a given test age. However, it is possible that such high temperature can produce irregular microstructure, degrading the strength [73], [74]. Even if it was reported that such "cross-over" point happen at about 3 days [19], [75], [76], the use of Type III cement can accelerate such a point. In other words, the increment of strength due to the accelerated hydration can be compensated by the degradation of microstructure due to high temperature. While no significant difference in the strengths of M15 specimens can be explained by this compensated effect, M16 specimens still showed significant improvement of the strength under high temperature.

8.2 Impact Resistance of Developing Concrete

To evaluate the impact resistance of the developed mixture, two groups of mixtures were prepared for comparison. The objective of this comparison was twofold: (1) to assess the effect of basalt fiber inclusion in the concrete, and (2) to examine the influence of cement replacement levels using fly ash. Accordingly, the concrete mixtures evaluated in this category were divided into two groups. The first group, with specified compressive strengths ranging from 6,000 to

7,000 psi (i.e., Group 1), was used to assess the influence of basalt fiber inclusion. These specimens were tested to determine the optimal fiber dosage and fiber length in terms of impact-loading resistance. It is noted that the specimens in this group were tested at an age of one year. Based on the fiber content identified from this phase (i.e., Vf=1% short basalt fiber), a second group of mixtures (i.e., Group 3) that prepared with varying fly ash replacement levels was evaluated. The specified compressive strength of the second group ranged from 12,000 to 14,000 psi, and the specimens were tested at an age of 35 days.

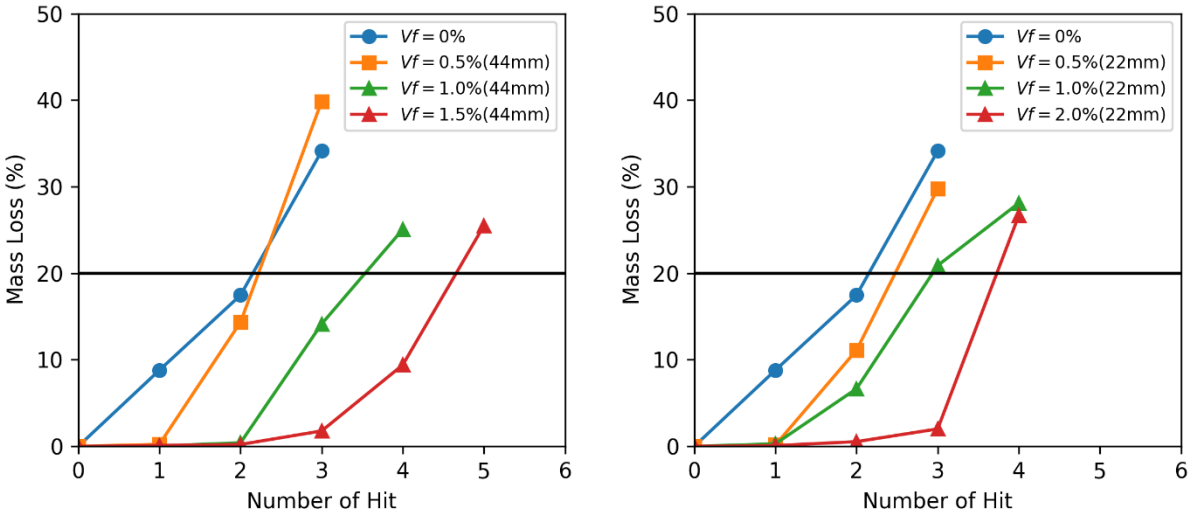

(a) (b)

Figure 8.9 Comparison of Impact Test for the Concretes with (a) 44-mm and (b) 22-mm Basalt Fibers

Figure 8.9 presents the mass-loss response of the specimens under successive impact loading for mixtures incorporating different types and dosages of basalt fiber. The results indicate that the mixture with a fiber volume fraction of V_f=0.5% exhibited improved impact resistance compared with the reference concrete (i.e.,f'c=4,500 psi) However, irrespective of fiber length (22 mm or 44 mm), all fiber-reinforced mixtures experienced mass losses exceeding 20% after the third impact loading. In general, higher fiber dosages result in improved resistance to impact loading. When a fiber volume fraction of V_f=1.0% is used, the mass loss of the specimens reinforced with both 22 mm and 44 mm basalt fibers exceeds 20% after four impact loadings. However, at each impact event, the mixture containing the 44 mm fibers exhibits comparatively lower mass loss, indicating better impact resistance than the corresponding 22 mm fiber mixture. It is noted that the diameter of the basalt fibers is identical for both the 22 mm and 44 mm lengths. Consequently, the total fiber volume is governed solely by the fiber count, which is inversely proportional to the fiber length when the volume fraction is fixed. Therefore, a mixture containing 1.0% of 44 mm fibers has approximately the same total fiber count—and thus the same effective fiber volume, as a mixture incorporating 2.0% of 22 mm fibers. Similarly, 0.5% of 44 mm fibers correspond to the same total fiber count as 1.0% of 22 mm fibers. In this context, the 22 mm fiber showed slightly better performance than the 44 mm fiber in the impact loading resistance.

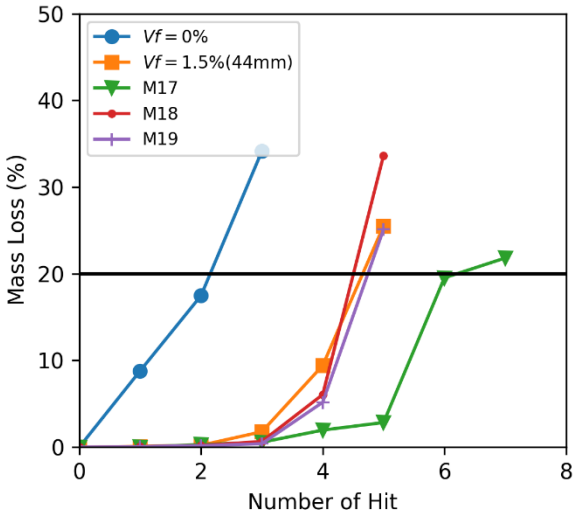

Figure 8.10 Comparison of Impact Test for the Concretes with M17, M18, and M19

Figure 8.10 compares the impact-loading performance of the reference concrete and the mixture containing 1.5% of the 44-mm basalt fibers with that of the developing mixtures incorporating different fly ash replacement ratios. The results indicate that the mixture with 15% fly ash replacement exhibited the highest impact resistance. Meanwhile, the mixtures with 20% and 25% fly ash replacement demonstrated performance levels comparable to that of the concrete containing 1.5% of the 44-mm basalt fibers.

Mixture	1st Impact	2nd Impact	3rd Impact	4th Impact
M17				
M18		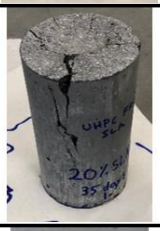		
M19				

Figure 8.11 Samples of the Concrete Failure after Impact Loading up to 4 Times

Figure 8.11 shows the damaged specimens after applying each impact loading. As considering only 4 impact loading, it is observed that the mixture with 15% of the fly ash showed relatively less mass loss as compared to the other specimens such as the mixture with 25% of the fly ash replacement ratio (i.e., M19).

8.3 Surface Reflectance of Developing Concrete

Figure 8.12 shows the specimens used to measure reflectance after exposure to different environmental conditions. The mixture used for this experiment is M19 in Group 3, producing the highest ultimate strength. (i.e., 13,590 psi) The color and surface texture of the three specimens differ noticeably. The specimen cured under standard conditions exhibits the brightest color, primarily due to calcium hydroxide residue on the surface, which dissolved and redeposited in the curing water. Consequently, the specimens cured outdoors and, in the oven, appear darker than the ones cured in water. The outdoor-cured specimen, in particular, shows the most irregular color variation across its surface. Overall, the results demonstrate that curing conditions significantly influence the resulting concrete surface characteristics.

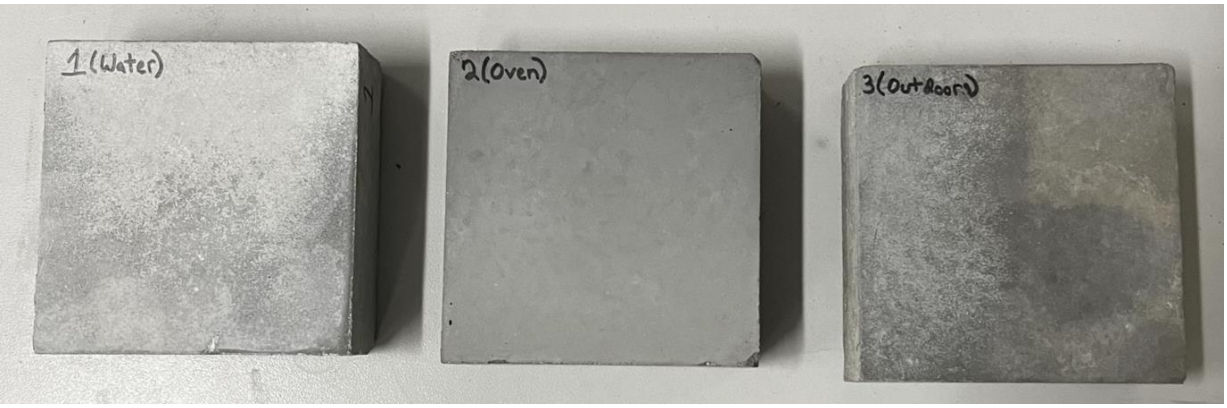

(a)

(b)

Figure 8.12 Specimens after exposure to different environmental conditions: (a) Front Face and (b) Side Face

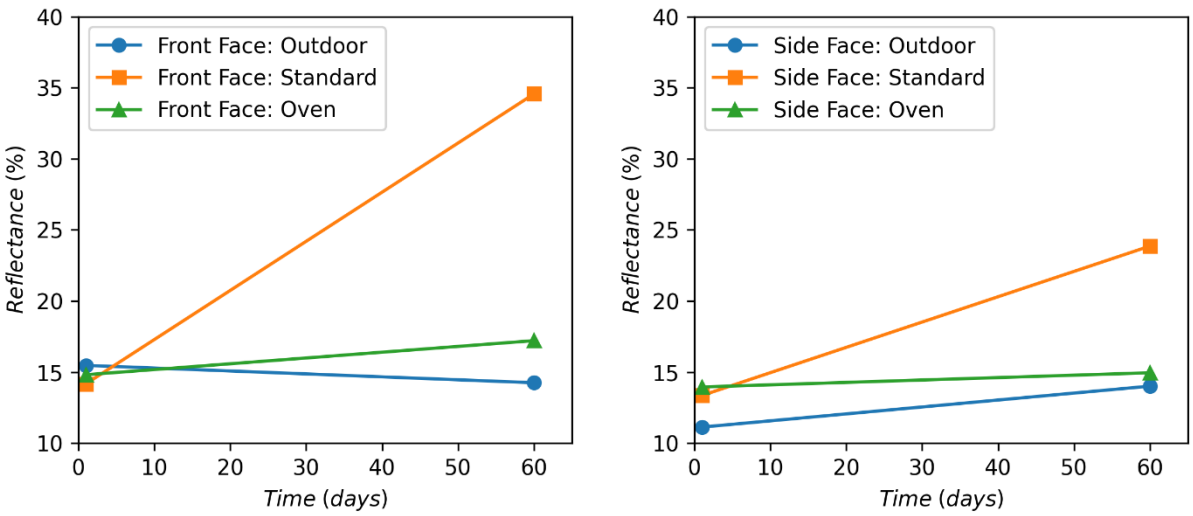

(a) (b)

Figure 8.13 Reflectance Values for Specimens exposed to different environmental conditions: (a) Front Face and (b) Side Face

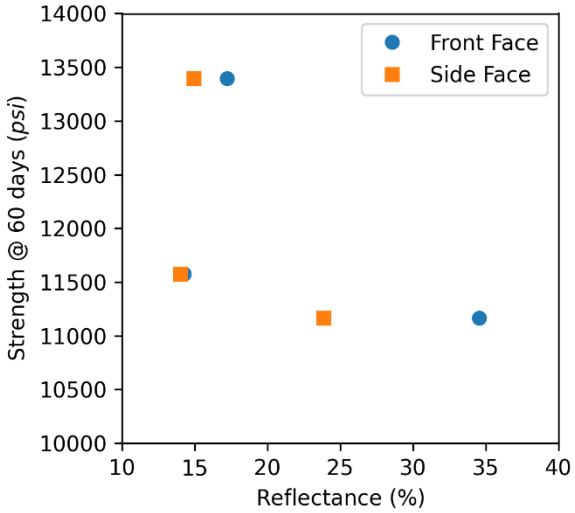

Figure 8.14 Relationship between Strength and Surface Reflectance

Figure 8.13 presents the comparison of the averaged reflectance for all three specimens. Before exposure to different environmental conditions, the reflectance on the front face was approximately 14.5 for all specimens, with a standard deviation of 0.89, regardless of curing method. In contrast, the reflectance on the side face showed greater variability, with an average value of 12.8 and a standard deviation of 1.21 measured immediately after demolding. The reflectance of the specimen cured under standard conditions changed significantly, whereas the specimens cured in the oven and outdoors showed only small changes in reflectance (approximately 1-3%).

Figure 8.14 presents the relationship between surface reflectance and compressive strength measured 60 days after exposure to different curing conditions. Specimens cured in the oven achieved the highest compressive strength (approximately 14,000 psi), while those subjected to outdoor and standard curing exhibited comparable strengths, both near 12,000 psi. This outcome indicates that elevated-temperature curing promotes a higher degree of hydration, resulting in increased strength. However, the surface roughness inferred from reflectance measurements did not reflect this trend, suggesting that reflectance may not be sensitive to strength-related microstructural differences under these curing conditions.

Chapter 9 Determination of Concrete Mixtures for Railroad Crossties

9.1 Water-to-Binder Ratio

The mixtures tested with a water-to-binder ratio lower than 0.25 satisfied the AREMA strength requirement without the need for additional steam curing (i.e., Groups 3 and 4). For mixtures prepared with such low water-to-binder ratios, a paste content of approximately 35% provided the best overall performance. Further reductions in paste content resulted in inadequate workability, even with the designated dosage of superplasticizer.

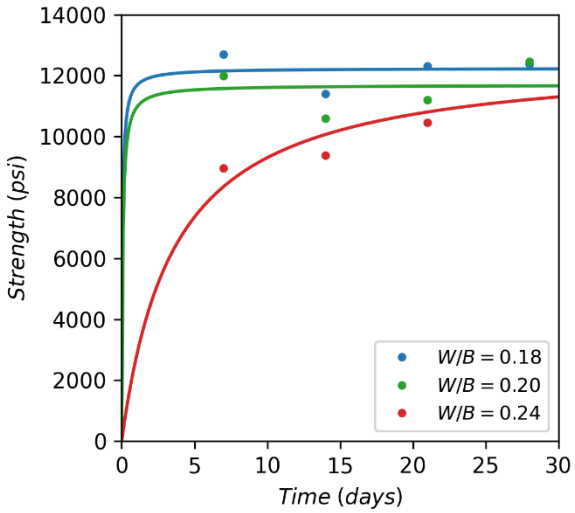

Figure 9.1 Comparison of Strength Development for the Mixtures with Lower W/B Ratios

Nonetheless, Figure 9.1 presents the strength development of the mixtures without fibers. All three mixtures incorporated 15% silica fume and 15% fly ash. The difference in strength between the mixtures with W/B=0.2 and W/B=0.18 was negligible, with variations of less than 1,000 psi at each test age. In contrast, the mixture with W/B=0.24 exhibited noticeably lower early-age strength, approximately 3,000 psi less than the other two mixtures. However, its strength development progressively caught up at later ages, ultimately aligning more closely with the strengths of the lower-W/B mixtures. Regardless, all three mixtures satisfied the AREMA strength requirement at 7 days, indicating that steam curing can effectively accelerate early-age strength development.

9.2 Binder and Paste Contents

Figure 8.7 illustrates the relationship between binder content (expressed as either mass per unit volume or paste volume fraction) and compressive strength. Both relationships are nonlinear, indicating that mixtures with approximately 1,000 to 1,200 lb of binder per cubic yard, corresponding to roughly 40% paste content for the given W/B ratio, tend to achieve higher compressive strength. However, mixtures containing 900 to 1,100 lb of binder per cubic yard

also satisfy the AREMA strength requirement. It is further observed that mixtures with a paste volume fraction of V_p=0.3 exhibit a wide range of compressive strengths (approximately 4,000 to 14,000 psi), depending on other mixture parameters. Therefore, when the target strength can be met, a mixture with V_p=0.35 is preferable to one with V_p=0.4, as it reduces the environmental impact associated with higher binder content.

9.3 Supplementary Cementitious Materials

Figure 8.5 and Figure 8.6 illustrate the effects of fly ash and GGBFS on compressive strength. All mixtures included 15% silica fume as a baseline, forming a ternary cementitious system with either fly ash or GGBFS. GGBFS, at any replacement ratio considered in this study (15 to 45%), consistently achieved strengths exceeding the AREMA requirement at all testing ages. In contrast, mixtures with fly ash replacement exceeding 45% did not meet the AREMA requirement at early ages; however, by 14 days or later, all fly ash replacement levels examined (15 to 55%) attained the required strength. Considering the ACI 318 [50] recommendation limiting fly ash content to 25%, the replacement ratio could be increased up to 40% to reduce environmental impact. Moreover, since steam curing is a common practice for concrete crossties, any early-age strength delay caused by the pozzolanic reaction can be mitigated.

9.4 Aggregates

It should be noted that a paste volume fraction of V_p=0.35 corresponds to approximately 57 to 60% of the concrete volume being occupied by aggregates, depending on the air content (3% for non-air-entrained concrete and 6% for air-entrained concrete) and fiber dosage. The proportion of fine aggregate relative to the total aggregate is a key factor influencing concrete strength; however, this proportion must be considered in the context of the combined grading of fine, intermediate, and coarse aggregates. As shown in Figure 7.1, the aggregate blend used in this study conforms to the 0.45 power curve, with the sand fraction adjusted as needed to achieve the target grading.

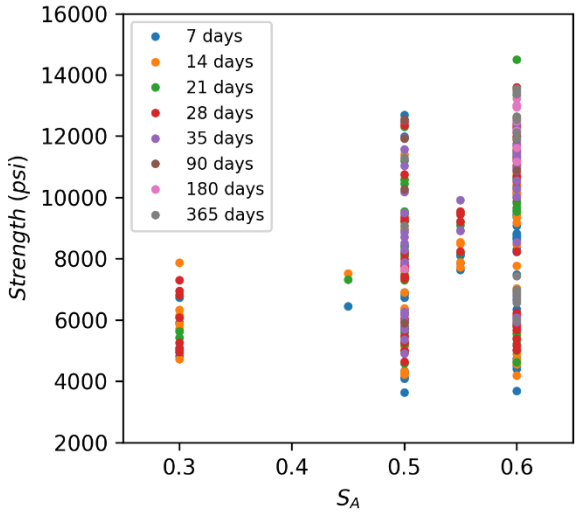

Figure 9.2 Relationship between Strength and S_A

Figure 9.2 presents the relationship between S_A (the volume fraction of fine aggregates relative to the total aggregate volume) and compressive strength for the mixtures examined in this study. As expected, no distinct trend is observed; however, both S_A=0.5 and S_A=0.6 are capable of achieving the full range of target strengths. This finding confirms that achieving the desired aggregate grading is more critical than the specific proportion of fine aggregates.

9.5 Fiber Inclusion

This study utilizes the non-metallic fiber, basalt fiber, to mitigate any potential corrosion issues. The dosage of fiber significantly influences both strength and the impact of load resistance. From this study, 1% of the concrete volume with the 22-mm basalt fiber achieved the best performance in compressive strength and impact load resistance. Note that the addition of the fiber reduces the workability of the concrete; however, it can be controlled by the superplasticizer.

Chapter 10 : Conclusions

This study investigated the mechanism of stress-induced failures of PSCCs focusing on prestressing tendon indentation geometry—specifically shape, volume, depth, and sidewall angle—on the structural characteristics of prestressed concrete prisms. The research methodology utilized a multi-scale approach, integrating SolidWorks for geometric modeling and a parallel computing algorithm for a large degree of freedom model analysis. While nine small-scale elastic models were analyzed on local processors, the high computational demands of the six intermediate and full-scale Prestressed Concrete (PSC) models necessitated the use of the High-Performance Computer (HPC).

Analysis of the small-scale pullout models yielded several key findings regarding the elastic stiffness of the steel-concrete bond:

1. Sidewall Angle: The sidewall angle emerged as the dominant factor influencing stiffness. Results indicate that angles approaching 90^{o} maximize mechanical interlocking. However, implementing such steep angles presents significant manufacturing challenges due to the limitations of current stamping processes.
2. Shape and Depth: The indentation shape and depth of cut demonstrated a notable influence on model response. Specifically, shallower indentation (as seen in the WG model) correlated with lower stiffness values. While some anomalies in the data suggest sensitivity to boundary loading conditions—such as the variance between original and reversed Chevron patterns—the overall trend confirms that geometric shape is a governing parameter for bond performance.

The successful migration of the intermediate and full-scale models to a parallel computing environment allowed for high-resolution analysis of degrees of freedom exceeding 18 million. This computational capacity enabled several critical observations:

1. A framework for analyze large degree of freedom of a full-scale prestressed concrete crossties model has been successfully developed and executed for de-tensioning analysis.
2. Displacement and Interlocking: The model with smooth WA tendons experienced the highest magnitude of displacement (contraction) upon prestress release, followed by the shallow-indented WG, with the deep-indented WP exhibiting the least displacement. This empirically validates the superior mechanical interlocking provided by deeper indentations.
3. Stress Concentrations vs. Interlocking: A critical trade-off was identified through the interface stress analysis. While deeper indentations and steeper sidewall angles guarantee better interlocking (reduced displacement), they simultaneously induce higher stress concentrations at the angular peaks of the concrete indentations. As anticipated, these localized stress surges significantly increase the susceptibility of the concrete to crack initiation.
4. Most of the critical damage zones are found to be with in 1.5 in from the free end upon prestress release.

This research highlights the delicate balance required in tendon design: maximizing interlocking stiffness while minimizing stress concentrations that lead to premature cracking. The numerical simulations, demonstrate that Chevron WG (shallow indentation) often provides an optimal compromise compared to the Smooth WA or the Deep Chevron WP. Furthermore, the study underscores the indispensable value of High-Performance Computing in simulating complex, full-scale structural behaviors that are computationally prohibitive on standard processors.

Furthermore, the study is to demonstrate that high-performance concrete mixtures for railroad crossties can be successfully developed to meet the strength and durability requirements specified by AREMA while considering cost and environmental impacts. Mixtures with a water-to-binder ratio below 0.25 achieved the required 28-day compressive strength without steam curing, and a paste volume fraction of approximately 35% provided an optimal balance between strength, workability, and sustainability. Incorporating supplementary cementitious materials, particularly silica fume and GGBFS, proved effective in enhancing strength and reducing environmental footprint, while fly ash can be used up to 40% replacement without compromising long-term performance when steam curing is applied. Aggregate grading following the 0.45 power curve ensured consistent strength development, and the inclusion of 1% basalt fiber improved impact resistance without significant adverse effects on compressive strength.

Overall, the findings support the feasibility of designing cost-effective, and durable concrete mixtures for railroad crossties. It is recommended that future work focuses on long-term durability assessments under field conditions and optimization of fiber reinforcement strategies to further enhance structural performance of railroad track structures.

Chapter 11 References

[1] National Transportation Safety Board, "Railroad Accident Brief: Accident No. DCA-050FR-101," Washington D.C., 2006.

[2] M. Mayville, Ronald A., Jiang, Liying, Sherman, "Performance Evaluation of Concrete Railroad Ties on the Northeast Corridor," 2014.

[3] Z. Chen, M. Shin, B. Andrawes, and J. R. Edwards, "Parametric study on damage and load demand of prestressed concrete crosstie and fastening systems," *Eng Fail Anal*, vol. 46, pp. 49–61, 2014, doi: 10.1016/j.engfailanal.2014.08.002.

[4] Z. Chen, M. Shin, S. Wei, B. Andrawes, and D. a. Kuchma, "Finite element modeling and validation of the fastening systems and concrete sleepers used in North America," *Proc Inst Mech Eng F J Rail Rapid Transit*, vol. 228, no. 6, pp. 590–602, 2014, doi: 10.1177/0954409714529558.

[5] F. Element, B. Modeling, F. O. R. Indented, W. In, and C. Crossties, "JRC2016-5782 FINITE ELEMENT BOND MODELING FOR INDENTED WIRES IN PRETENSIONED," pp. 1–10, 2016.

[6] J. R. Holste, "Experimental determination of prestressing wire bond and splitting propensity characteristics through tensioned pullout tests," Ph.D. Thesis, Kansas State University, 2014.

[7] Federal Railroad Administration, *Qualitative Lifecycle Analysis of Rail Tie Materials*. Massachusetts: U. S. Department of Transportation, 2024.

[8] J. W. Weber, "Concrete Crossties in the United States," *PCI Journal*, vol. 14, no. 1, pp. 46–61, Feb. 1969.

[9] M. A. H. Diaz, A. Scouse, and S. S. Kelly, "Environmental Full Cost Accounting of Alternative Materials Used for Railroad Ties: Treated-wood and Concrete Case Study," *J Clean Prod*, vol. 364, p. 132536, Sep. 2022.

[10] A. H. Lovett, C. T. Dick, Jr. Conrad Ruppert, and C. P. L. Barkan, "Cost and Delay of Railroad Timber and Concrete Crosstie Maintenance and Replacement," *Transp Res Rec*, vol. 2426, no. 1, pp. 37–44, Jan. 2015.

[11] E. Ferro, J. Harkness, and L. Le Pen, "The Influence of Sleeper Material Characteristics on Railway Track Behavior: Concrete vs. Composite Sleeper," *Transportation Geotechnics*, vol. 23, p. 100348, Jun. 2020.

[12] AREMA, *Manual for Railway Engineering*. Maryland: American Railway Engineering and Maintenance-of-Way Association, 2025.

[13] H. Yu, D. Jeong, J. Choros, and T. Sussmann, "Finite Element Modeling of Prestressed Concrete Crossties with Ballast and Subgrade Support," *ASME 2011 International Design Engineering Technical Conferences*, pp. 1–10, 2011, doi: 10.1115/DETC2011-47452.

[14] B. Hwan Oh, E. Sung Kim, and Y. Cheol Choi, "Theoretical Analysis of Transfer Lengths in Pretensioned Prestressed Concrete Members," *J Eng Mech*, vol. 132, no. 10, pp. 1057–1066, 2006, doi: 10.1061/(ASCE)0733-9399(2006)132:10(1057).

[15] L. J. Malvar, "Bond of Reinforcement Under Controlled Confirement," *ACI Mater J*, vol. 89, no. 6, p. 593~601, 1992.

[16] P. ; K. R. Gupta, "A STUDY ON DEVELOPMENT OF STRESSES IN ANCHORAGE ZONE USING PARALLEL PROCESSING | Semantic Scholar," *Asian Journal of Civil Engineering*, pp. 47–59, 2008.

[17] B. T. Stuart, C.D.; Peterman, R.J.; Beck, "A WIRE INDENT PROFILING SYSTEM FOR THE ASSESSMENT OF CROSSTIE BOND AND SPLITTING PROPENSITY," 2019.
[18] ACI Committee 239, *Ultra-High-Performance Concrete: An Emerging Technology Report*. Michigan: American Concrete Institute, 2018.
[19] S. H. Kosmatka, B. Kerkhoff, and W. C. Panarese, *Design and Control of Concrete Mixtures*, 17th ed. Skokie, Illinois: Portland Cement Association, 2021.
[20] M. Rößler and I. Odler, "Investigations on the Relationship between Porosity, Structure and Strength of Hydrated Portland Cement Pastes I. Effect of Porosity," *Cem Concr Res*, vol. 15, no. 2, pp. 320–330, Mar. 1985.
[21] C. Lian, Y. Zhuge, and S. Beecham, "The Relationship between Porosity and Strength for Porous Concrete," *Cement and Building Materials*, vol. 25, no. 11, pp. 4294–4298, Nov. 2011.
[22] V. S. Gopalaratnam, S. P. Shah, G. B. Batson, M. E. Criswell, V. Ramakrishnan, and M. Wecharatana, "Fracture Toughness of Fiber Reinforced Concrete," *ACI Mater J*, vol. 88, no. 4, pp. 339–353, Jul. 1991.
[23] N. Banthia, V. Bindiganavile, J. Jones, and J. Novak, "Fiber-reinforced concrete in precast concrete applications: Research leads to innovative products," *PCI Journal*, vol. 57, no. 3, pp. 33–46, Aug. 2012.
[24] D.-Y. Yoo and N. Banthia, "Impact resistance of fiber-reinforced concrete – A review," *Cem Concr Compos*, vol. 104, no. 103389, pp. 1–22, Nov. 2019.
[25] L. Farahzadi, L. G. F. Tellnes, B. Shafei, and M. Kioumarsi, "Life-Cycle Environmental Assessment of Ultra-High-Performance Concrete with Sustainable Materials and Fiber Substitutions," *Clean Eng Technol*, vol. 23, p. 100846, Dec. 2024.
[26] H. A. Shah, Q. Yuan, and N. Photwichai, "Use of Materials to Lower the Cost of Ultra-High-Performance Concrete - Review," *Constr Build Mater*, vol. 327, p. 127045, Apr. 2022.
[27] American Association of State Highway and T. Officials, *Standard Test Method of Moisture Content Penetration Resistance Relationships of Fine-Grained Soils*. Washington, D.C.: American Association of State Highway and Transportation Officials, 2020.
[28] ACI Committee 329, *Report on Performance-Based Requirements for Concrete*. Michigan: American Concrete Institute, 2014.
[29] O. S. B. Al-Amoudi, W. A. Al-Kutti, S. Ahmad, and M. Maslehuddin, "Correlation between Compressive Strength and Certain Durability Indices of Plain and Blended Cement Concretes," *Cem Concr Compos*, vol. 31, no. 9, pp. 672–676, Oct. 2009.
[30] W. Piasta and B. Zarzycki, "The Effect of Cement Paste Volume and W/C ratio on Shrinkage Strain, Water Absorption and Compressive Strength of High Performance Concrete," *Constr Build Mater*, vol. 140, pp. 395–402, Jun. 2017.
[31] S. Kaewunruen and A. M. Remennikov, "Progressive Failure of Prestressed Concrete Sleepers under Multiple High-Intensity Impact Loads," *Eng Struct*, vol. 31, no. 10, pp. 2473–2640, Oct. 2009.
[32] L. Mao, S. J. Barnett, A. Tyas, J. Warren, G. K. Schleyer, and S. S. Zaini, "Response of Small Scale Ultra High Performance Fibre Reinforced Concrete Slabs to Blast Loading," *Constr Build Mater*, vol. 93, pp. 822–830, Sep. 2015.
[33] R. Ranade, V. C. Li, W. F. Heard, and B. A. Williams, "Impact Resistance of High Strength-High Ductility Concrete," *Cem Concr Res*, vol. 98, pp. 24–35, Aug. 2017.

[34] A. A. Shurpali, J. R. Edwards, R. G. Kernes, D. A. Lange, and C. P. L. Barkan, "Investigation of Material Improvements to Mitigate the Effects of the Abrasion Mechanism of Concrete Crosstie Rail Seat Deterioration," *J Transp Eng*, vol. 140, no. 2, Aug. 2013.
[35] A. A. Shurpali, J. R. Edwards, R. G. Kernes, D. A. Lange, and C. P. L. Barkan, "Improving the Abrasion Resistance of Concrete to Mitigate Concrete Crosstie Rail Seat Deterioration (RSD)," *Mater Perform Charact*, vol. 6, no. 1, pp. 521–534, Dec. 2017.
[36] S. M. Cheyad, A. N. Hilo, and S. Al-Gasham, "Comparing the Abrasion Resistance of Conventional Concrete and Geopolymer Samples," *Mater Today Proc*, vol. 56, no. 4, pp. 1832–1839, Nov. 2022.
[37] F. Wu, X. Chen, and J. Chen, "Abrasion Resistance Enhancement of Concrete using Surface Treatment Methods," *Tribol Int*, vol. 179, p. 108180, Jan. 2023.
[38] P. M. D. Santos and E. N. B. S. Júlio, "Comparison of Methods for Texture Assessment of Concrete Surfaces," *ACI Mater J*, vol. 107, no. 5, pp. 433–440, Sep. 2010.
[39] N. Fisco and H. Sezen, "Comparison of Surface Macrotexture Measurement Methods," *Journal of Civil Engineering and Management*, vol. 19, no. 1, pp. 153–160, Nov. 2013.
[40] S. R. Abid, S. H. Ali, G. Murali, and T. S. Al-Gasham, "A Simple Suggested Approach to Reduce the Testing Time of Concrete Surface Abrasion using ASTM C1138," *Case Studies in Construction Materials*, vol. 15, p. e00685, Dec. 2021.
[41] ASTM, "A881/A881M Standard Specification for Steel Wire, Deformed, Stress-Relieved or Low-Relaxation for Prestressed Concrete Railroad Ties." Accessed: Nov. 21, 2025. [Online]. Available: https://store.astm.org/a0881_a0881m-02.html
[42] A. A. Robertson, "A wire indent profiling system for the assessment of crosstie bond and splitting propensity," Kansas State University, Manhattan , 2025.
[43] ACI Committee 318, "318-14 Building code requirements for structural concrete and commentary," *ACI Standard and Report*, vol. 11, p. 520, 2014, doi: 10.2748/tmj/1232376167.
[44] V. 6. 14-2 ABAQUS User Manual, *ABAQUS Documentation*. Providence, RI, USA: Dassault Systemes Simulia Corp, 2014.
[45] Paraview, "ParaView - Open-source, multi-platform data analysis and visualization application." Accessed: Nov. 26, 2025. [Online]. Available: https://www.paraview.org/
[46] "TACC." Accessed: Nov. 24, 2025. [Online]. Available: https://tacc.utexas.edu/about/citing-tacc/
[47] Massachusetts Department of Transportation, "Qualified Construction Materials List," 2025.
[48] ACI Committee 211, *Standard Practice for Selecting Proportions for Normal, Heavyweight, and Mass Concrete*. Michigan: American Concrete Institute, 1991.
[49] B. Bissonnette, P. Pierre, and M. Pigeon, "Influence of Key Parameters on Drying Shrinkage of Cementitious Materials," *Cem Concr Res*, vol. 29, no. 10, pp. 1655–1662, Oct. 1999.
[50] ACI Committee 318, *Building Code Requirements for Structural Concrete (ACI318-14)*. Michigan: American Concrete Institute, 2014.
[51] ACI Committee 350, *Code Requirements for Environmental engineering Concrete Structures*. Michigan: American Concrete Institute, 2020.
[52] ACI Committee 232, *Report on High-Volume Fly Ash Concrete for Structural Applications*. Michigan: American Concrete Institute, 2014.

[53] W. B. Fuller and S. E. Thompson, "The Laws of Proportioning Concrete," *Transactions of the American Society of Civil Engineers*, vol. 59, no. 2, pp. 67–143, Dec. 1907.
[54] ASTM C187-16, *Standard Test Method for Amount of Water Required for Normal Consistency of Hydraulic Cement Paste*. West Conshohocken, PA: ASTM International, 2016.
[55] G. A. Rao, "Investigations on the performance of silica fume-incorporated cement pastes and mortars," *Cem Concr Res*, vol. 33, no. 11, pp. 1765–1770, Nov. 2003.
[56] ASTM C192/C192M-16a, *Standard Practice for Making and Curing Concrete Test Specimens in the Laboratory*. West Conshohocken, PA: ASTM International, 2016.
[57] ASTM C39/C39M-17a, *Standard Test Method for Compressive Strength of Cylindrical Concrete Specimens*. West Conshohocken, PA: ASTM International, 2017.
[58] ACI Committee 209, *Guide for Modeling and Calculating Shrinkage and Creep in Hardened Concrete*. Michigan: American Concrete Institute, 2008.
[59] ACI Committee 209, *Prediction of Creep, Shrinkage, and Temperature Effects in Concrete Structures*. Michigan: American Concrete Institute, 1992.
[60] D. A. Abrams, "Design of Concrete Mixtures," Chicago, 1924.
[61] D. A. Abrams, "Effect of Curing Condition on the Wear and Strength of Concrete," Chicago, 1922.
[62] N. I. Vatin, M. Hematibahar, and T. H. Gebre, "Impact of Basalt Fiber Reinforced Concrete in Protected Buildings: a Review," *Front Built Environ*, vol. 10, May 2024.
[63] E. T. Al-Rousan, H. R. Khalid, and M. K. Rahman, "Fresh, Mechanical, and Durability Properties of Basalt Fiber-Reinforced Concrete (BFRC): A Review," *Developments in the Built Environment*, vol. 14, p. 100155, Apr. 2023.
[64] ACI Committee 214, *Evaluation of Strength Test Results of Concrete*. Michigan: American Concrete Institute, 2002.
[65] D. Ghosh, Z. J. Ma, and D. Hun, "Effect of GGBFS slag on CSA-based Ternary Binder Hydration, and Concrete Performance," *Constr Build Mater*, vol. 386, p. 131554, Jul. 2023.
[66] Y. Zhao, J. Gao, Z. Xu, S. Li, X. Luo, and G. Chen, "Long-term Hydration and Microstructure Evolution of Blended Cement Containing Ground Granulated Blast Furnace Slag and Waste Clay Brick," *Cem Concr Compos*, vol. 118, p. 103982, Apr. 2021.
[67] M. Li, L. Wang, J. Wang, X. Li, F. Xu, and S. Liu, "Hydration Properties of Cement Paste Containing High Volume Ground Granulated Blast Furnace Slag (GGBFS)," *J Therm Anal Calorim*, vol. 150, pp. 13099–13113, Jul. 2025.
[68] S. Mindess, J. F. Young, and D. Darwin, *Concrete*, 2nd ed. NJ 07458: Pearson Education, Inc., 2003.
[69] S. Kolias and C. Georgiou, "The Effect of Paste Volume and of Water Content on the Strength and Water Absorption of Concrete," *Cem Concr Compos*, vol. 27, no. 2, pp. 211–216, Feb. 2005.
[70] Z. Jiang, Y. Mao, D. Jiao, X. Hu, M. T. Ghafoor, and C. Shi, "Effect of SCM and Superplasticizer on Excessive Paste Thickness and Properties of Concrete," *Cem Concr Compos*, vol. 164, p. 106233, Nov. 2025.
[71] E. Roziére, S. Granger, Ph. Turcry, and A. Loukili, "Influence of Paste Volume on Shrinkage Cracking and Fracture Properties of Self-Compacting Concrete," *Cem Concr Compos*, vol. 29, no. 8, pp. 626–636, Sep. 2007.

[72] P. Klieger, “Effect of Mixing and Curing Temperature on Concrete Strength,” *ACI Journal Proceedings*, vol. 54, no. 12, pp. 1063–1081, Jun. 1958.
[73] C. H. Lee and K. C. Hover, “Compatible Datum Temperature and Activation Energy for Concrete Maturity,” *ACI Mater J*, vol. 113, no. 2, pp. 197–206, Mar. 2016.
[74] C. H. Lee and K. C. Hover, “Relationship between Computed Rate Constants and the Variability in Maturity-Based Strength Predictions,” *J Test Eval*, Nov. 2018.
[75] G. J. Verbeck and R. H. Helmuth, “Structures and physical properties of cement pastes,” in *Proceedings of the 5th International Symposium on the Chemistry of Cement*, Tokyo, Oct. 1968, pp. 1–32.
[76] C. H. Lee and K. C. Hover, “Influence of Datum Temperature and Activation Energy on Maturity Strength Prediction,” *ACI Mater J*, vol. 112, no. 6, pp. 781–790, Nov. 2015.

Transportation Infrastructure Durability Center
AT THE UNIVERSITY OF MAINE

35 Flagstaff Road
Orono, Maine 04469
tidc@maine.edu
207.581.4376

www.tidc-utc.org